Dynamic Modeling and System Identification of the Human Respiratory System

Jiayao Yuan

Submitted in partial fulfillment of the
requirements for the degree of
Doctor of Philosophy
under the Executive Committee
of the Graduate School of Arts and Sciences

COLUMBIA UNIVERSITY

2021

Abstract

Dynamic Modeling and System Identification of the Human Respiratory System

Jiayao Yuan

The lungs are the primary organ of the respiratory system. Their main function is to provide freshly breathed oxygen (O_2) to the blood capillaries, while taking carbon dioxide (CO_2) from them and expelling it to the atmosphere. Lung conditions such as Acute Respiratory Distress Syndrome (ARDS), Idiopathic Pulmonary Fibrosis (IPF), Coronavirus Disease (COVID-19), etc., cause impaired gas exchange that is life-threatening. In this dissertation, I developed 1) a physiology-based dynamic pulmonary system to study the lung normo- and patho-physiology, and 2) a model-based constrained optimization algorithm to do parameter estimation in order to non-invasively assess lung health. The goals of this work are 1) to accomplish a respiratory personalized medicine example for clinical decision support, and 2) to further the understanding of respiratory physiology, via a mechanistic physiology-based model and system identification techniques.

The mechanistic model presented in this thesis comprises six subsystems: 1) a lung mechanics module that computes airflow transport from the mouth and nose to the alveoli (gas exchange units), 2) a respiratory muscles and rib cage mechanics module that simulates the effect of the respiratory muscle contraction on the lungs and the rib cage, 3) a microvascular exchange system that describes fluid (water) and mass (albumin and globulin) transport between the pulmonary capillaries and the alveolar space, 4) an alveolar elasticity module that computes alveolar compliance as a function of the pulmonary surfactant concentration and the elastic properties of the lung tissue fiber, 5) a pulmonary blood circulation that describes blood transport from the heart

to the pulmonary system, and 6) a gas exchange system that describes O_2 and CO_2 transport between blood in the pulmonary capillaries and gas in the alveoli. Each subsystem was developed based on the latest knowledge of lung physiology and was validated using patient data when available or published and validated physiology-based models. To our knowledge, the combined six-module model would be the most rigorous and expansive lung dynamic model in the literature. This dynamic respiratory system can be used to describe human breathing under healthy and diseased conditions. The model can readily be used to test different what-if scenarios to find the optimal therapy for the patients.

Further, I tailor the proposed lung model and adopt system identification techniques for noninvasive assessment of the lung mechanical properties (resistance and compliance) and the patient breathing effort. Pulmonary syndromes or diseases, such as ARDS and COPD (Chronic Obstructive Pulmonary Disease) evoke alterations in lung resistance and compliance. These two parameters reflect, by and large, the state of health and functionality of the respiratory system. Hence tracking these two parameters can lead to better disease diagnosis and easier monitoring of the respiratory disease progression. For spontaneously breathing patients on ventilatory support, the estimation of the lung parameters is challenging due to the added patient's breathing effort. This dissertation presents a model-based nonlinear constrained optimization algorithm to estimate, breath-by-breath, the lung resistance, the lung compliance, as well as the patient breathing effort due to the respiratory muscle activity, using readily available non-invasive measurements (airway opening pressure and airflow).

Table of Contents

List of Figures

List of Tables

Acknowledgments

As I approach the end of my remarkable PhD adventure at Columbia University and the beginning of my professional career, I want to take a moment to give my sincere gratitude to those people who have made this milestone possible. They have sharpened my mind, developed my professional skills and made this journey unique, memorable, and invaluable, I wish to give my whole-hearted appreciation to the following individuals.

First, my deepest gratitude goes to Professor Nicolas W. Chbat, my PhD advisor. It was Nick's inspiring lectures that introduced and led me to the world of healthcare. I was truly touched by his passion for improving the current state of medicine and vision of applying quantitative approaches to the human body, his passion and vision have guided me through my entire PhD journey. As the founder of Quadrus Medical Technologies (QMT), Nick has put theory into practice and showed me how theories in textbooks should be put into practice. Additionally, I would like to pay my special regards to Caitlyn M. Chiofolo, Vice President of QMT. She is smart and knowledgeable about the clinical field. During our weekly meetings, she has offered her constructive advice and warm encouragement. It was Nick and Caitlyn, who not only taught me the fundamentals of research, but also kept the process fun and exciting. They provided me invaluable technical guidance, pushed me to exceed my limits, and helped me reach higher academic maturity. They are continuous sources of inspiration and support. This thesis would not have been possible without their selfness contribution.

Secondly, I want to express my appreciation for my academic advisor Professor Andrew Laine at Columbia University for his logistical and technical support during our monthly research updates. His contribution has advanced my thesis and bettered my PhD journey.

Next, I am most thankful for being part of Professor Chbat's PhD group, and it was Benjamin J Czerwin, Nikolaos Karamolegkos, and Antonio Albanese, who made this journey one-of-a-kind. Not only did they offer me support in research, they have also guided my career development and witnessed my life milestones. The fact that Ben and I started our PhD at a similar time and graduating together means there are countless memories share between us, those sleepless nights that we work relentlessly to meet paper deadlines, to prepare technical presentation, to discuss research details, and more. I am so grateful to work with Ben throughout this incredible journey. Thank you Nikos for the contribution to the simulation and validation work on Chapter I. As the co-author of Chapter I, professionally, you have shown me your knowledge of modeling and system identification, personally, you have shown me how to be a reliable resource and trustable teammate. I have found Antonio's PhD thesis inspiring and have used his work as the foundation for my research. I am extremely grateful for having Antonio's work as a building block to my thesis as well as having him as a mentor, who provided me valuable career guidance as my graduation approaches.

And then I would like to thank Quadrus Medical Technologies for providing financial support to my research along with accesses to their facilities. The engineering team at QMT, particularly Siddharth Chamarthy, Pruthav Khire, and Andrew Moshova, whom I worked closely with, I would like to express my gratitude toward them for their support of building the lung emulator in Chapter III.

Lastly, my warmest regards go to my lovely wife, Meng Wan, who is always there when I was in need. Thank you for the company and the encouragement to let me pursue my academic passion. I would also like to thank my parents-in-law, who have been providing care to our family, especially during this pandemic and special time as I approach this big milestone. Finally, I would

like to thank my parents, Wei Yuan, and Mei Tie, for their unconditional love and numerous guidance throughout my life. Thank you for giving me strength to pursue my dream and always believed in me.

Jiayao Yuan

January 2021

Dedication

To my family: without your love and care I could not have reached this point. I dedicate this dissertation to you.

Introduction

Many therapeutic decisions follow generalized protocols, or guidelines, that are based on epidemiological studies, and hence may not be suited for the individual patient. From basic measured patient signals and patient status, clinicians make clinical judgments derived from their experience and/or guidelines. Clinicians and researchers have recently put a lot of effort into improving guidelines, machine learning algorithms, and data mining techniques to detect diseases. A dynamic model of the human body for predicting diseases is still uncommon in current medicine, however, its benefits are numerous, including parameters that have real physical meaning and changes in which can be related to diseases and/or interventions. Building a mechanistic dynamic model that is physiology-based could be beneficial to the current state of medicine.

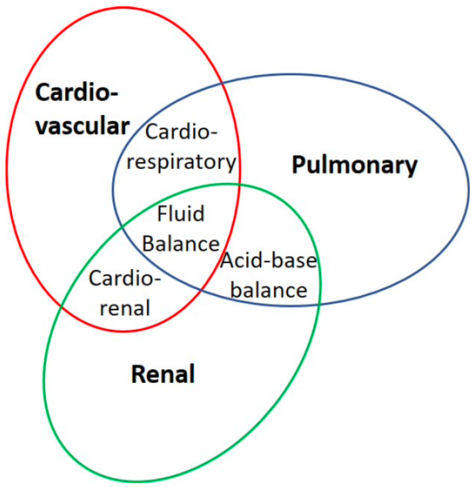

Figure 0. 1: Cardio-Pulmonary-Renal (CPR) model representation. Red: cardio-vascular system; Blue: pulmonary system; Green: renal system.

Dr. Chbat's research group aims to gain a deep understanding of fluid balance, since it has a major effect on human health. Our group has yielded two doctoral theses, one in cardiovascular modeling [1] and the other in cardio-respiratory modeling [2]. Two more are under development, one in pulmonary modeling (my work) and the other in renal modeling [3]. Dr. Albanese in our

group, developed a cardio-pulmonary (CP) dynamic model [1]. Following Albanese's work, Dr. Karamolegkos improved the cardiac section of the CP model by focusing on the heart-lung interaction phenomena [2], while the pulmonary system remains simplistic. My work fills an important gap, the pulmonary system model shown in Figure 0.1. Such a cardio-pulmonary-renal (CPR) model would certainly help in understanding interactions and ultimately fluid, solute and gas balance. This also facilitates the understanding of CPR diseases. System identification techniques can then be employed to estimate model parameters of the specific patient, in real-time. Such approaches can be utilized to facilitate personalized medicine. The first step towards achieving the goal is by developing a dynamic model of the targeted organ (for acute diseases).

In the respiratory system modeling field, many researchers have contributed to the understanding of the breathing mechanisms. Weibel published the morphometry of the human lung in 1963, which serves as the foundation of lung mechanics [4]. Guyton *et al.* published the classic medical physiology in 1956 [5], and updated regularly with the advancement of this field. In 1972, Guyton also published a rigorous physiology-based cardiopulmonary model in 1972 [6]. West then described respiratory physiology essentials systematically in 1974 [7]. In what follows is a current understanding of respiratory physiology. During quiet breathing, the nerve that originates in the neck (C3–C5) sends electric signals to activate the diaphragmatic and intercostal muscles. The contraction of respiratory muscles expands the thoracic cavity, generating a negative hydraulic pressure in the pleural cavity. This negative pressure generates a pulling force expanding the lungs and reducing the alveolar pressure. Due to the pressure gradient between atmospheric and alveolar pressures, airflow is then induced into the alveolar space through the mouth/nose, larynx, trachea and bronchi. The trachea and bronchi are airway tubes that divide repeatedly into more and more tubes of smaller and smaller diameter. The amount of air that reaches the alveolar space depends

on the energy stored and dissipated along the way. The alveoli are the main space for gas exchange. Due to the oxygen/carbon dioxide partial pressure gradient between the blood in the capillaries and gas in the alveoli, oxygen dissolves in the blood and gets carried to the entire body, and carbon dioxide leaves the blood and gets exhaled during expiration. The parameters (resistances and compliances, *i.e.* material property and geometry of the lungs) of lung tissue change when diseases are introduced. For Chronic Obstructive Pulmonary Disease (COPD) patients, for instance, the lung pathways are clogged and thus, resistances increase. With the contraction of respiratory muscles, very little air reaches the alveolar space, causing respiratory distress. Another pulmonary disease is pulmonary pneumonia, where the lung tissue becomes porous. Water from the pulmonary capillaries seeps into the alveoli, clogging the airway, and often causing acute respiratory distress syndrome. Under such conditions, alveolar surface tension also increases and collapses the alveolar space, which in turn, prevents gas exchange and causes acute respiratory distress. This is shown as a decrease in the lung compliance value.

Six subsystems were defined to rigorously capture lung behavior. They are: 1) lung mechanics module (Chapter I) that computes airflow transport from the mouth and nose to the alveoli (gas exchange units), 2) respiratory muscles and rib cage mechanics module (Chapter II) that simulates the effect of the respiratory muscle contraction on the lungs and the rib cage, 3) microvascular exchange system [8] (Chapter IV) that describes fluid (water) and mass (albumin and globulin) transport between the pulmonary capillaries and alveolar space, a link from the pulmonary circulation to the lungs, 4) alveolar elasticity module (Chapter I) that computes alveolar compliance as a function of the pulmonary surfactant concentration and the elastic properties of the lung tissue fiber, 5) pulmonary circulation (Chapter V) that describes blood flow transport from the heart to the pulmonary system, and 6) gas exchange system (Chapter V) that describes O_2 and

CO_2 exchange between blood in the pulmonary capillaries and gas in the alveoli, another link from the pulmonary circulation to the lungs. These six subsystems form one complete dynamic lung model that will serve as a tool for disease detection and prediction.

To achieve personalized medicine, we adopt optimization algorithms to estimate parameters of the physiological model that represent diseases. However, a more rigorous model indicates a bigger number of parameters, which could yield poor estimation results that do not make physiological sense. Therefore, we sometimes tailor the rigorous physiological model, *i.e.*, simplify or select a part of the model, based on different diseases in order to estimate the minimal number of parameters that best represent a disease. In this thesis, we tailor the proposed lung model to a simplistic lung mechanics model to estimate parameters of patients who have impaired lung mechanical properties, *i.e.*, obstructive and restrictive diseases like COPD and Acute Respiratory Distress Syndrome (ARDS). For ventilated patients with spontaneous breathing, we estimate the lung resistance, lung compliance, and respiratory muscle effort for better disease diagnosis, easier monitoring of the respiratory disease progression, and optimal ventilation settings.

In this dissertation, all the biological systems/mechanisms are represented using linear graphs. Linear graphs are a graphical representation of the physical system that can help in the construction of the equations of motion. The equations are derived by way of energy dissipation, storage, as well as transduction within or between different energy domains. The linear graph concept with a generic simple hydraulic example is introduced first. The six chapters are then introduced:

Chapter I: Alveolar Tissue Fibers and Surfactant Effects on Lung Mechanics – Model Development and Validation on ARDS and IPF Patients.

Chapter II: Respiratory Muscles and Rib Cage Mechanics – Mathematical Model Development and Validation with Patient Data.

Chapter III: Pulmonary Function Monitoring: Physiology-based Optimization Algorithm.

Chapter IV: Modeling of Transport Mechanisms in the Respiratory System: Validation via Congestive Heart Failure Patients.

Chapter V: Integrative Pulmonary Model with Lung Gas Exchange System and Pulmonary Blood Circulation.

Chapter VI: Summary and Future Work.

Modeling Approach – Linear Graph

We employ linear graph technique to aid in the development of our dynamic model. A linear graph is a visual tool that can concisely display all dynamics of a complex system to allow for a systematic formulation of all the system's dynamic equations [9]. We develop a linear graph of the respiratory system comprising all energy domains with transducers linking them together to present a complex dynamic system. As an example, Figure 0.2a shows a hydraulic system, where hydraulic flow from a source enters compartment 1. Every node (filled circle) represents a physical compartment and is labeled with a variable, pressure. Every line with an arrow represents a flow and is labeled with a parameter like a resistance, capacitance, inertance. Subscripts show the variables and parameters of the corresponding compartment. Any variables subscripted with ref are considered as known reference values. Arrows are illustrated in the positive defined direction, however, flow may occur in either direction. By using conservation of mass (analog to Kirchhoff's Current Law), as shown in Figure 0.2b, the flows entering must equal the sum of all flows leaving, being stored, or being transduced:

$$Q_{in} = Q_{st} + Q_{tr} + Q_d \tag{1}$$

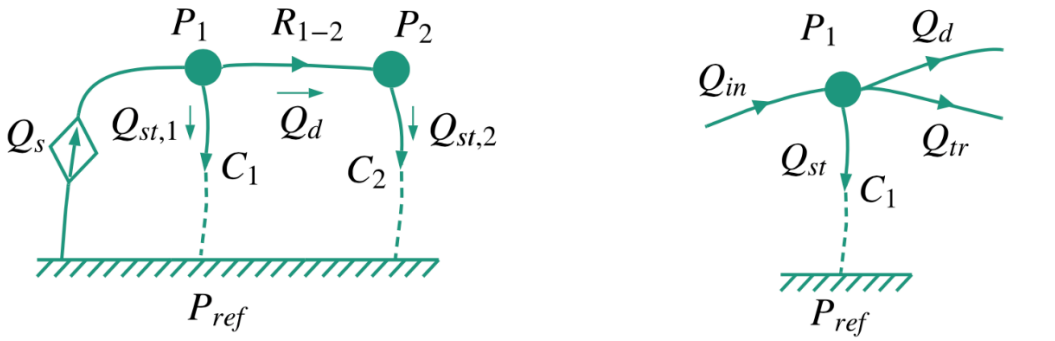

(a) Hydraulic Domain Linear Graph

(b) Generic Hydraulic Linear Graph

Figure 0. 2: P_1, P_2: hydraulic pressures in compartments 1 and 2; P_{ref}: reference pressure; C_1, C_2: hydraulic capacitances of compartments 1 and 2; R_{1-2}: hydraulic resistance between compartments 1 and

2; Q_s: flow input source; Q_{in}: flow going into compartment 1; Q_{st}: flow stored in compartment 1; Q_d: dissipative flow leaving compartment compartment 1; Q_{tr}: flow transduced into another energy domain

Chapter I: Alveolar Tissue Fibers and Surfactant Effects on Lung Mechanics – Model Development and Validation on ARDS and IPF Patients

Alveolar compliance is a main determinant of lung airflow. The compliance of the alveoli is a function of their tissue fiber elasticity, fiber volume, and surface tension. The compliance varies during respiration because of the nonlinear nature of fiber elasticity and the time-varying surface tension coating the alveoli. Respiratory conditions, like acute respiratory distress syndrome (ARDS) and idiopathic pulmonary fibrosis (IPF) affect fiber elasticity, fiber volume and surface tension. To better understand the lungs, we developed a physiology-based mathematical model to 1) describe the effect of tissue fiber elasticity, fiber volume and surface tension on alveolar compliance, and 2) the effect of time-varying alveolar compliance on lung mechanics for healthy, ARDS and IPF conditions. The proposed model is validated with healthy and diseased human data.

1.1 Introduction

The main function of the lungs is to provide freshly breathed oxygen (O_2) to the blood capillaries, while taking carbon dioxide (CO_2) in exchange from them and expelling it to the atmosphere. It does so tidally via repetitive inspiratory and expiratory cycles. This exchange is possible thanks to a hydraulic and a diffusive transport mechanism. Hydraulically, the respiratory system is defined as one tracheobronchial tree, that has 24 generations of dichotomous branching, extending from the trachea (close to the mouth) down to the alveolar sacs [4]. Generation 0 (trachea) to generation 16 (terminal bronchioles) are conducting pipes, known as dead space, where no gas exchange takes place. The branches from the respiratory bronchioles to the alveolar

sacs (generation 17 to 23) are defined as transitional and respiratory zones where CO_2 in the blood is exchanged for O_2 in the air diffusively.

Lung parenchyma, comprising a large number of thin-walled alveoli, has a complex internal structure with an inner surface area that maximizes gas exchange. The alveolus the basic gas exchange unit, is lined with a layer of epithelial cells (type I and type II). Type II epithelial cells secrete surfactants that are a mixture of lipids and proteins that line the inside of the alveoli, forming a film that reduces surface tension, to keep alveoli open, hence preventing alveolar collapse (atelectasis) and facilitating respiration. Alveolar surface tension is generated from molecular attractive forces of water on alveoli tissue. The surfactant plays a critical role in maintaining lung elasticity by lowering those attractive forces, effectively reducing surface tension [10][11]. Low surfactant concentration keeps alveoli closed at low lung pressure range (lung threshold opening pressure increases) due to the alveoli's inability to withstand increased surface tension. In between epithelial cells and the capillary basement membrane is the extracellular matrix (ECM) of the alveolar septal wall. The ECM contains elastin and collagen that determine the elasticity of the pulmonary tissue. Elastin is an essential load-bearing component of the ECM, and can withstand a large range of strain. Collagen, a helical shaped protein, provides considerable recoil stress during stretching. When lung volume increases to a certain level, the stress of the lung tissue increases significantly due to the nonlinear stress-strain relation of the collagen. Considering all these effects, the alveoli are held open under the balance of three pressures: 1) the transmural pressure, which is the difference between pleural cavity pressure and alveolar pressure, 2) the stresses in the elastin and collagen fibers, and 3) the alveolar surface tension, as determined by the surfactant concentration. The balance of these three pressures plays a crucial role in patients with respiratory distress. Patients with acute respiratory distress syndrome (ARDS), idiopathic pulmonary fibrosis

(IPF) have severely impaired gas exchange [4]–[9], due to increased lung stiffness that could cause alveolar collapse. Poor gas exchange causes hypoxemia, low levels of oxygen in the blood, that would lead to tissue and organ failure. Studies have shown that patients with ARDS, caused by pneumonia, sepsis, chest injury, etc., have low surfactant concentration and an increased amount of collagen compared to a healthy population [12]–[14]. On the other hand, patients with IPF were identified as not only having an increased amount of collagen but also a degraded quality of collagen [15]–[17]. ARDS and IPF patients have deficient pulmonary compliance and experience shortness of breath. Severe cases are life-threatening and need exogenous breathing support, like a mechanical ventilator. Pressure vs volume (PV) curves have been used at times at the patient's bedside [18] to show the stiffness of the diseased lungs, and it is crucial to recruit the collapsed alveoli in order to improve gas exchange.

Understanding the pulmonary system is studying lung mechanics, alveolar elasticity, gas exchange, as well as respiratory muscles and ribcage mechanics. Our focus here, however, is on lung mechanics and alveolar elasticity. The proposed lung model calculates alveolar compliance in time as a function of surfactant concentration, lung fiber (elastin and collagen) quantity, and fiber quality. Lung mechanics variables (*e.g.,* alveolar pressure) can then be computed using this time-varying alveolar compliance, and lung resistances. We validate the model via ARDS and IPF patients' data and PV curves. Furthermore, a study by, Gattinoni [19] claims that 20-30% of the coronavirus disease (COVID-19) patients admitted to the intensive care unit have severe hypoxemia associated with low lung compliance values. The proposed model thus has the potential to simulate COVID-19 patients who are lung compliance compromised.

In what follows, we first provide a brief literature review of the mathematical models of the respiratory system. We then describe the development of the proposed lung model (modeling

approach, equations, and parameters). We present simulation results and compare them to healthy human data [20], a published lung mechanics model [1], ARDS patient data and IPF patient data [24]. Finally, we summarize the model performance, and highlight future extensions of this work.

1.2 Method

1.2.1 Literature Review

Lung mechanics models with varying levels of rigor have been developed by researchers. A linear one-compartment (balloon type) dynamic model of the respiratory system with one resistive element (R) and one capacitor (C) is well accepted by the clinical community due to its simplicity [25]. A few mechanical ventilator applications adopt such a model to assess the patient's pulmonary health status by estimating R and C [26][27]. In 1991, a more rigorous linear model was proposed by Rideout [28] that included four compartments: larynx, trachea, bronchi, and alveoli. In his work, lung air tubes that share similar geometric and functional properties were lumped into one compartment. Rideout's model adequately describes lung mechanics, but fails to include (the nonlinear) alveolar elasticity and dynamic compliance, both of which are included in our work. Further, a complex model with several (10-50) parallel lung sections can also be found in the literature [29]. This work describes each section with an analog electrical network of a resistance in series with a capacitor.

To describe the nonlinear behavior of alveolar compliance, Venegas *et al.* proposed a sigmoidal equation to represent lung pressure – volume relationship [30]. This equation fits well to inflation and deflation limbs of the PV curves of normal and diseased lungs. Denny and Schroter developed a series of finite element models for the mammalian lung alveolar duct [31]–[34]. In their models, alveolus geometry was considered as a truncated octahedron and the amount and

distribution of elastin and collagen fiber bundles were studied. Surface tension effects as a function of surfactant concentration were fitted from available published patient data [35], [36]. Finally, Fujioka *et al.* developed a lung parenchyma model [37], which comprises individual alveoli. In that work, alveolar deformation was computed based on the elastin and collagen stresses, surface tension, and transmural pressure. Fujioka *et al.* focused on the effect of surfactant on the tethering force that is applied on the alveoli. To validate the model, Fujioka *et al.* simulated ARDS and compared their simulation results to the sigmoidal functions proposed by Venegas *et al.* [30]. We build upon Fujioka's and Venegas's by modeling the lung mechanics from the elasticity of individual alveolar units and their contribution to the time-varying alveoli capacitance, while including additional lung mechanics compartments per Rideout.

1.2.2 Model Development – Equations and Parameters

A model of the human pulmonary system can be described via four modules, as per Figure 1.1:

1) A lung mechanics (LM) module that computes airflow (Q_{air}), volumes, and pressures at different lung compartments, such as the alveolar space, as a result of a given pleural cavity pressure (P_{pl}) and an alveolar capacitance (C_{alv}), where P_{pl} and C_{alv} change in time.

2) An alveolar elasticity (AE) module that quantifies alveolar capacitance as a function of the nonlinear tissue fiber elasticity and the surfactant concentration, both of which change depending on the health of the pulmonary system.

3) A gas exchange module that computes the oxygen and carbon dioxide transport between blood in the pulmonary capillaries and gas in the lungs based on the airflow computed in the LM module.

4) A respiratory muscles and ribcage mechanics module that describes how respiratory muscle contraction affects ribcage motion and pleural cavity pressure.

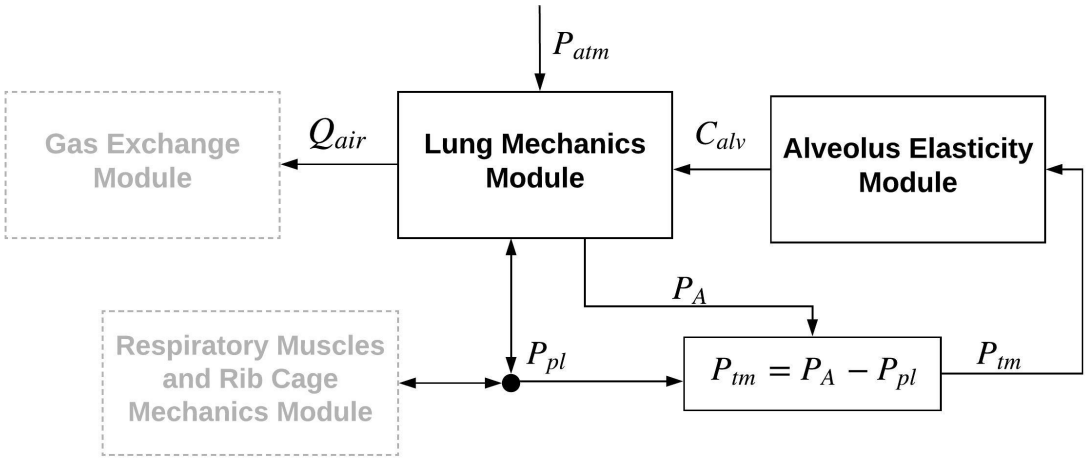

Figure 1. 1: Block diagram of lung modules. The two modules highlighted in black are described in this chapter. The full respiratory model comprises: lung mechanics, alveolus elasticity, respiratory muscles and rib cage mechanics, and gas exchange modules. P_{atm}: atmospheric pressure; P_A: alveolar space pressure; P_{pl}: pleural cavity pressure; P_{tm}: transmural pressure; C_{alv}: alveolar capacitance; Q_{air}: airflow into and out of the lungs.

In this chapter, we are presenting the first and the second modules only (dark boxes in Fig. 1). Following Rideout's work [28], we define four spatial compartments in series, which are larynx, trachea, bronchi and alveoli. A nonlinear module that computes time-varying alveolar capacitance was developed to replace the constant capacitance (or compliance as explained below), used by Rideout. We computed time-varying alveolar capacitance as a function of tissue fiber elasticity and surfactant concentration. Typically, parameters (representing material property and geometry) are constant values and variables, the solutions of the ordinary differential equations, change in time. However, in this work, we computed the time-varying property of the alveolar capacitance. Hence, it is a time-varying parameter. Figure 1.2A shows the linear graph of the lung mechanics module. We employ this graphing technique to allow for a systematic formulation of the system's

dynamic equations [38]. These equations consist of variables and parameters. Parameters represent material property and geometry of the lung compartments, such as hydraulic resistances and capacitors. Pressures and volumes are termed variables, which could potentially be measured through an instrument. In Figure 1.2A, every node (solid circle) represents pressure within a compartment of the respiratory system. Every line with an arrow represents a flow between two compartments and is labeled with the associated parameter of that segment. Alveolar capacitance (C_{alv}), is indicated with an additional oblique arrow because it is a time-varying parameter that is derived from the AE module. Airway opening (P_{ao}) and larynx (P_l) pressures are referenced to atmospheric pressure. Tracheal (P_{tr}), bronchial (P_b), and alveolar (P_{alv}) pressures are referenced to pleural cavity pressure (P_{pl}) since the pleural cavity anatomically encloses these three compartments. In this model, collagen volume (V_{col}) and surfactant concentration (Γ) appear as parameters in the AE module equations, since they are variables' fixed initial conditions that determine the severity of a lung disease in one simulation study, and as such they could be considered like parameters.

The pleural cavity pressure decreases as respiratory muscles contract, as is the case of inspiration, and increases as the pulmonary muscles relax, as in expiration. The reduction in P_{pl} generates a positive transmural pressure forcing the alveoli to expand. Alveolar expansion causes an alveolar pressure to drop and creates a pressure gradient between the mouth and the alveoli. Air subsequently gets inhaled into the lungs, and hence we breathe. P_{pl} is modeled according to Equation (1.1) [1]:

$$P_{pl} = \begin{cases} -\frac{P_{mag}}{T_I T_E} t^2 + \frac{T \cdot P_{mag}}{T_I T_E} t + P_{init} & 0 \le t < T_I \\ \frac{P_{mag}}{\left(1 - e^{-\frac{T_E}{\tau}}\right)} \left(e^{-\frac{t - T_I}{\tau}} - e^{-\frac{T_E}{\tau}}\right) + P_{init} & T_I \le t < T \end{cases} \tag{1.1}$$

where T_I is the inspiration time, T_E is the expiration time, T is the total time for one breath, and τ is the time constant of the exponential expiratory profile. P_{mag} is the magnitude of P_{pl} and P_{init} is the initial P_{pl} value at the beginning of inspiration. During quiet breathing, typically, P_{init} is -5 cmH_2O, P_{mag} is 3.5 cmH_2O, τ is 0.44 s, when the respiratory rate is 12 breaths/min (bpm), and the I:E ratio (ratio of the inspiratory time to the expiratory time) to 0.6 [1].

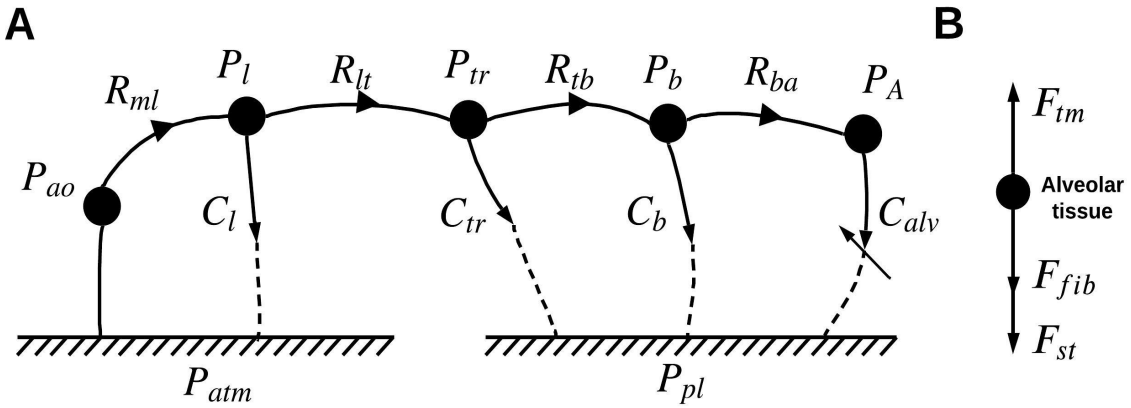

Figure 1. 2: (A) Linear graph of the lung mechanics module, and (B) force balance diagram of alveolar tissue. ao: airway opening; l: larynx; tr: trachea; b: bronchi; A: alveoli; pl: pleural cavity; atm: atmosphere; ml: mouth to larynx; lt: larynx to trachea; tb: trachea to bronchi; ba: bronchi to alveoli; tm: transmural; st: surface tension; fib: fibers; P: hydraulic pressure; F: force; C: hydraulic capacitance.

From the linear graph in Figure 1.2A, we can write the dynamic equations to solve for the variables in time at each node by applying continuity and compatibility laws. Continuity equations are derived from the laws of conservation of mass. As an example, Equation 1.2 represents the larynx pressure node:

$$C_l \dot{P}_l = \frac{P_{ao} - P_l}{R_{ml}} - \frac{P_l - P_{tr}}{R_{lt}} \tag{1.2}$$

All the variables in the system of equations change in time but the expression of variables as a function of t has been omitted for clarity. As such P_l should really be $P_l(t)$, etc. Table 1.1 summarizes capacitances (C), resistances (R), and unstressed volume (V_u) values in the LM module

[1] [28], with subscripts, l: larynx; t: trachea; b: bronchi; alv: alveoli; ml: mouth to larynx; lt: larynx to trachea; tb: trachea to bronchi; ba: bronchi to alveoli.

The mechanical properties of the alveolar tissue, which determine alveolar capacitance, are a function of fiber (elastin and collagen) stresses and surface tension [39]. At every simulation time step, the alveolus dimension is computed from the quasi-steady state of the force balance equation, $F_{tm} - F_{st} - F_{fib} = 0$, where F_{st} is the force due to surface tension, F_{fib} is the force due to lung fiber elasticity, and F_{tm} is the force due to transmural pressure ($P_A - P_{pl}$), as shown in Figure 1.2B. Note that this model simulates patients in supine position, where gravity gradient is negligible. The alveolus volume can then be determined by the transmural pressure (P_{tm}) that changes in time. The following describes the empirical relations of the fiber forces that relate fiber force/stress to alveolus dimension, and the assumptions of fiber distribution on a single alveolus.

Table 1. 1: Parameters for lung mechanics and alveolus elasticity.

Lung mechanics parameters		
Capacitance (L/cmH_2O)	Resistance ($cmH_2O \cdot s \cdot L^{-1}$)	Unstressed Volume (L)
$C_l = 0.00127$ [20]	$R_{ml} = 1.021$ [20]	$V_{u,l} = 34.4$ [20]
$C_t = 0.00238$ [20]	$R_{lt} = 0.3369$ [20]	$V_{u,t} = 6.63$ [20]
$C_b = 0.0131$ [20]	$R_{tb} = 0.3063$ [20]	$V_{u,b} = 18.7$ [20]
C_{alv} (Equation (1.6))	$R_{ba} = 0.0817$ [20]	$V_{u,alv} = 1.26$ [12]

Alveolus elasticity parameters			
	Septal border (cm^3)	Cross-linking (hex) (cm^3)	Cross-linking (square) (cm^3)
Elastin	4.4610×10^{-11}	8.6574×10^{-11}	9.9960×10^{-11}
Collagen	6.9616×10^{-11}	1.2986×10^{-10}	1.4994×10^{-10}

The elastin fiber is assumed to have a linear stress-strain relation with a Young's modulus of

7.1×10^6 dynes/cm^2 [32]. The collagen fiber has a highly nonlinear stress-strain relation, as shown in Equation (1.3):

$$\sigma_C = c_1 \log\left[1 - \frac{\exp(\epsilon_f)-1}{c_2}\right] + c_3\epsilon_f \quad (1.3)$$

where $c_1 = -2.25 \times 10^6$ dynes/cm^2, $c_2 = 1.264$, $c_3 = -1.78 \times 10^6$ dynes/cm^2, and ϵ_f is the fiber strain [32]. In Equation (1.3), the coefficients of collagen elasticity (c_1, c_2 and c_3) can quantify collagen degradation, where c_1 and c_3 are coefficients in the first nonlinear and second linear term, respectively, while c_2 limits strain nonlinearly as a disturbance to the exponential and the log function. In order to compute the fiber force due to fiber elasticity, the volume distribution of elastin and collagen on an alveolus was determined from the following four assumptions: 1) a truncated octahedron is adopted as the shape of one alveolus in the AE module, since Fung *et al.* found that the most common shapes of the surfaces of alveoli were hexagons and rectangles [40]. As shown in Figure 1.3, we defined septal border fibers and cross-linking fibers on square and hexagonal surfaces following the works by Fujioka *et al.* and by Denny *et al.* [32][37]. 2) Assuming the amount of the cross-linking fibers per unit area on a hexagonal face is identical to that on a square face, the volume of the cross-linking fibers on a square face is computed as $\sqrt{2}$ times the volume of same fibers on a hexagonal surface. 3) The alveolus expands and contracts analogously as the inner pressure changes, then the ratio of cross-sectional area between a septal border and a cross-linking fiber bundle is computed as 1.077 [37]. 4) The ratio of the amount of collagen to elastin is 1:5 [37][41]. The elastin and collagen volume of cross-linking fibers and septal borders are shown in Table 1.1. The fiber forces can thus be computed from the fiber stresses and the cross-sectional area of the fibers.

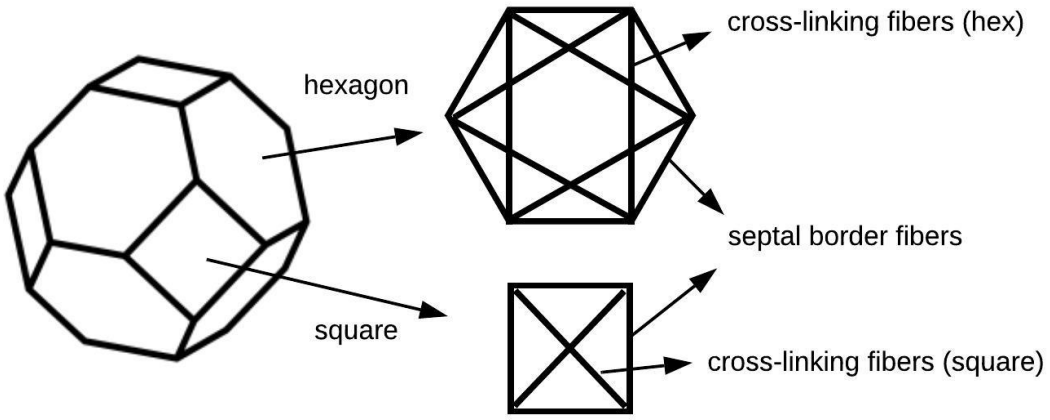

Figure 1. 3: Geometry and fiber structure of a single alveolus.

Surface tension is a function of surfactant concentration as shown in Equation (1.4):

$$\gamma = \begin{cases} \gamma_0 - E\Gamma & \Gamma < \Gamma_\infty \\ \Gamma_\infty \exp\left[\frac{E}{\Gamma_\infty}(\Gamma_\infty - \Gamma)\right] & \Gamma \geq \Gamma_\infty \end{cases} \tag{1.4}$$

where Γ is the surfactant concentration, Γ_∞ is a critical surfactant concentration = 3.1×10^{-7} g/cm^2 [42], γ_o is basal surface tension = 72 dynes/cm and $E\Gamma_\infty/\gamma_o = 0.7$. Γ is calculated as the ratio of the mass of surfactant to the surface area of an alveolus (*i.e.*, m_{surf}/A_{alv}). The surfactant mass in one single alveolus is 3.35×10^{-10} g [37]. The pressure due to surface tension is determined by Laplace's law.

As P_{tm} changes at every time step, the edge length of an alveolus, l_{alv}, is computed at quasi-steady state using the force balance equation. The volume of an alveolus (truncated octahedron) is computed as $8\sqrt{2}l_{alv}^3$, and surface area of an alveolus is solved as $(6 + 12\sqrt{3})l_{alv}^2$. The alveolar space volume (V_A) is then computed as the product of the number of alveoli and the volume of a single alveolus (V_{alv}). The number of alveoli is set to be 600 million [43]. As such, we have the needed V_A that will be used in determining alveolar capacitance.

The fluid (hydraulic) capacitance (C_f) represents the potential energy storage element. It is a combination of three components: open reservoir effects (C_{reserv}), elasticity/compliance effects

(C_{compl}), and fluid compressibility effects (C_{compr}), as shown in Equation 1.5.

$$C_f = C_{reserv} + C_{compl} + C_{compr} \tag{1.5}$$

During normal breathing, the potential energy storage due to the air compressibility effect is negligible (that is, $C_{compr} = 0$), since air pressure in the lungs is about one cmH2O [7]. Approximating air to an ideal gas, the potential energy storage in the alveolar space due to open reservoir effect (C_{reserv}) is then derived from the ideal gas law, $C_{reserv} = V_A/\rho RT$, where R is the ideal gas constant, ρ is the density, and T is the temperature. The compliance effect is derived as the ratio between the change of alveolar volume and the change of alveolar pressure, $C_{compl} = \Delta V_A/\Delta P_A$. We then compute the alveolar fluid capacitance (C_{alv}) as:

$$C_{alv} = \frac{V_A}{\rho RT} + \frac{\Delta V_A}{\Delta P_A} \tag{1.6}$$

Simple calculations show that C_{reserv} is two orders of magnitude smaller than alveolar compliance C_{compl}. Therefore, we conclude that the lung compliance effect serves as the main determinant of potential energy storage in the lungs. As such, we now use the terms capacitance and compliance interchangeably throughout the chapter.

The LM module has four dynamic equations and four unknown pressures (at the four nodes in where gravity gradient is negligible. The alveolus volume can then be determined by the transmural pressure (P_{tm}) that changes in time. The following describes the empirical relations of the fiber forces that relate fiber force/stress to alveolus dimension, and the assumptions of fiber distribution on a single alveolus 2A). For non-sedated patients, P_{pl} serves as the input of the model. The time-varying alveolar compliance, computed as a function of surfactant concentration (Equation 1.4) and fiber (elastin and collagen) elasticity (Equation 1.3 for collagen and the linear stress-strain function for elastin), is fed into the LM module at every simulation step. The LM

variables and the pulmonary diseases (*i.e.*, ARDS and IPF) can thus be simulated as results of the surfactant concentration and the lung fiber elasticity.

1.3 Results

In this section, we first present the model sensitivity analysis to show the effects of model parameters on the lung mechanics variables. Then, we perform model simulation and validate on healthy non-ventilated subjects and ventilated ARDS or IPF patients, along with the corresponding interpretation and analysis. To validate the model in healthy conditions, we compare the proposed model to 1) an accepted lung model with a constant alveolar compliance value, and 2) measured healthy human flow data. To validate the model in diseased conditions, we compare the model to ARDS and IPF human data. Finally, we assess the robustness and stability of this dynamic system.

1.3.1 Sensitivity Analysis

To evaluate the effects of model parameters (collagen volume (V_{col}), collagen elasticity coefficients (c_1, c_2, and c_3 from Equation (1.3)), surfactant concentration (Γ), hydraulic resistances, and hydraulic capacitances) on the LM variables, we performed a sensitivity analysis of the lung mechanics variables to changes in parameters via sigma (Σ) values, as shown in Table 1.2. Sigma values were computed to quantify the sensitivity, as $\frac{\Delta Variable \times Parameter}{\Delta Parameter \times Variable}$. The sigma value is a measure of the effect of the change in parameters to changes in variables, where parameters represent material property and geometry of the system (first column of Table 1.2), while variables are the system outputs (first row of Table 1.2). A bigger Σ value indicates a higher sensitivity. Each sigma value is computed using a change in a parameter and corresponding changes in variable. For comparison purposes, we have selected a common range of parameter change in Table 1.2 (50% decrease to a 100% increase in 10% increments). The range -50% to

100% corresponds to halving and doubling each parameter, thereby covering a reasonable range to study negative and positive changes of the nominal value. A mean sigma was then generated for each parameter (across all variables) and reported in the cells of Table 1.2. As seen, surfactant concentration is the most sensitive parameter across all lung mechanics variables and has an average sensitivity of 1.17 (computed from the 2nd row). The alveolar elasticity parameter, c_2, is the second highest sensitive parameter, across all variables, and has an average sensitivity of 0.71. Among the three collagen elasticity parameters (c_1, c_2, and c_3) in Equation (1.3), c_3 has the least impact on the LM variables, when compared to c_1 and c_2. The collagen volume (V_{col}) is the fourth sensitive parameter. The compliances of the upper airways (C_l, C_{tr}, C_b) were the least sensitive parameters, followed by some of the resistances (R_{tb} and R_{lt}) of the upper airways. This observation was expected since parameters affecting the alveolar compartment (and not the upper airways) are the main determinants of respiratory conditions such as ARDS and IPF, as mentioned in the Introduction, [4]–[9].

Table 1. 2: Sensitivity results

Σ	P_A	V_A	Q	V_{lung}	P_b	P_{tr}	P_l	Mean
V_{col}	0.114	0.313	0.214	0.294	0.113	0.113	0.112	0.182
Γ	0.929	1.492	1.630	1.396	0.921	0.916	0.915	1.171
c_1	0.148	0.242	0.394	0.227	0.146	0.147	0.144	0.207
c_2	0.496	1.138	0.826	1.066	0.492	0.490	0.488	0.714
c_3	0.038	0.108	0.240	0.101	0.047	0.038	0.036	0.087
R_{ml}	0.195	0.074	0.148	0.074	0.217	0.332	0.541	0.226
R_{lt}	0.071	0.037	0.074	0.034	0.080	0.121	0.111	0.075
R_{tb}	0.069	0.029	0.074	0.027	0.076	0.098	0.097	0.067
R_{ba}	0.128	0.081	0.069	0.079	0.144	0.225	0.226	0.136
C_l	0.019	0.064	0.022	0.060	0.019	0.018	0.019	0.032
C_{tr}	0.037	0.047	0.016	0.045	0.037	0.035	0.036	0.036
C_b	0.023	0.068	0.025	0.029	0.024	0.024	0.024	0.031

Table 1.2 quantifies the sensitivity of the lung mechanics variables to parameter change. c_1, c_2 , c_3 : coefficients in collagen stress-strain function; V_{col} : collagen volume; Γ : surfactant concentration; V_{lung}: lung volume; Q: total airflow; l: larynx; tr: trachea; b: bronchi; A: alveoli; ml: mouth to larynx; lt: larynx to trachea; tb: trachea to bronchi; ba: bronchi to alveoli; P: hydraulic pressure; C: capacitance.

Figure 1.4 shows the effects of the variations of collagen volume, surfactant concentration and c values on static transmural pressure vs alveolar volume (PV) curves in the subplots (Figure 4A-E), respectively. Every curve in Figure 1.4 represents a severity level that is defined by the magnitude of a parameter change (increase by 2, 4, 6 times, or decrease by 20%, 40%, 60%). The severity levels indicated follow ARDS simulation by Fujioka *et al.* [37]. Alveolar volume in Figure

1.4 is normalized by total lung capacity (TLC) in order to compare patients with different body weights (lung volume). As reflected in Table 1.2 and Figure 1.4 (subplots C-E), lung pressures and volumes are not sensitive to c_3 compared to the other collagen elasticity coefficients (c_1 and c_2). As we analyze the subplots of the sensitivity analysis shown in Figure 1.4, the subplots A and B reveal that an increase in collagen quantity and/or a decrease in surfactant concentration create stiffer lungs, a fact which agrees with clinical findings [10][11][15]–[17]. In Figures 1.4A and 1.4C, we find that the inflection points shift to the right as severity level increases. Figure 1.4B shows that a decrease in surfactant concentration flattens the PV curves, especially in the low-pressure range. Further, the slopes of the curves (compliances) rise faster as surfactant concentration (Γ) decreases (severity level increases), and all curves reach the same alveolar volume at high pressures. Figure 1.4B also shows that once pressure exceeds the alveolar threshold opening pressure, the alveoli are open and lung volume increases according to their elastic properties. This threshold opening pressure may be higher for the lower surfactant concentrations, as shown. In Figure 1.4D, PV curves show high sensitivity of pressures and volumes to changes in c_2. When c_2 decreases, not only do the lungs get stiffer (lower slope), but also the maximum alveolar volume is reduced at high P_{tm}. More interpretation of the sensitivity results can be found in the Discussion section.

Hence from the sensitivity results, LM variables are sensitive to 1) the surfactant concentration (Γ), 2) the collagen elasticity parameters (c_1, c_2) in Equation 1.3, and 3) the collagen volume (V_{col}). Clinical studies also support the fact that ARDS and IPF patients have abnormal Γ, c values and V_{col} [4]–[9], we thus simulate ARDS and IPF by varying these parameter values.

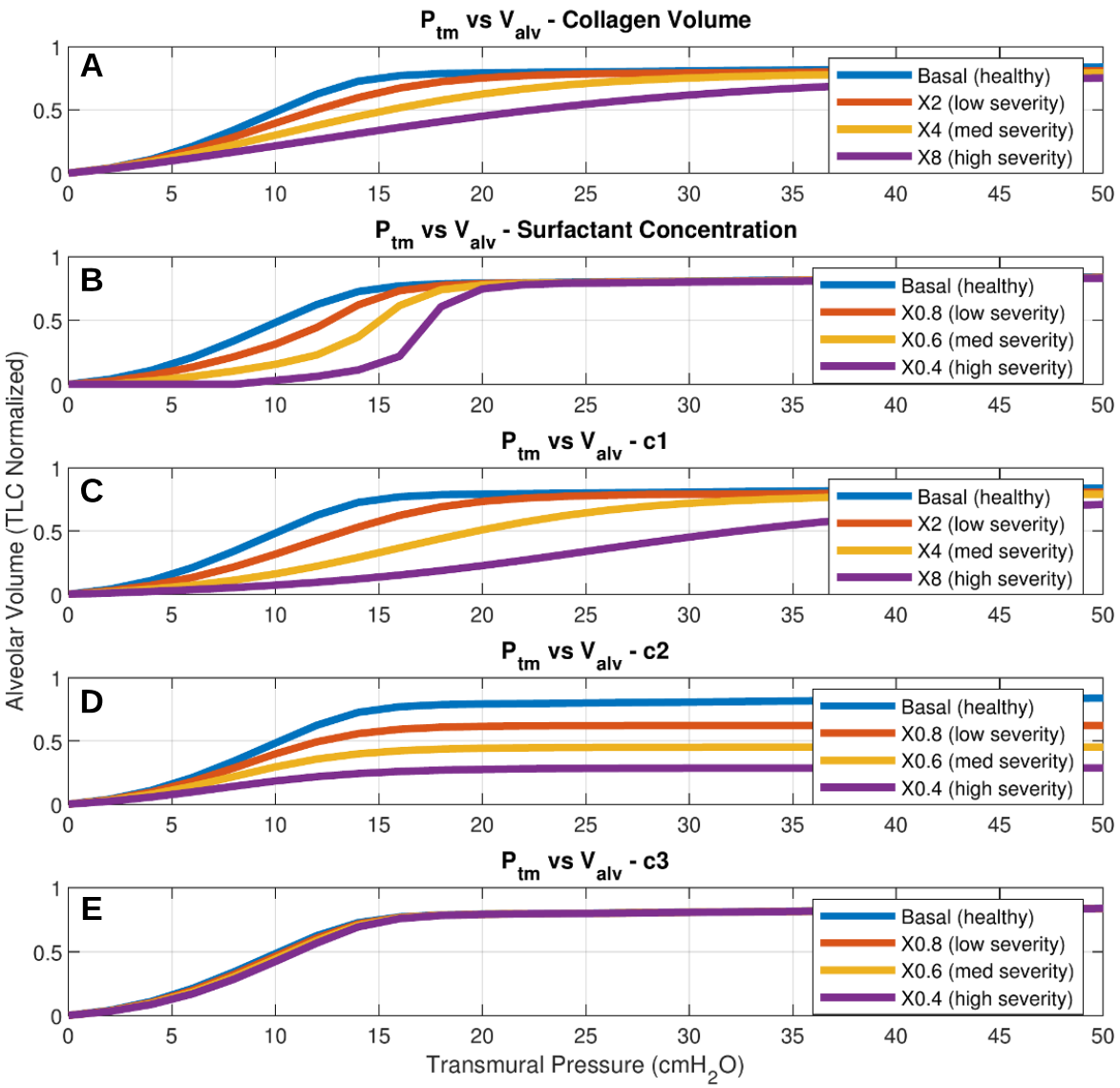

Figure 1. 4: Sensitivity of alveolar volume (total lung capacity (TLC) normalized) and transmural pressure to the change of collagen volume (A), surfactant concentration (B), *c* values in collagen stress-strain function: Equation 1.3 (C-E).

1.3.2 Simulation and Validation for Healthy Subjects

As a first validation step, we compare the proposed model to a published model [1] for a healthy non-ventilated human. Simulation of normal (healthy) breathing is shown in Figure 1.5 (blue curves). The model's lung mechanics variables (solid blue), airflow, alveolar pressure and alveolar volume, are plotted with respect to time and compared to an accepted model (dashed blue) [1]. Our

simulation results show that the alveolar pressure becomes negative during inspiration and returns to positive during expiration (varying between -0.6 and 0.98 cmH_2O). This trend is expected since the airflow follows the pressure gradient between the P_{ao} and P_A nodes of Figure 1.2A, as airflow is positive during inspiration and negative during expiration. The lower panel in Figure 1.5 shows a tidal volume of 500 ml, which agrees with values reported for normal subjects in literature [7]. Our model also reveals a close match to the accepted pulmonary mathematical model (from Albanese *et al.*) [1] — such a model was validated with experimental data from healthy subjects under different environmental conditions [44]. The slight difference between the blue solid and blue dashed curves in Figure 1.5 is expected since the proposed model adopts a time-varying alveolar compliance, while [1] assumes a constant alveolar compliance of 0.2 L/cmH_2O. The comparison between the two model simulations in Figure 1.5 indicates that our proposed model generates waveforms that resemble those predicted by [1]. This observation serves as a preliminary validation of our model.

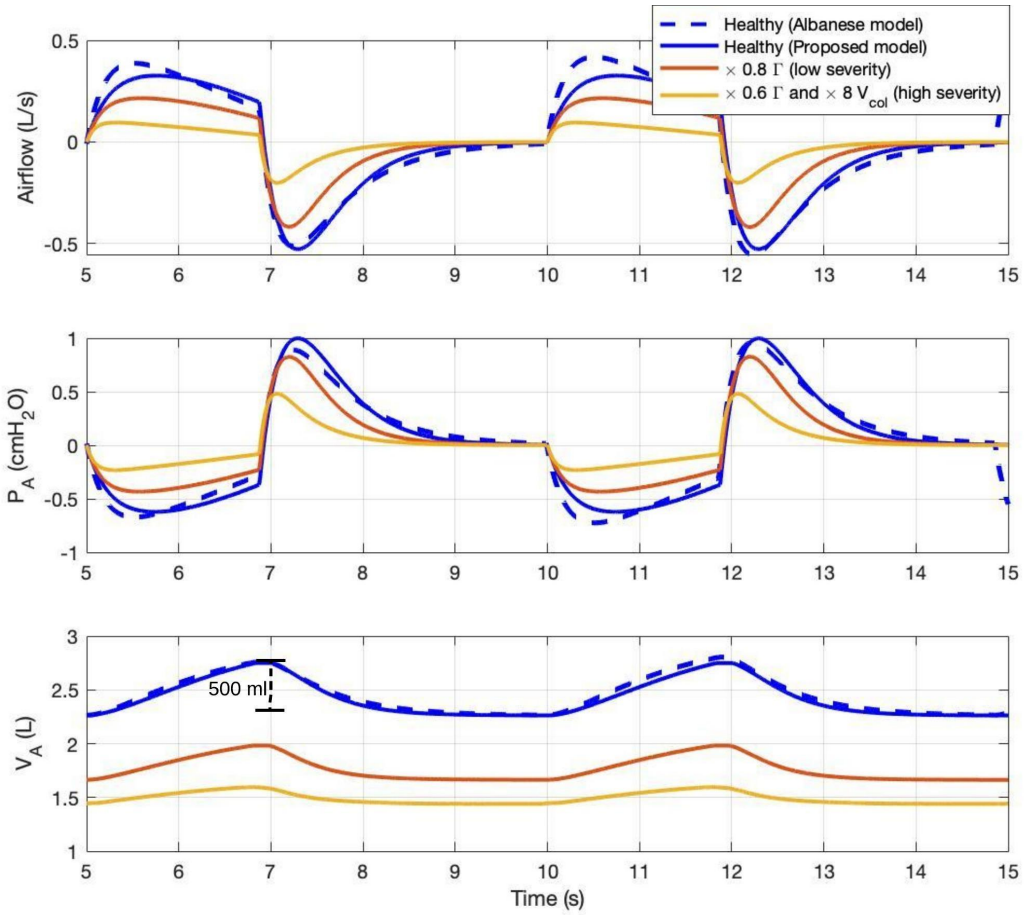

Figure 1. 5: Model simulation of a healthy subject during normal breathing (blue) compared to Albanese's model simulation (blue dashed) [13], and ARDS model simulation with two severity levels (red and yellow): 1) 20% reduction in surfactant concentration, and 2) 40% reduction in surfactant concentration and 8 times more of collagen volume. Airflow, alveolar pressure, and alveolar volume waveforms are shown.

Figure 1.6 compares our model-simulated airflow to a healthy (non-ventilated) person's airflow as reported by Proctor [20]. In order to match the experimental breathing pattern in [20], we tuned the parameters in Equation (1.1) to determine the P_{pl} profile (the model's forcing function) in order to match the patient flow waveform: we approximated I:E ratio as 0.45, τ as 0.627 s, and magnitude of P_{pl} as 6.5 cmH_2O. Using this new input and nominal (healthy) parameter values of Table 1.1, our model calculates an airflow waveform that is close to the real human data (root mean squared

error: 6.79 L/min). The proposed model emulates healthy patient well since, besides the model input, neither the model parameters nor the equations were changed to fit the human data.

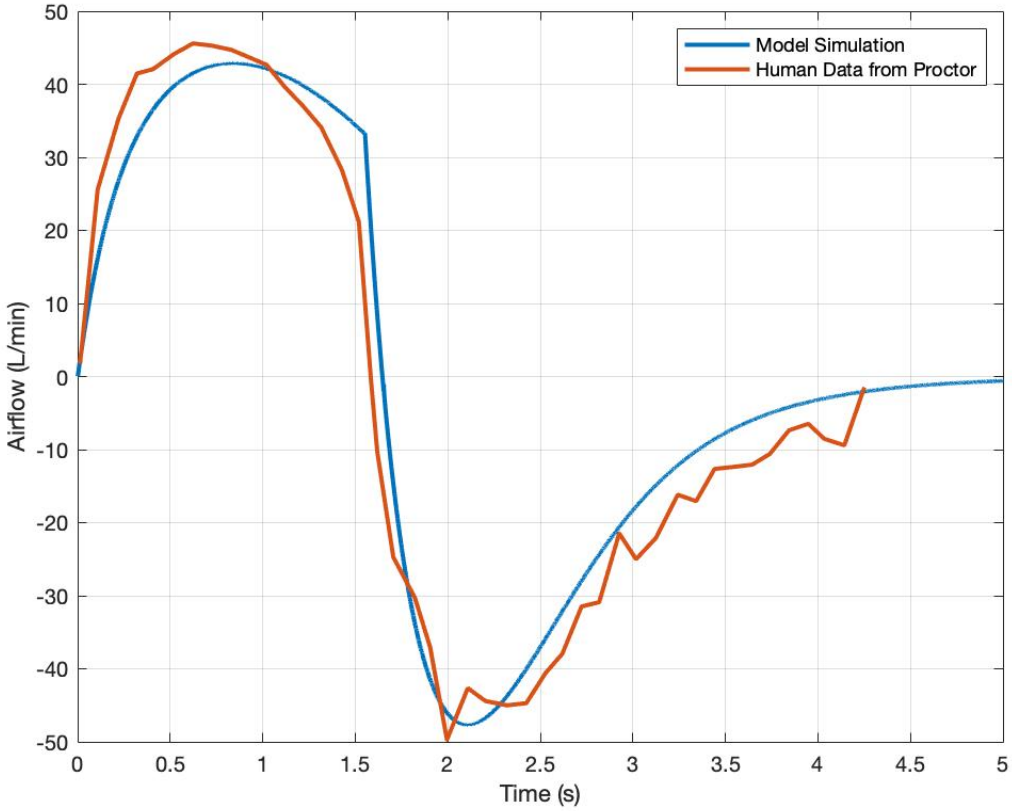

Figure 1. 6: Airflow validated against healthy human data from Proctor *et al.* [11]. Red curve represents healthy human data, and blue curve represent simulation results.

1.3.3 Simulation and Validation for Patients with ARDS or IPF

As described in the sensitivity analysis, pulmonary conditions such as ARDS and IPF are greatly affected by, and can be understood as, changes of these four parameters ($\Gamma, V_{col}, c_1, c_2$) that represent the surfactant concentration, collagen quantity, and collagen quality. In the following sections, we present the simulation results of the time-varying compliance waveforms and the corresponding LM variables under diseased conditions for non-ventilated patients. We then validate our model with ARDS and IPF patient data by tuning these four parameters so the simulation matches experimental results.

In Figure 1.7, the simulated time-varying compliance waveforms for healthy subjects and diseased nonventilated patients are shown. The solid blue curve represents the simulation of normal subjects whose compliance values oscillate around 0.16 L/cmH_2O with a magnitude of 0.045 L/cmH_2O. The purple dashed line represents the constant alveolar compliance that Rideout and Albanese *et al.* adopted in their models [1], [28]. They reported similar LM variable waveforms as ours, as presented in Figure 1.4. The red and yellow solid curves are the compliance waveforms simulation, using the parameter change for ARDS patients from Fujioka *et al.* [37]. The red curve (low ARDS severity) has 20% reduction in surfactant concentration, and the yellow curve (high ARDS severity) has 40% reduction in surfactant concentration as well as 8 times increase in basal collagen volume. The ARDS simulation with a high severity level generates a compliance curve that barely oscillates since the lungs are much less elastic. The yellow compliance waveform reaches a value close to 0.04 L/cmH_2O, which matches the severe compliance reported in the literature as shown in the green dashed curve [45], [46]. Note that the simulated time-varying compliance shown in Figure 1.7 is bounded between the static healthy and diseased compliance values from literature, further supporting the simulation results.

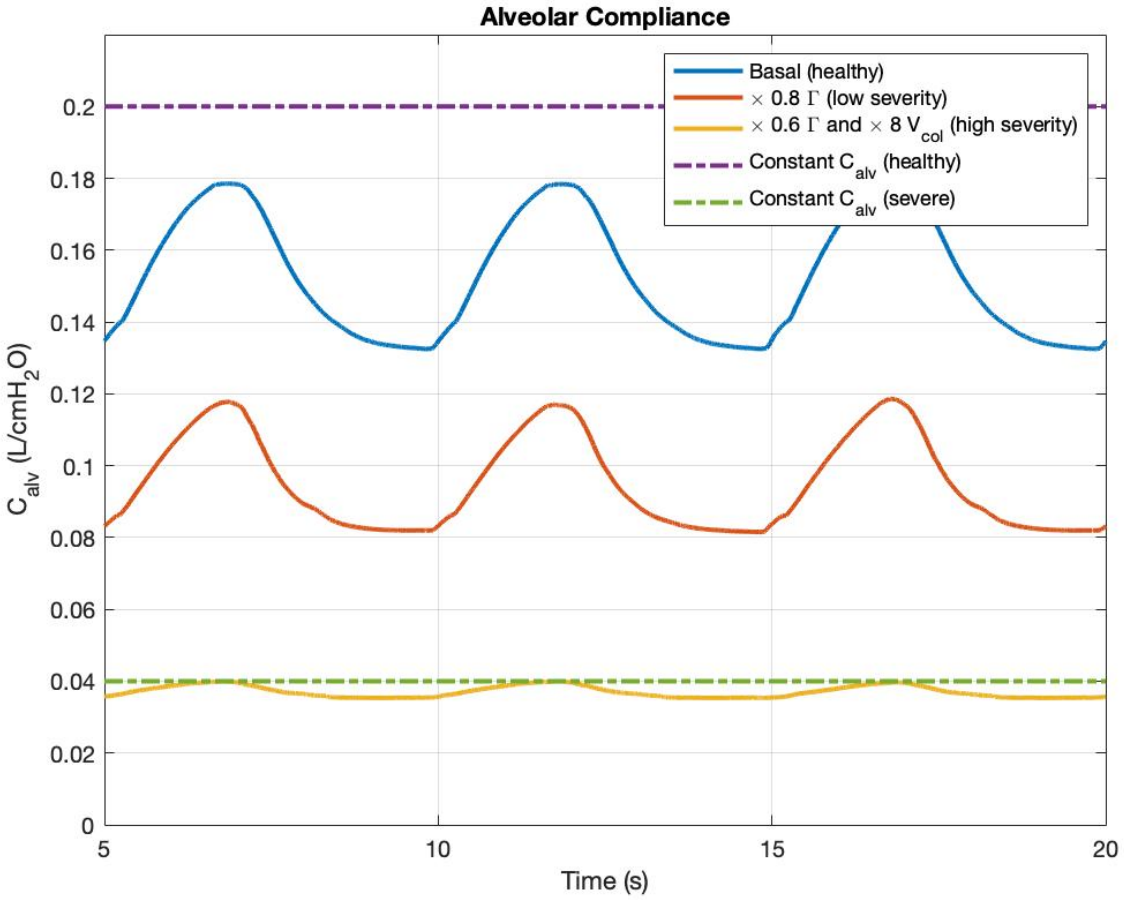

Figure 1. 7: Time-varying alveolar compliance waveforms under two severity levels: 1) 20% reduction in surfactant concentration, and 2) 40% reduction in surfactant concentration and 8 times increase in basal collagen volume. Purple dashed line is the constant alveolar compliance value adopted by Rideout [20]. Green dashed line represents the severe alveolar compliance value in ARDS [40], [41].

The resultant LM variables in time (airflow, alveolar pressure, and alveolar volume) with time-varying compliances are shown in Figure 1.5 for healthy subjects (blue) and diseased nonventilated subjects (red and yellow curves). As alveolar compliance decreases (disease severity level increases), all LM variables exhibit peak-to-peak decreases. Tidal volumes are reduced and airflow and pressure reach lower peaks as compared to healthy patient simulation. The tidal volume reduced to approximately 150 ml from a normal value of 500 ml (77% reduction). This is expected due to the increased stiffness of the lungs. The low tidal volume in the high-severity case also indicates

the need for exogenous ventilation.

ARDS human data from three different studies [21]–[23] were obtained to validate our model. All patients were fully sedated and intubated with mechanical ventilator support. Orfao *et al.* [22] reported a mean PV curve from 23 ARDS patients, plotted as the dashed black line in Figure 1.8. The reported lung volume is normalized by total lung capacity (TLC), which was estimated from the sigmoidal fitting function: $V = a + \frac{b}{1+e^{-(P-c)/d}}$, where $a, b, c,$ and d are four fitting parameters. The TLC can be estimated from $a + b$ or read from the upper asymptote by considering the pressure interval from 0 to 100 [22]. The sigmoidal function has been shown to fit the PV curve, and it is a well-accepted approximation for understanding the lung mechanics of ARDS patients when appropriately tuned [22], [30]. The transmural pressure in Figure 1.8 is determined by the difference between P_A and P_{pl}. The pleural cavity pressure shows positive swings as the ventilator blows air into the lungs tidally. Assuming nominal chest wall compliance (C_{cw}) of 0.2445 L/cmH_2O [1], pleural cavity pressure is equal to $\frac{V_A}{C_{cw}}$. Using the low and the high severity defined in Figure 1.5, we generated two independent PV curves (blue solid) that envelop the mean PV curve. This is expected since the two border PV curves are determined with the extreme parameter change following the work by Fujioka *et al.* [37].

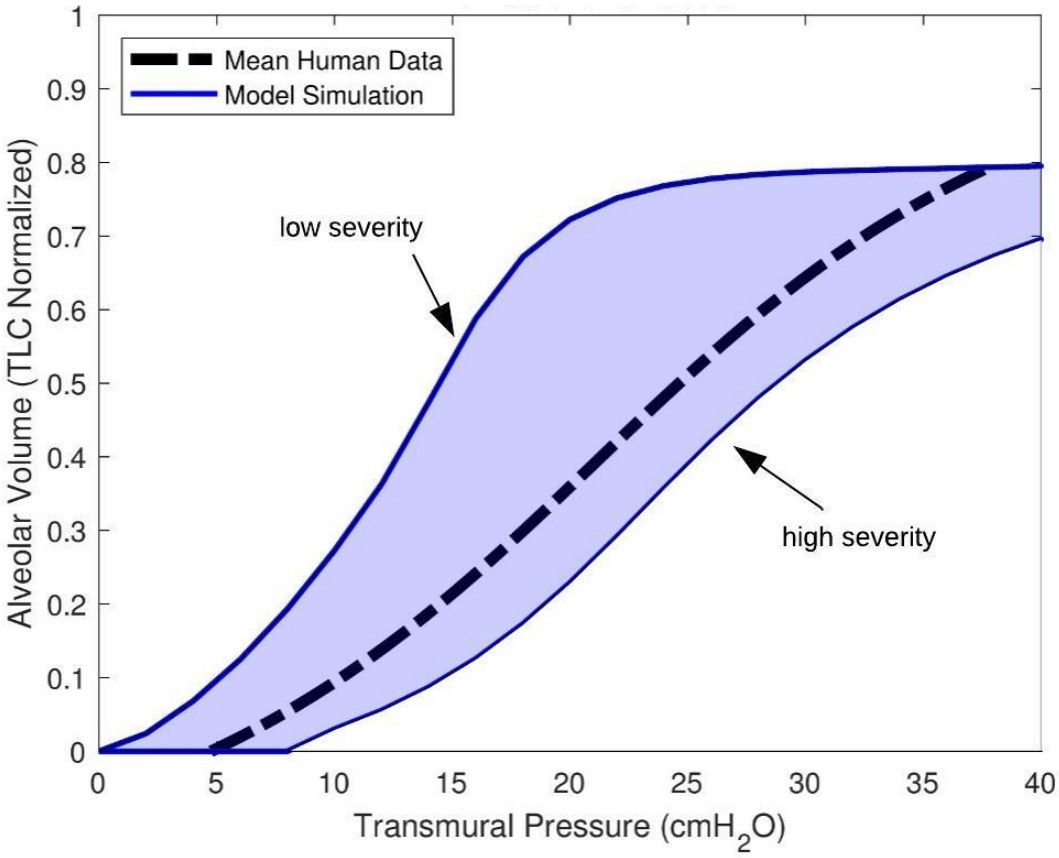

Figure 1. 8: Model validation against mean PV data from 23 ARDS patients (dashed curve). Two border lines were simulated with low and high severity levels as defined in sensitivity analysis. The blue shadow covers the area of general ARDS PV curve data according to our simulation.

Orfao, Servillo, and Pereira [21]–[23] each reported PV data for one ARDS patient, plotted in black, blue, and green dashed lines in Figure 1.9, respectively. The sensitive and disease-important parameters for the ARDS patients, namely Γ and V_{col}, are determined via exhaustive search to match the literature-reported PV curves. Once the parameters are estimated, we fix the set of the disease-related parameters, and generate this patient's PV curve from the model to compare to the data reported in literature. The R^2 values computed from comparing the model-simulated and literature-reported PV curves are reported in Table 1.3 along with the corresponding parameter scaling factors applied to fit the model to the data. The model approximates the physical data

reasonably well. In Figure 1.9, the simulated PV curves with the estimated parameters also agree with the sensitivity analysis (Figure 1.4). As noted, Pereira's ARDS data is flatter at low pressure (steeper S-shaped) than the other two (Orfao's, Servillo's) PV curves, indicating a reduced surface tension effect, as learned from Figure 1.4B. As a result, a greater reduction of Γ was indeed needed to emulate the Pereira patient data, as compared to the Orfao or Servillo patient data. The estimated parameter variations of the three ARDS patients are reasonable since the scaling factors are between the low and high severity as defined earlier. Also, the collagen volume change in ARDS patients were quantified by Saldiva *et al.* [47]. In their study, the color intensity of stained lung tissue showed that collagen volume of ARDS patients can increase by 2.7 times (and more than 10 times for a severe case) compared to a normal patient group on average.

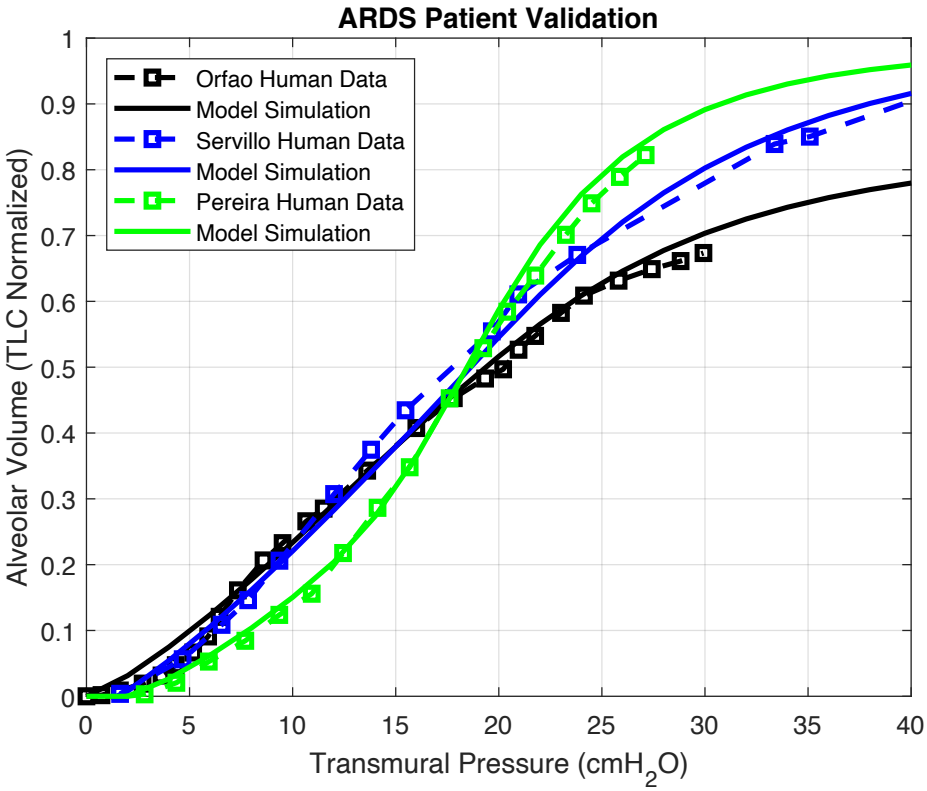

Figure 1. 9: Model validation against ARDS patient data from three references [13]–[15]. Dashed lines represent ARDS patient data, and solid lines represent model simulation results.

The proposed model is also employed to compute pulmonary elasticity (PV curves) of IPF patients. Six IPF patients' PV curves were reported in [24]. All patients were fully anesthetized and intubated with mechanical ventilator support. IPF is a disease resulting from collagen degradation and increase in quantity. Since c_3 does not greatly affect lung mechanics variables, according to the Sensitivity Analysis, and the IPF pathophysiology does not support a decrease in Γ for IPF patients, we simulate IPF by exhaustively searching for the optimal c_1, c_2, and collagen volume only. To compare different patients and to compare patient data to model simulation, we normalized the reported lung volumes by TLC values. Table 1.3 summarizes the multiplicative factors applied to the healthy parameters and R^2 values from comparisons of model-simulated and literature-reported PV curves. A multiplicative factor of 1 means that either the nominal or the healthy parameter value was used. Figure 1.10 shows all six patients' data along with our simulation results. Our model-simulated PV curves match the six patients' data well. The model simulates IPF data of patient 1 by an eightfold increase in c_1. This result agrees with the sensitivity analysis, as the first order derivative of the patient's PV curve is monotonically increasing, which is similar to the effect of altering c_1 in Figure 1.4C. This result also agrees with findings by Fulmer [16] that certain IPF patients do not have an increase in collagen volume in the lungs. Other IPF patients require a combination of both the elastic properties of collagen and its volume. For example, the PV curve of patient 2 is flatter and the total lung capacity is low even at high pressures. This implies a greater increase in collagen volume (as seen in Figure 1.4A) and a reduction in c_2 (as seen in Figure 1.4D), which agrees with the estimated parameters. The alterations in collagen volume that emulate the reported patients' data also fall in the V_{col} range as reported by Saldiva *et al.* [47]. Saldiva *et al.* reported that IPF patients have an average of 3.9 times increase in the collagen volume compared to a normal patient group, and a severe case can have an increase of more than 10 times.

Table 1. 3 Parameter Scaling factors for ARDS and IPF Patients

ARDS Patients			
Patient References	V_{col}	Γ	R^2
Orfao [15]	6	0.9	0.9973
Servillo [14]	6.5	0.8	0.9937
Pereira [16]	4	0.58	0.9794
IPF Patients			
Patient ID	c_1	c_2	V_{col}	R^2
Ferreira [17] - 1	8	1	1	0.9907
Ferreira [17] - 2	0.7	0.5	6	0.9949
Ferreira [17] - 3	0.7	0.61	4.5	0.9943
Ferreira [17] - 4	2.4	0.78	4	0.981
Ferreira [17] - 5	1.8	0.5	8	0.992
Ferreira [17] - 6	0.3	0.75	1.6	0.9926

R^2: coefficient of determination; c_1, c_2: coefficients in collagen stress-strain function; V_{col}: collagen volume; Γ: surfactant concentration.

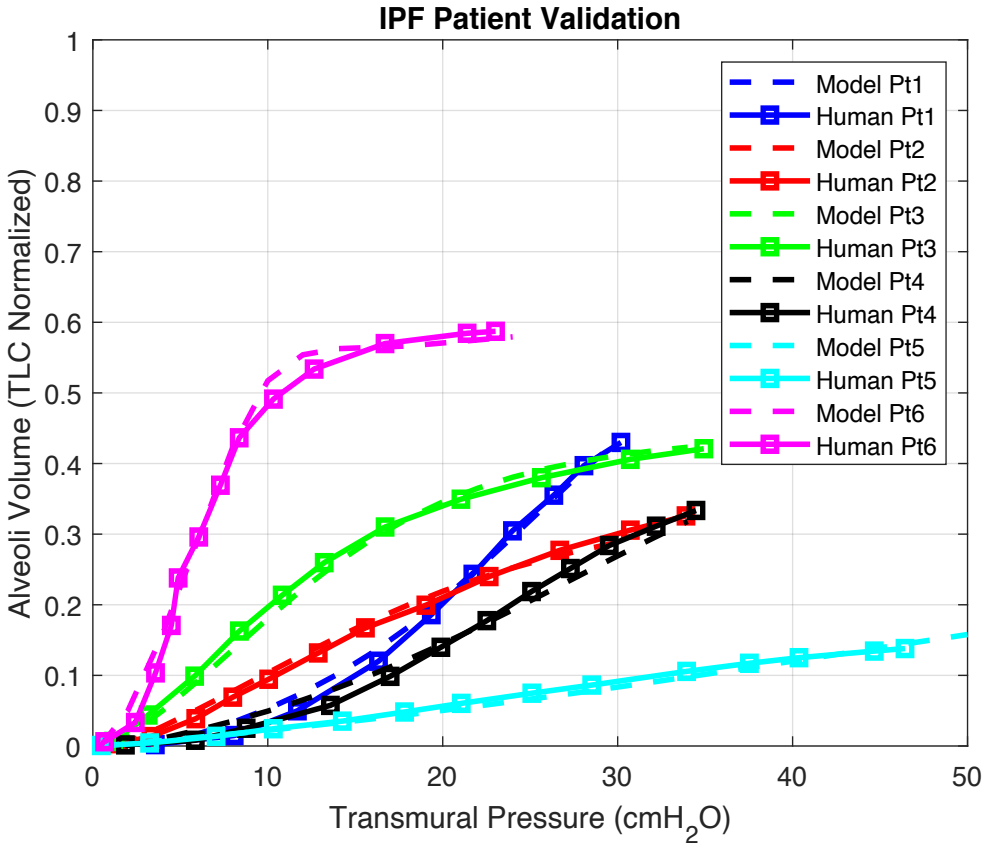

Figure 1. 10: Model validation against six IPF patients [16]. Solid lines represent real IPF patient data, and dashed lines represent model simulation results.

1.3.4 Model Stability and Robustness Assessment

To assess the stability and robustness of the proposed model, we perform an eigenvalue analysis, generate phase plane plots for unperturbed and perturbed long-time simulations, and assess feasible parameter ranges. To prove the dynamic stability, we first linearized the time-varying C_{alv} in order to formulate the dynamic system into a state-space form, and the state equation can be found in the Appendix. The computed eigenvalues of the state matrix all have negative real parts, namely, -4631.8,-1579.4, -740.2, and -2.7, indicating stability of the linearized model. For numerical stability we have simulated the model for more than 4000 breaths (300+ simulation hours) on a 2.9GHz 8GB machine and plotted the PV loops for healthy (blue), low severity (red) and high severity (yellow) levels as shown in Figure 1.11. The system output loops (pleural cavity pressure vs alveolar volume) are closed, indicating a well-behaved system under both healthy (unperturbed) and diseased (perturbed) cases. Through these analyses, system stability is maintained when multiplicative factors perturbing the parameters (representing lung diseases) are bound by the following limits: $V_{col} > 0$, $\Gamma \geq 0$, $c_1 > 0$, and $0 < c_2 \leq 1$. Note that physiological systems typically have positive-only parameters, since negative parameter values do not have physical meaning.

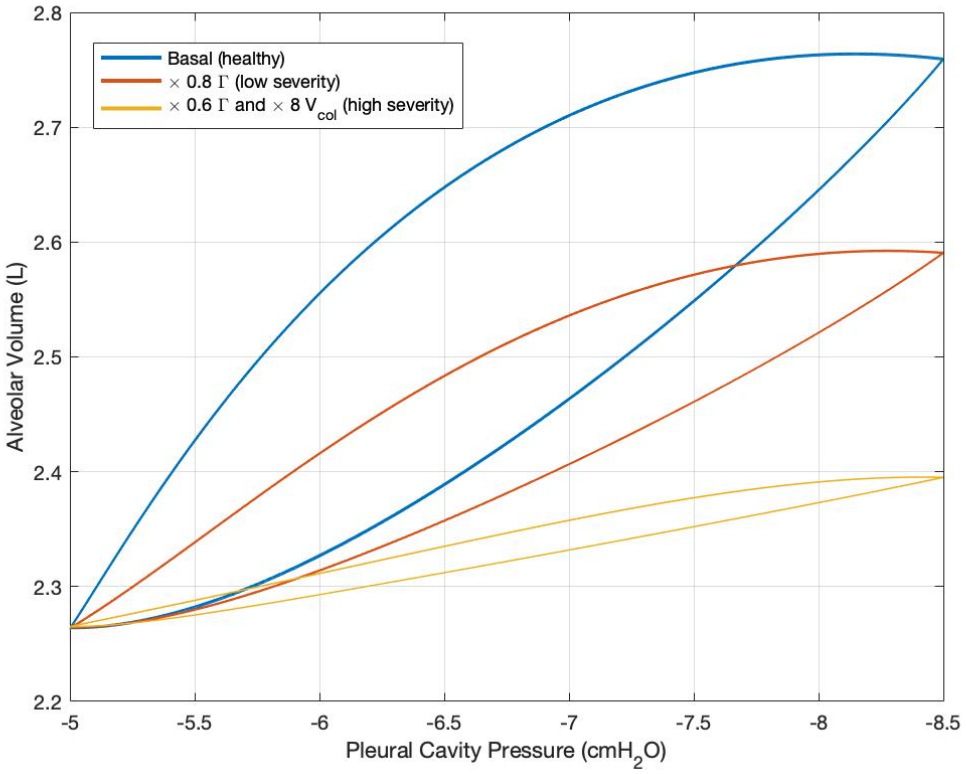

Figure 1. 11: PV loops for long-time breathing simulation in healthy (blue), low severity (red) and high severity (yellow) sickness levels. Low severity: 20% reduction in surfactant concentration. High severity: 40% reduction in surfactant concentration and 8 times increase in basal collagen volume.

1.4 Discussion

The lung is often modeled as an *RC* circuit, where *R* represents the hydraulic resistance and *C* represents the compliance of the whole respiratory system. Such a model can be used to describe dynamically the lung pressure and flow reasonably well, by first assigning values for *R* and *C*, and then solving, a system of 1st order ordinary differential equations (ODEs), for the pressure and flow in time. Disease simulation is then accomplished via changing the parameters *R* and *C* and again solving the ODEs. In such simulations, ARDS, IPF, and other compliance-compromised conditions would all be modeled in a similar fashion, *e.g.*, change *C* and then solve for flow and pressure. In the present work, however, ARDS, IPF, and other compliance-compromised

conditions can be modeled through the mechanisms that cause compliance changes, such as collagen remodeling or surfactant degradation. In this way, a deeper level of understanding of respiratory dynamics is achieved through more rigor in the model.

In this study, we presented a mechanistic model of the respiratory physiology, specifically how alveolar tissue fibers and surfactants affect lung compliance and breathing. The model validated reasonably well against ARDS and IPF patient data demonstrating its possible use to run what-if scenarios simulating lung conditions and diseases. Interestingly, through simulations of severe disease, we find that lung volumes are extremely low, indicating the need for interventional ventilatory support. Additionally, PV curves of severe disease simulations (increased collagen, decreased elasticity, decreased surfactant) have inflection points that are shifted to the right, indicating stiffer lungs and a greater pressure required to achieve the same volume. In some cases, such as severely reduced surfactant concentration, the PV curve remains nearly flat at low pressure levels, suggesting that more pressure is required to overcome the alveoli threshold opening pressure and supporting the use of high PEEP (positive end-expiratory pressure) to prevent alveolar collapse in ventilating ARDS patients [48].

Through the sensitivity analysis presented, we have confirmed that parameters that determine the health of the alveolar space, such as surfactant concentration (Γ) and collagen fiber properties (c values and V_{col}), have a greater impact on lung mechanics variables (lung pressure, flow, and volume) than resistances and compliances of the upper airways. The role of these important parameters is supported in the literature. In ARDS, excess fluid accumulation in the lungs affects the concentration of pulmonary surfactant significantly, which causes alveolar collapse, especially at low pressure ranges [4]. ARDS has also been shown to cause an increase in collagen volume [5]–[6]. IPF, on the other hand, which is characterized by scarring and destruction of the lung

architecture, tends to be a chronic disease with an excessive increase of collagen volume [49], and polymorphism [15]–[17]. Our model can differentiate between ARDS (via Γ and V_{col}) and IPF (via c_1, c_2, and V_{col}) since all these parameters appear explicitly therein.

Further, with the linearized version of this model and system identification techniques, we can estimate not just compliance changes but fiber or surfactant properties that caused these changes. In this way, the model can also simulate some COVID patients who resemble ARDS patients in that they have compromised compliance. According to Gattinoni [19], 20-30% of the COVID patients admitted to the intensive care unit have severe hypoxemia associated with low compliance values. These COVID patients with compromised compliance can potentially be simulated via this model.

While we present a time-varying compliance in this work, we have not yet modeled the development of ARDS or IPF in time, which may be of importance in ARDS, as the lungs often show signs of fibrosis or fibrotic scarring in late or severe stages [5]–[6]. However, with real-time parameter estimation we may be able to continually estimate these parameters to assess how they are changing and how the condition is progressing or deteriorating. Furthermore, though the model satisfies the need to understand compliance change during a breath cycle, its effect on LM variables is more prominent in diseased lungs than it is in healthier ones.

1.5 Conclusion

In this chapter, we have developed a mathematical model of the lung mechanics comprising alveolar tissue and surfactant properties that generates reasonable lung pressures and volumes when compared to healthy, ARDS, and IPF patient data. The model describes a time-varying alveolar compliance that provides a better understanding of lung diseases. We have also shown,

through sensitivity analysis, that the surfactant concentration and the collagen stiffness parameter c_2 have a strong impact on lung mechanics variables. Further, the model has proven to be stable and robust under different disturbances.

The model is a set of ODEs that can be implemented to allow for what-if scenario testing via changing specific parameters. Using measurements for patient and a parameter estimation technique a personalized version of the model can be obtained. The research team is working toward model simulations that test different ventilation strategies for a specific patient, *e.g.*, varying ventilator settings (pressure and PEEP) to simulate the change of airflow, lung pressure and volume of that patient.

1.6 Appendix – State Equation

The state equation of the linearized model is shown below:

$$\begin{bmatrix} \dot{P}_l \\ \dot{P}_t \\ \dot{P}_b \\ \dot{P}_A \end{bmatrix} = \begin{bmatrix} -\frac{1}{C_l R_{ml}} - \frac{1}{R_{lt} C_l} & \frac{1}{R_{lt} C_l} & 0 & 0 \\ \frac{1}{R_{lt} C_t} & -\frac{1}{C_t R_{lt}} - \frac{1}{R_{tb} C_t} & \frac{1}{R_{tb} C_t} & 0 \\ 0 & \frac{1}{C_b R_{tb}} & -\frac{1}{C_b R_{tb}} - \frac{1}{R_{ba} C_b} & \frac{1}{R_{ba} C_b} \\ 0 & 0 & \frac{1}{R_{ba} C_{alv}} & -\frac{1}{R_{ba} C_{alv}} \end{bmatrix} \begin{bmatrix} P_l \\ P_t \\ P_b \\ P_A \end{bmatrix} + \begin{bmatrix} \frac{1}{R_{ml} C_l} & 0 \\ 0 & 1 \\ 0 & 1 \\ 0 & 1 \end{bmatrix} \begin{bmatrix} P_{atm} \\ \dot{P}_{pl} \end{bmatrix}$$

Chapter II: Respiratory Muscles and Rib Cage Mechanics – Mathematical Model Development and Validation with Patient Data

During quiet breathing, the periodic contractions of the respiratory muscles (diaphragm and intercostal muscles) cause a cyclic movement of the rib cage (expansion and shrinkage) that varies the pleural cavity pressure (P_{pl}). Inhalation and exhalation consecutively happen following the change of P_{pl}. In order to quantitatively study the human breathing mechanism of healthy and quadriplegic patients who breathe via phrenic paced diaphragm, we developed a physiology-based mathematical lung model that describes how contraction and relaxation of the respiratory muscles dictate human breathing. The proposed model includes: 1) a respiratory muscle and rib cage mechanics module that simulates the dynamic change of pleural cavity pressure in response to the motion of the rib cage and respiratory muscles, 2) a lung mechanics module that computes pressures and volumes of the lung compartments as P_{pl} changes. The contraction forces of the diaphragm and intercostal muscles (F_{dia} and F_{int}) drive respiration. In the model, these two forces are the excitatory inputs. Typically, they are not measured in patients, and are not available in the literature We, however, have calculated their shape and relative magnitudes using three invasively measured human signals found in the literature: displacement of the diaphragmatic central tendon, abdominal cavity pressure, and pleural cavity pressure. Once evaluated, we use them as model inputs and perform breathing simulations. The model outputs were validated with 1) healthy human data, and 2) a simplistic rib cage model, where P_{mus}, the combined respiratory muscle effect, and the integrated chest wall elastic property (C_{cw}), is adopted, and 3) quadriplegic patient data. The respiratory behavior of such patients, who breathe via isolated phrenic paced diaphragm, exhibits peculiar dynamics that our model has successfully captured.

2.1 Introduction

Respiration requires periodic contraction and relaxation of the respiratory muscles. Figure 2.1 shows the schematics of a human rib cage. As the respiratory muscles (diaphragm and intercostal muscles) contract, the pleural cavity expands, decreasing pleural cavity pressure (P_{pl}), generating a positive transmural pressure (P_{tm}) and subsequently expanding the alveoli (the gas exchange units). The alveolar expansion induces a decrease in alveolar pressure that leads to a pressure gradient between the mouth and the alveoli favoring the movement of air into the alveoli (and thus we breathe).

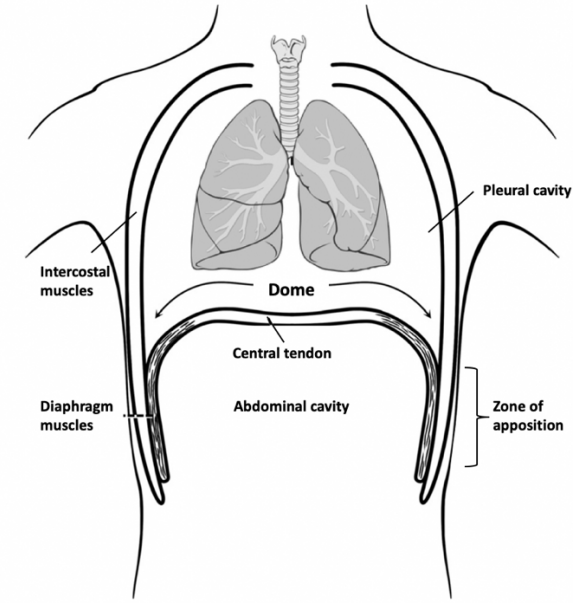

Figure 2. 1: Human rib cage schematics.

The respiratory muscles driving respiration comprise the diaphragm muscles, the intercostal muscles, and the accessory muscles. The diaphragm muscles are the main muscles that sustain ventilation. The intercostal muscles drive respiration to a lesser extent, compared to the diaphragm, while accessory muscles, such as scalene muscles, are conventionally considered inactive during quiet breathing [50].

The intercostal muscles are formed of two thin layers (external and internal) that span the intercostal spaces. During normal breathing, the contraction of the intercostal muscles facilitates breathing by expanding the rib cage laterally via rotating the ribs about the spine, similar to a bucket handle motion [51]. Because of the homogeneous distribution of the neurological control on the intercostal muscles' activity (contraction and relaxation), the 12 pairs of ribs move in the same direction during normal breathing. Thus, the entire chest wall is often conceptually considered as one compartment.

The diaphragm is a dome-shaped partition that separates the thoracic and abdominal cavities. It is composed of peripheral muscle sheets that originate from the circumference of the thoracic outlet and converge into the diaphragmatic central tendon. Figure 2.2 summarizes the respiratory muscle effects on P_{pl} as the direct diaphragm and intercostal muscle effects, and the diaphragm insertional and appositional effects [52], described as follows:

The diaphragm contraction pulls the central tendon caudally (toward the tail end of the body), flattening the diaphragm and increasing the vertical dimensions of the thoracic cavity (direct effect on P_{pl}) [53].

The insertional force exerted by the tension in the diaphragm muscles acts directly on the line of insertion to the thoracic outlet. This force pulls the lower ribs cranially (toward the head end of the body) and increases the horizontal dimensions of the thoracic cavity, shown as F_{dia}^{inser} in Figure 2.2.

The appositional force, generated by the abdominal cavity pressure, is applied on the inner aspect of the lower mediastinal wall, known as the zone of apposition (ZOA). As the diaphragm is activated during inspiration, its muscle fibers shorten and its dome (the central tendon) moves in the caudal direction. The descending of the diaphragmatic central tendon increases the

abdominal cavity pressure, generating an appositional force (F_{dia}^{appo}) on the ZOA. The F_{dia}^{appo} induces a torque that rotates the lower ribs, leading to an increase in the horizontal dimensions of the thoracic cavity.

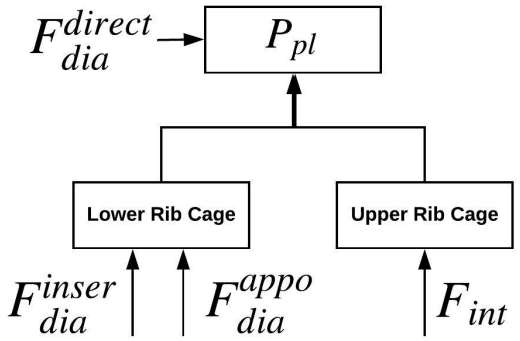

Figure 2. 2: Respiratory muscle effects on the rib cage and the pleural cavity. The diaphragm muscles 1) directly affect the pleural cavity pressure (F_{dia}^{direct}), 2) have an insertional effect (F_{dia}^{inser}) on the lower rib cage and 3) an appositional effect (F_{dia}^{appo}) on the lower rib cage, all of which alter the pleural cavity pressure. The intercostal muscles (F_{int}) expands the upper rib cage to affect the pleural cavity pressure.

A mathematical model of the human pulmonary system can be described via four modules as per Figure 2.3:

The respiratory muscles and rib cage mechanics (RMRM) module computes the motion of the rib cage (expansion and shrinkage) as the respiratory muscles contract and relax during quiet breathing. The pleural cavity pressure is computed in time as the volume of the rib cage changes. The variation of P_{pl} determines the inspiratory and expiratory flow, and it serves as an input to the lung mechanics module.

The lung mechanics (LM) module computes airflow, volumes, and pressures of different lung compartments (*i.e.* larynx, trachea, bronchi, and alveolar apace) in response to P_{pl} and the alveolar compliance (C_{alv}). Both P_{pl} and C_{alv} change in time, and they are computed from the RMRM module and the alveolus elasticity module, respectively.

The alveolus elasticity (AE) module quantifies the alveolar compliance as a function of the nonlinear tissue fiber elasticity and the surfactant concentration, both of which change depending on the health of the pulmonary system.

The gas exchange module computes the oxygen and carbon dioxide transport between the blood in the pulmonary capillaries and the gas in the lungs based on the airflow computed in the LM module.

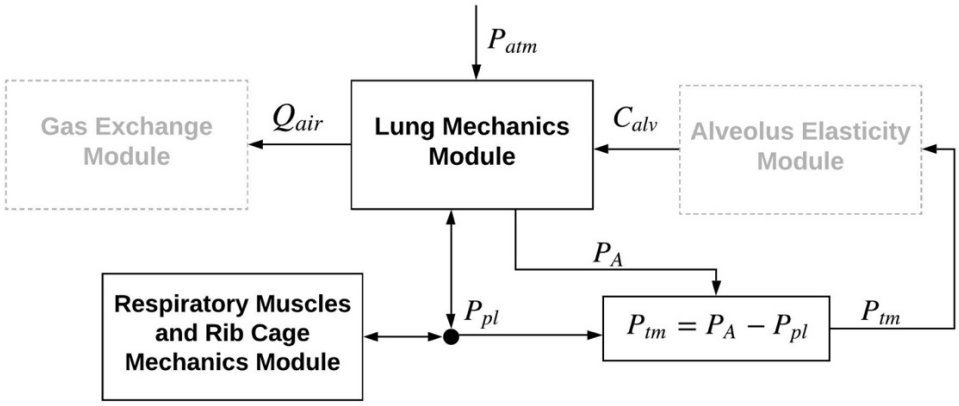

Figure 2. 3: Block diagram of mathematical lung modules that would make up the respiratory system. The full respiratory model comprises: lung mechanics, alveolus elasticity, respiratory muscles and rib cage mechanics, and gas exchange modules. P_{atm}: atmosphere pressure; P_A: alveolar space pressure; P_{pl}: peural cavity pressure; P_{tm}: transmural pressure; C_{alv}: alveolar compliance; Q_{air}: airflow into the lungs. The two modules highlighted in black are described in this work.

In this work, we focus on the first and the second module (RMRM and LM modules). The proposed lung model computes the change of the pleural cavity pressure as the result of the contraction and relaxation of the diaphragm and intercostal muscles. The LM variables (airflow, pressures and volumes of different lung compartments) are simultaneously determined by the changes of P_{pl} caused by the respiratory muscle efforts.

In the following, we first review other lung mathematical models published in the literature. Then we describe the development of the proposed lung model (modeling approach, parameters,

and equations). We then present simulation results and compare them to healthy human data [1], [54], [55] and quadriplegic patient data [56]. Finally, we conclude by summarizing the model performances, describing the limitations, and highlighting future extensions of this work.

2.2 Model Development

2.2.1 Literature Review

Mecklenburgh developed a simplistic lung model that consists of a compliance (C), a resistance (R), and a negative pressure source (P_{mus}) that represents the respiratory muscle efforts [57]. The model consists of one algebraic equation of motion that is easy to understand. This simplistic model was developed to test the performance of mechanical ventilators when ventilated patients breathe spontaneously. The Mecklenburgh model is often applied on mechanical ventilator related applications. For example, Vicario *et al.* applied the real-time estimation of R, C, and P_{mus} on ventilated patients in order to better provide mechanical ventilator support [27]. The Mecklenburgh model, however, does not capture any rib cage motion nor respiratory muscle effects on the thoracic and the abdominal cavities.

A common way to include rib cage mechanical characteristics into a lung model has been to adopt a lumped chest wall compliance (C_{cw}). See [58][25] as examples. C_{cw} is a single parameter, lumping both abdominal and rib cage compliances, that describes the elasticity of the entire chest wall. Conditions such as obesity, ascites, and neuromuscular weakness can cause alterations in the respiratory system compliances, and lead to respiration inefficiency [59]. These diseases are then modeled by changing C_{cw}. However, since C_{cw} lumps the effects of both abdominal cavity and rib cage, it is hard to discern between conditions affecting one and not the other, like ascites, which primarily affects the abdomen.

Ward *et al.*, Kenyon *et al.* and Wilson *et al.* [60]–[62] published rib cage models that comprehensively describe the rib cage mechanics, including 1) the pleural cavity and the abdominal cavity, 2) a rib cage (thoracic cavity) that is separated into two parts: the lung-apposed rib cage and the abdomen-apposed rib cage, and 3) the diaphragm insertional and appositional effects on rib cage. However, some breathing mechanisms were simplified or missing based on the respiratory physiology: 1) all the hydraulic pressure-volume relations of the chest wall compartments are simplified as mechanical spring systems, 2) the rib rotation (bucket handle mechanism) during normal breathing is not included, 3) the effect of the respiratory muscle contraction force on the rib cage is simplified as a negative pressure source.

Using springs to model the pressure-volume relations of human breathing [60]–[62] is a good step to understand the breathing mechanism, however, in this work, we follow the anatomy and the physiology of the chest wall and include energy storage and dissipation elements in both mechanical and hydraulic domains to sufficiently capture human breathing behavior. We model the rib cage as a mechanohydraulic system from the contraction of the respiratory muscles, and we derive the chest wall volume from the angular displacements of the upper and lower ribs via a bucket handle mechanism. Lung air tubes that share similar geometric and functional properties are lumped into one compartment. The lungs are thus partitioned into four compartments: larynx, trachea, bronchi, and alveoli, like Rideout's work [1], [28]. However here, the proposed compartmental lung model has multiple energy domains: translational mechanical, rotational mechanical, and hydraulic domains. Direct measurements of muscle tension force are invasive [18] and hence not found in the literature. However, we assessed the muscle tension force using three invasively measured signals: 1) diaphragmatic central tendon displacement (d_{ct}) [54], 2) abdominal cavity pressure (P_{abd}) [55], and 3) pleural cavity pressure (P_{pl}) [1]. We utilize these

three invasively measured signals only once to compute the respiratory forces during breathing, and then use these forces as inputs to perform simulation studies.

Figure 2.4 shows the human respiratory system in a 2-D anatomical diagram. The thoracic cavity (grey) and the abdominal cavity (white) are anatomically separated by the central tendon of the diaphragm. The diaphragm is presented as the central tendon (CT) and the diaphragm muscles at the zone of apposition (ZOA). The pleural cavity enveloping the lungs plays a critical role in respiration, as it affects the alveolar pressure, determining inhalation and exhalation. The pleural cavity pressure thus serves as the connection point that links the RMRM and the LM modules. In this model, we consider the rib cage as two separate compartments, the upper rib cage (URC) and the lower rib cage (URC). In healthy conditions, the movements of URC and LRC are similar, however, De Troyer [63], [64] found that in both dogs and humans, the upper ribs move paradoxically inward during inspiration whereas the lower ribs move outward when only the diaphragm is active. In quadriplegic patients with phrenic paced diaphragm, who suffer from intercostal muscle paralysis, the URC and the LRC move differently [56], [65], [66]. This observation shows that the rib cage does not act as a single unit. Thus, we include two angular velocity nodes to model the human rib cage. The rotation of ribs (*i.e.* the expansion of the rib cage) and the descending of diaphragmatic dome alter the pleural cavity volume and change the pleural cavity pressure. The LRC is separated by the diaphragm as the pleura-apposed and abdomen-apposed parts. In Figure 2.4, colors represent different energy domains. The green nodes represent hydraulic pressures of the different compartments in the chest wall, the purple nodes are the angular velocities of the ribs and the blue node is the translational velocity of the diaphragmatic central tendon during respiration.

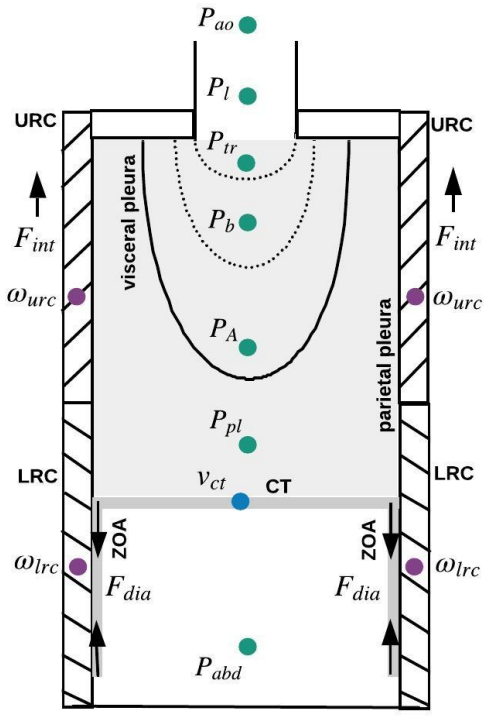

Figure 2. 4: 2-D anatomical diagram showing the human respiratory system and the important nodes to model. URC: upper rib cage; LRC: lower rib cage; ZOA: zone of apposition; CT: central tendon; F: force; P: pressure; ω: angular velocity; v: velocity; pl: pleural cavity; abd: abdomen; A: alveoli; b: bronchi; tr: trachea; l: larynx; ao: airway opening.

2.2.2 Model Development

Figure 2.5 shows a linear graph of the LM and RMRM modules. We employ this technique to aid in the development of our dynamic model. A linear graph is a visual tool that can concisely display all dynamic interactions of a complex system, hence aiding to systematically formulate the dynamic equations of the system [7].

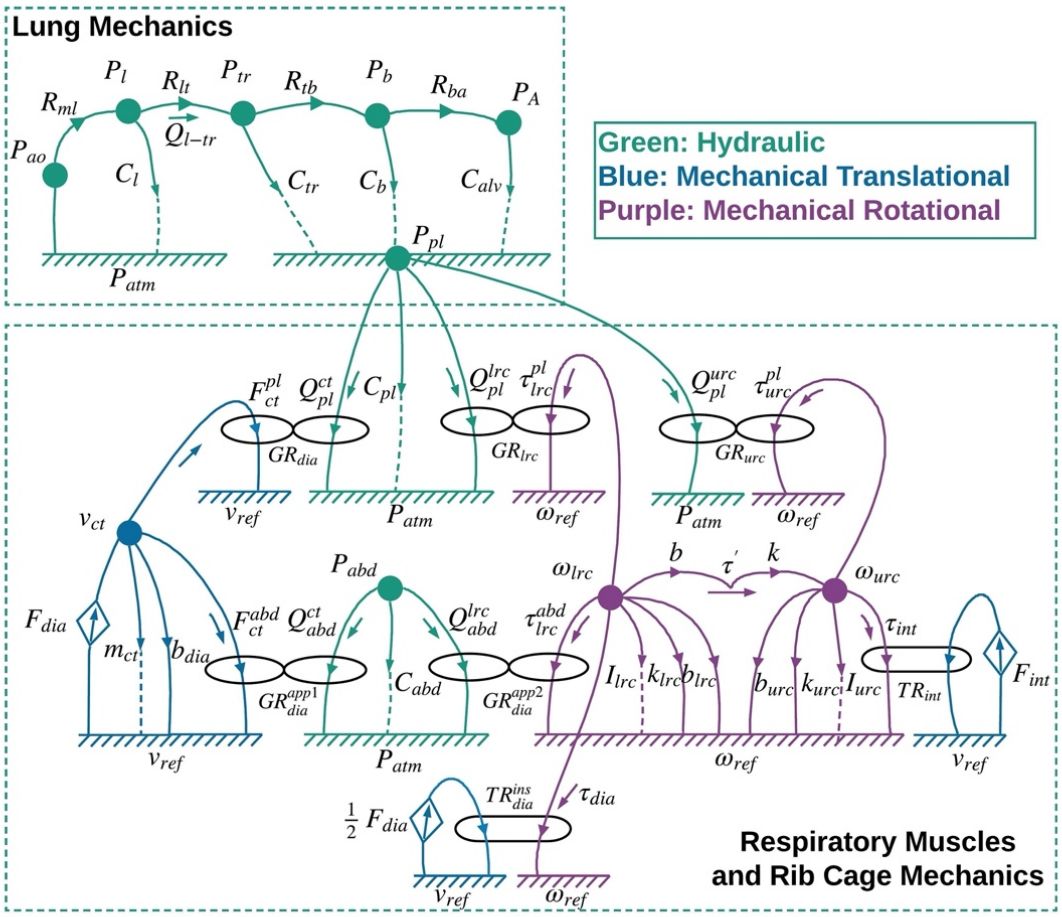

Figure 2. 5: Linear graph of the lung mechanics and the respiratory muscles and rib cage mechanics modules. P: pressure; v: velocity; ω: angular velocity; F: force; Q: flow; τ: torque; C: hydraulic capacitance; R: hydraulic resistance; b: friction (damper effect); k: spring effect; m: mass; I: moment of inertia; ct: central tendon; dia: diaphragm; abd: abdomen; lrc: lower rib cage; urc: upper rib cage; int: intercostal muscles; pl: pleural cavity; ao: airway opening; l: layrnx; tr: trachea; b: bronchi; a: alveoli; ml: mouth to layrnx; lt: laryx to trachea; tb: trachea to bronchi; ba: bronchi to alveoli; ref: reference; atm: atmosphere; GR: gyration ratio; TR: transformation ratio.

In Figure 2.5, we adopted three colors to represent the three aforementioned energy domains (translational mechanical, rotational mechanical, and hydraulic). The inputs of the proposed model are considered to be the contraction forces of the diaphragm and the intercostal muscles (F_{dia}, F_{int}), denoted by the diamond shape in the linear graph.

In the linear graph, every node (filled circle) represents a spatial compartment and is labeled with a variable, more specifically an across-variable, *i.e.*, pressure, velocity, and angular velocity (quantities that could potentially be measured across two terminals, one of which is considered reference). Every line with an arrow represents a through-variable that could potentially be measured, *i.e.*, flow, force, or torque. A line (hence linear graph), in which the through-variable flows, is either labeled with a parameter (a resistance, a capacitance, etc.), or is linked to an energy transducer element. Two types of energy-transducing elements are shown in Figure 2.5, transformers (ring shape) and gyrators (cross-linked ring shape). We assume ideal energy transduction and hence the transducers are lossless power devices and are represented by algebraic equations. Each transducer is labeled by either a gyration ratio (*GR*) or a transformation ratio (*TR*). Across- and through-variables are then used in continuity and compatibility relations to derive the differential equations of the dynamic system. In Figure 2.5, the diaphragm muscles displace the LRC via the appositional and the insertional gyrators (GR_{dia}^{app1}, GR_{dia}^{app2}, and GR_{dia}^{ins}). The intercostal muscles displace the URC via a transformer (TR_{int}). The rotation of the upper ribs and lower ribs change P_{pl} via two gyrators (GR_{urc} and GR_{lrc}).

Both the LRC and the URC have stiffness and damping characteristics. Hence, we assigned energy dissipation, potential and kinetic energy storage elements (b, k and I) for each compartment. The LRC and the URC are anatomically connected, and hence we modeled this coupling via a stiffness and a damping element in series. The LRC and URC individual mechanical behaviors are modeled via parallel arrangement of the energy dissipation (damper parameter) and the potential energy storage elements (stiffness parameter). However, their coupling is modeled via a series arrangement, as seen in Figure 2.5.

From the linear graph, we derived the dynamic equations at each node. The equations in the hydraulic domain are derived following the laws of conservation of mass. For example, to solve for the pleural cavity pressure, we derive the following:

$$C_{pl}\dot{P}_{pl} = Q_{l-tr} - Q_{pl}^{ct} - Q_{Pl}^{lrc} - Q_{pl}^{urc} \tag{2.1}$$

where Q_{pl}^{ct}, Q_{Pl}^{lrc}, Q_{pl}^{urc} are the entrained flows generated by the respiratory motion of the diaphragmatic central tendon, the lower rib cage, and the upper rib cage, respectively. C_{pl} is the hydraulic capacitance of the pleural cavity, P_{pl} is the hydraulic pressure of the pleural cavity, and Q_{l-tr} is the fluid flow from larynx to trachea. For instance, the entrained flow Q_{pl}^{ct} can be solved for via a transducer equation:

$$\begin{bmatrix} v_{ct} \\ F_{ct}^{pl} \end{bmatrix} = \begin{bmatrix} 0 & \frac{1}{A_{do}} \\ -A_{do} & 0 \end{bmatrix} \begin{bmatrix} P_{Pl} \\ Q_{pl}^{ct} \end{bmatrix} \tag{2.2}$$

A_{do} is the surface area of the diaphragm dome and is also the gyration ratio, the parameter that characterizes energy transduction from the translational mechanical domain to the hydraulic domain. v_{ct} is the velocity of the central tendon, and F_{ct}^{pl} is the force applied on the pleural cavity from the diaphragmatic central tendon. Using Equation 2.1 and substituting the other two entrained flow terms (Equation 2.10 and 2.11 in Appendix), we have

$$C_{pl}\dot{P}_{pl} = Q_{l-tr} - A_{do}v_{ct} - A_{urc}l_{rb}^{u}\sin\left(\theta_{u,o} - \theta_{u}\right)\omega_{urc} - A_{lrc}^{pl}l_{rb}^{l}\sin\left(\theta_{l,o} - \theta_{l}\right)\omega_{lrc} \tag{2.3}$$

where A_{urc} and A_{lrc}^{pl} are the surface areas of the upper and lower rib cage that are apposed to the pleural cavity. l_{rb}^{u} and l_{rb}^{l} are the average rib length of the upper and the lower rib cage, $\theta_{u,o}$ and $\theta_{l,o}$ are the initial angles between the ribs on the coronal plane and the horizontal line of the URC and the LRC, θ_u and θ_l are the angular displacement of the URC and the LRC during respiration,

ω_{urc} and ω_{lrc} are the angular velocity of the URC and the LRC during respiration, and the rest variables are the same as shown in the earlier equations.

The dynamic equation of the velocity of the central tendon is derived according to Newton's Second Law of motion, as shown in the following:

$$m_{ct}\dot{v}_{ct} = F_{dia} - F_{ct}^{abd} - F_{ct}^{pl} - b_{dia}v_{ct} \tag{2.4}$$

where F_{ct}^{abd} and F_{ct}^{pl} are the resultant forces applied on the abdominal cavity and the pleural cavity due to the movement of the diaphragmatic central tendon, m_{ct} is the mass of diaphragmatic central tendon, F_{dia} is the diaphragm contraction force, b_{dia} is the friction of the diaphragm, and the other variables are the same as shown in the earlier equations. These forces are computed via gyration relations. The equations of the entire system can be found in the Appendix.

2.2.3 Parameter Assignment

Table 2.1 shows the model parameters of the chest wall compartments, *i.e.*, the diaphragm muscles, the rib cage and intercostal muscles, and the abdominal and pleural cavities, that are either measured or computed based on human studies as described in the following sections.

Table 2. 1: Model Parameter Values

Parameter	Value	Reference
Diaphragm Muscles		
$\boldsymbol{m_{ct}}$ (kg)	19.81e-3	[67]
$\boldsymbol{A_{do}}$ (m^2)	4.9E-2	[68]
$\boldsymbol{b_{dia}}$ (N/m·s)	3.9E-1	-
Rib Cage and Intercostal Muscles		
$\boldsymbol{A_{urc}}$ (m^2)	1.115E-1	[69]
$\boldsymbol{A_{lrc}}$ (m^2)	1.115E-1	[69]
$\boldsymbol{A_{zoa,o}}$ (m^2)	8.92E-2	[70]
$\boldsymbol{\theta_{l,o}}$ (radians)	0.72	-
$\boldsymbol{\theta_{u,o}}$ (radians)	0.57	-
$\boldsymbol{l_{rb}^{u}}$ (m)	1.76E-1	[71]
$\boldsymbol{l_{rb}^{l}}$ (m)	1.98E-1	[71]
$\boldsymbol{I_{lrc}}$ ($kg \cdot m^2$)	1.77E-2	-
$\boldsymbol{I_{urc}}$($kg \cdot m^2$)	1.17E-2	-
$\boldsymbol{m_{urc}}$ (kg)	0.752	[72]
$\boldsymbol{m_{lrc}}$ (kg)	0.903	[72]
$\boldsymbol{b_{urc}}$ (N/cm·s)	0.23	-
$\boldsymbol{b_{lrc}}$ (N/m·s)	0.35	-
$\boldsymbol{b}$ (N/m·s)	7870.5	App. Eqn (A-23)
$\boldsymbol{k_{urc}}$ (N/m)	30	-
$\boldsymbol{k_{lrc}}$ (N/m)	50	-
$\boldsymbol{k}$ (N/m)	57.15	App. Eqn (A-23)
Abdominal and Pleural Cavities		
$\boldsymbol{C_{abd}}$ (m^5/N)	2.07E-6	[73]
$\boldsymbol{C_{pl}}$ (m^5/N)	2.08E-6	[74]–[76]

2.2.3.1 Diaphragm Muscles

This section introduces the parameters that are used in the Appendix Equations 2.1-2.3 that relate to the diaphragm muscles. The diaphragm consists of the diaphragmatic central tendon and the diaphragm muscles. The mass of the central tendon (m_{ct}) serves as the kinetic energy storage element as the diaphragm muscles contract. Arora et al. [67] measured the weight and the surface

area of the diaphragm muscles of 27 normal patients (average weight of 68 kg and average age of 46 years). The average weight of the whole diaphragm was measured as 283 ± 53 g, and the mass of the muscular portion is measured to be 93 ± 2% of the total [67]. The mass of the central tendon was derived as $m_{ct} = (1 - 93\%) \times 283 = 19.81$ g. Cassart et al. [68] reported the surface area of the diaphragm dome (A_{do}) as 490 ± 22 cm^2 at functional residual capacity (FRC) for healthy patients. The friction of the diaphragm muscles during contraction is b_{dia}. Though small, we have calculated it to be 0.39 N/m·s via exhaustive search that minimizes the error between the simulated d_{ct} to the real human d_{ct} [54].

2.2.3.2 Rib Cage and Intercostal Muscles

From geometry (triangle formed by the respiratory muscle force, the ribs, and the horizontal line), we found that the products of the rib length, the rib cage surface area and the sine function of the angular displacement (*i.e.,* $l_{rb}^{u} A_{urc} \sin(\theta_{u,o} - \theta_u)$ and $l_{rb}^{l} A_{lrc} \sin(\theta_{l,o} - \theta_l)$) are the transducer ratios that relate the rotation of the ribs to the pressure of the pleural cavity. See Appendix Equations 2.10 and 2.11 for details.

To compute the surface area of the rib cage, we adopted the measurement of the surface area of the ZOA at rest, ($A_{zoa,0}$ = 892 cm^2) as reported by Pettiaux *et al.* [70], and the estimation by Troyer and Wilson [69] that A_{zoa} at rest is 40% of the total surface of the rib cage (A_{rc}). The total rib cage area was computed as $A_{rc} = A_{zoa}/0.4 = 2230$ cm^2. The entire rib cage is dichotomized into 1) the upper rib cage (1st to 5th pairs of ribs) that are apposed to the lungs, and 2) the lower rib cage that has partial surface (6th pair of the ribs) apposed to the pleura (A_{lrc}^{pl}) and partial surface (7th to 10th pairs of ribs) apposed to the abdominal cavity (A_{lrc}^{zoa}), known as zone of apposition. Thus, we have both A_{lrc} and A_{urc} computed as 1115 cm^2, where A_{lrc} is made of A_{lrc}^{pl} and A_{lrc}^{zoa} with values of 223 cm^2 and 892 cm^2, respectively.

To compute the angles between the rib projection of the coronal plane and the horizontal line of the URC ($\Theta_{u,o}$) and LRC ($\Theta_{l,o}$), we derive the following from geometry (triangle formed by the ribs, the horizontal line and the vertical line) $\Theta_{i,o} = \tan^{-1}\left(\left(\sqrt{(\frac{l_{tr}}{2}^2 + \frac{w_{tr}}{2}^2)} * \tan(\theta^i_{bkt}) + \frac{l^i_{chord}}{2} * \sin(\theta^i_{pump})\right)/l_{tr}\right)$, where i represents the rib cage compartment (URC or LRC), l_{tr} and w_{tr} are the length and width of the human thorax on the transverse plane, l^i_{chord} is the average rib chord length, θ^i_{bkt} and θ^i_{pump} are the average bucket handle angle (caused by intercostal muscle contraction) and the average pump handle angle (caused by accessary muscle contraction during forced inspiration. The values of l^u_{chord}, l^l_{chord}, l_{tr}, w_{tr}, θ^i_{bkt} and θ^i_{pump} are measured by Dansereau *et al.* [71]. Thus, we compute $\Theta_{u,o}$ and $\Theta_{l,o}$ as 0.57 and 0.72 radians, respectively.

To compute the rib length (l^i_{rb}) in Appendix Equations 2.10 and 2.11, we derive l^i_{rb} as $\frac{l_{tr}}{2}/\cos(\theta_{i,o})$. The values of l^u_{rb} and l^l_{rb} are 17.6 cm and 19.8 cm respectively.

The GR^{app2}_{dia} gyrator (Appendix Equation 2.9) that relates Q^{lrc}_{abd} and ω_{lrc} as a product of l^l_{rb}, A_{zoa}, and $sin\,(\theta_{l,o} - \theta_l)$ is shown in the upper panel of Figure 2.6. Both A_{zoa} and θ_l change during respiration, which makes the GR^{app2}_{dia} a time-varying gyrator. We hence expect to see hysteresis in this relation, as it indeed shows in Figure 2.6, since both A_{zoa} and θ_l are time-varying parameters. Similarly, the plot of GR_{lrc} gyrator (Appendix Equation 2.11), that relates Q^{lrc}_{pl} and ω_{lrc} as the product of l^l_{rb}, A^{pl}_{lrc}, and $sin\left(\theta_{l,o} - \theta_l\right)$, is shown in the lower panel of Figure 2.6. Since we observe that both gyrator functions have negligible hysteresis behavior in Figure 2.6 and adopting linear slopes maintains the system linearity, which is advantageous in future system identification work, we approximate the gyration ratio as a constant, *i.e.*, the slope of the curve.

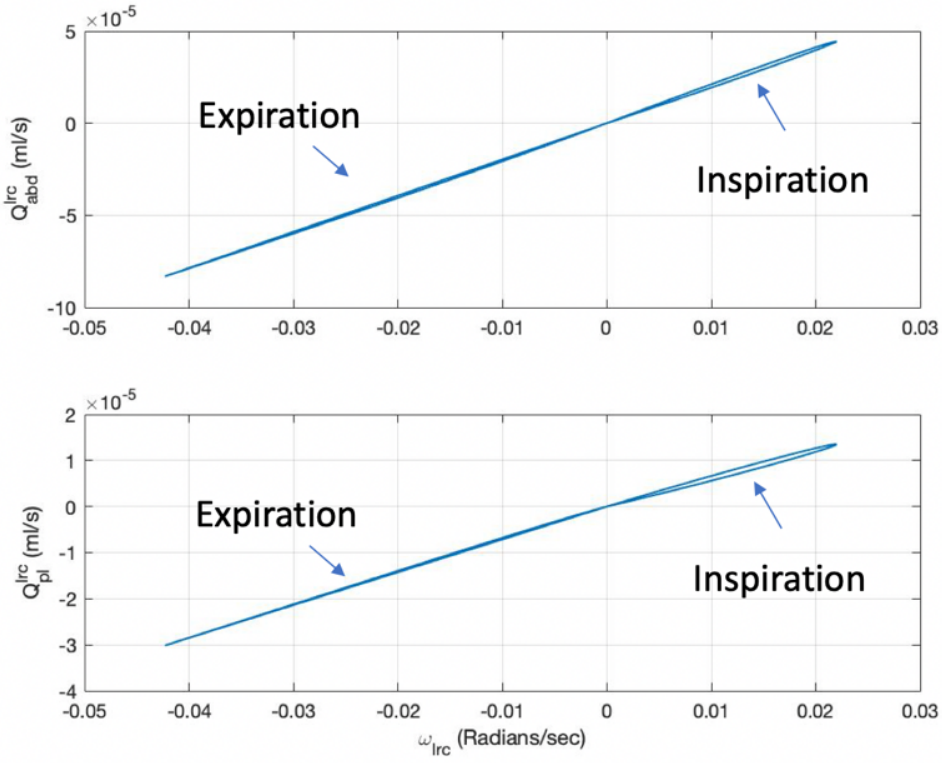

Figure 2. 6: Angular velocity of the LRC vs the entrained flow Q_{abd}^{lrc} and angular velocity of the URC vs the entrained flow Q_{abd}^{urc}.

In Appendix Equation 2.4 and 2.5, the kinetic energy storage in LRC and URC during respiration, *i.e.,* the moment of inertia (I_{urc} and I_{lrc}) is derived as $I_i = m_i \times \frac{{l_{rb}^i}^2}{2}$, where i represents the rib cage compartment (URC or LRC). To compute the masses of the rib cage (the masses of the intercostal muscles and the ribs), we take the density of the skeletal muscle as 1.06 kg/L [72], the thickness of the ribs as 0.7 cm [77], and assuming the same density of the ribs and the density of the intercostal muscles, the rib cage mass is computed as $m_{rc} = A_{rc} \times d_{rib} \times \rho = 1.65\ kg$. The masses of the upper and the lower rib cage (m_{urc} and m_{lrc}) are taken as 0.75 kg and 0.9 kg respectively. Taking the lengths computed earlier ($\Theta_{i,o}$ Equation) and the newly computed masses, we computed the moment of inertias (I_{urc} and I_{lrc}) as 117 kg·cm^2 and 177 kg·cm^2, respectively.

In Appendix Equation 2.4 and 2.5, the stiffness and damping effects of the LRC and URC, *i.e.*, k_{lrc}, b_{lrc} , k_{urc}, and b_{urc}, were tuned so that 1) the healthy simulation of ω_{urc} matches the human data, and 2) ω_{urc} simulation stays in a reasonable range. Note that these parameters are fixed after one-time tuning, and simulation subsequently will be run with the fixed set of these parameters.

The potential energy storage element k, and the energy dissipation element b at the connection between the LRC and the URC are not available from literature search. We estimate these two values via the least squares approach using the model Appendix Equation 2.6 with the measured $\omega_{urc}, \omega_{lrc}$ data and τ waveform computed from Appendix Equation 2.4. The values of k and b are estimated by minimizing the sum squared error of $\dot{\tau}$ and $k\left(\omega_{lrc} - \omega_{urc} - \frac{1}{b}\tau'\right)$, which are the left and the right side of the Appendix Equation 2.6, respectively.

2.2.2.4 Abdominal and Pleural Cavities:

In the Appendix Equation 2.2 and 2.3, the compliances of the abdominal and pleural cavities serve as potential energy storage elements.

The abdominal compliance is a measure of the ease of abdominal expansion, determined by the elasticity of the abdominal wall and the diaphragm. Malbrain *et al.* [73] reported a normal C_{abd} to be from 250 to 450 ml/mmHg. In this model, a C_{abd} value of 276 ml/mmHg was selected, since this value offers a good estimation of ω_{lrc} (Appendix Equation 2.2), *i.e.*, the computed ω_{lrc} has the same order of magnitude as ω_{urc} [78], but slightly bigger. We expect ω_{lrc} to be bigger than ω_{urc}, since the diaphragm muscles have stronger effect (appositional and insertional effects) on the angular displacement of the rib cage than the intercostal muscles during quiet breathing.

The compliance (inverse of elastance) of the pleural cavity is a measure of the ease of pleural cavity expansion. Heidecker *et al.* [74] measured normal pleural cavity compliance values from

124 patients, and they defined the normal range of pleural compliance to be 0.0689–2 L/cmH_2O. We used a C_{pl} value of 0.2 L/cmH_2O, since the ω_{urc} simulated for healthy patient matches well the human data (ω_{urc}) as measured by Wilson [78].

In the proposed model, we have 10 dynamic equations (6 equations in RMRM module and 4 equations in LM module), 30 parameters (22 parameters in RMRM module and 8 parameters in LM module), and 10 unknowns (9 nodes shown in Figure 2.4 and 1 torque between LRC and URC). The LM variables (pressures and volumes at different lung compartments) of healthy and diseased conditions (*e.g.*, respiratory muscle paralysis) can be now be simulated as the diaphragm and the intercostal muscles contract and relax.

2.3 Results

In order to simulate and produce results, we have first derived the two unknown inputs, *i.e.*, the contraction forces of the diaphragm and the intercostal muscles, from real patient data (three invasively measured signals from literature [54][55][1]). We have validated the computed force inputs with the unitless muscle force (shape-verification) proposed by Wilson's [62]. Secondly, we compared the force inputs to the published P_{mus} waveform [1] after converting the force inputs into the respiratory muscle pressure. Thirdly, we simulated the breathing mechanism using these two computed inputs in a healthy state, and validated the model outputs against healthy patient data [78]. A sensitivity analysis was also performed in order to find the effects of the model parameters on the model variables. Finally, we have validated our model with human data from quadriplegic patients [56].

2.3.1 Respiratory Muscle Forces Validation

The inputs of the proposed lung model (F_{dia} and F_{int}) were unavailable in the literature based on our extensive literature review, except a unitless force muscle force waveform that indicates the shape of the force during respiration [62]. Goldman [79] also claimed that in intact humans, clinicians generally do not measure lengths and tensions; rather they typically measure volumes and pressures. Therefore, to perform breathing simulation and to present the force waveforms of the diaphragm and the intercostal muscles during quiet breathing, we solve for F_{dia} and F_{int} algebraically from three invasively measured signals P_{pl} , P_{abd} and the central tendon displacement (d_{ct}) [54][55][1], using the dynamic Equations [2.1-2.5] in the Appendix. Note that once they have been computed, the forces are subsequently used without further computation or tuning. The measurements of P_{pl}, P_{abd} and d_{ct} of a healthy human during quiet breathing were reproduced in red in Figure 2.7. Adopting the parameters in Table 1 and the human P_{pl}, P_{abd} and d_{ct} signals, we computed the respiratory muscle forces as shown in Figure 2.8. The diaphragm muscles play a vital role in sustaining ventilation and are considered essential for respiration [80], [81]. We would expect the computed contraction force of diaphragm to be greater than that of the intercostal muscles, as indeed indicated in Figure 2.8 where F_{dia} generates around 27.4 N while F_{int} generates only about 10 N. Wilson [62] reported dimensionless respiratory muscle force that was scaled from 0 to 1 showing the force waveform over a breath. After descaling them into the magnitude of the computed forces ($F_{dia}$and F_{int}), shown in black in Figure 2.8, both forces have shapes that match Wilson's [62]. In addition, the shapes of both forces also follow the shape of the P_{mus} waveform, which has a finite rate of rise, a rounded peak, and a rapid fall [57][82]. This gives further credence to our computed respiratory muscles forces. Pressure and force waveforms should share the same shape because they are directly related by a constant factor (surface area).

2.3.2 Simulation and Validation for Healthy Subjects

Using the computed F_{dia} and F_{int} as the inputs of the system, we simulate the model and validate the model outputs with the real patient data. The simulated P_{pl}, P_{abd} and d_{ct} closely match the real patient data as shown in Figure 2.7. The upper panel shows that the simulated pleural cavity pressure decreases from -5 cmH_2O to -8 cmH_2O during quiet breathing, matching to a validated human P_{pl} waveform from an accepted lung model (red) [1], which has been validated with an average human profile proposed by Mecklenburgh and Mapleson [57]. The middle panel shows the simulated abdominal cavity pressure changing from 6.9 to 9.7 cmH_2O, with a magnitude of 2.8 cmH_2O. This magnitude matches the human data reported by Mills *et al.* [55] as shown in Figure 2.7 middle panel. The lower panel shows the simulated central tendon displacement movement of 1.34 cm during quiet breathing, which also matches the human measurements from Ayoub *et al.*

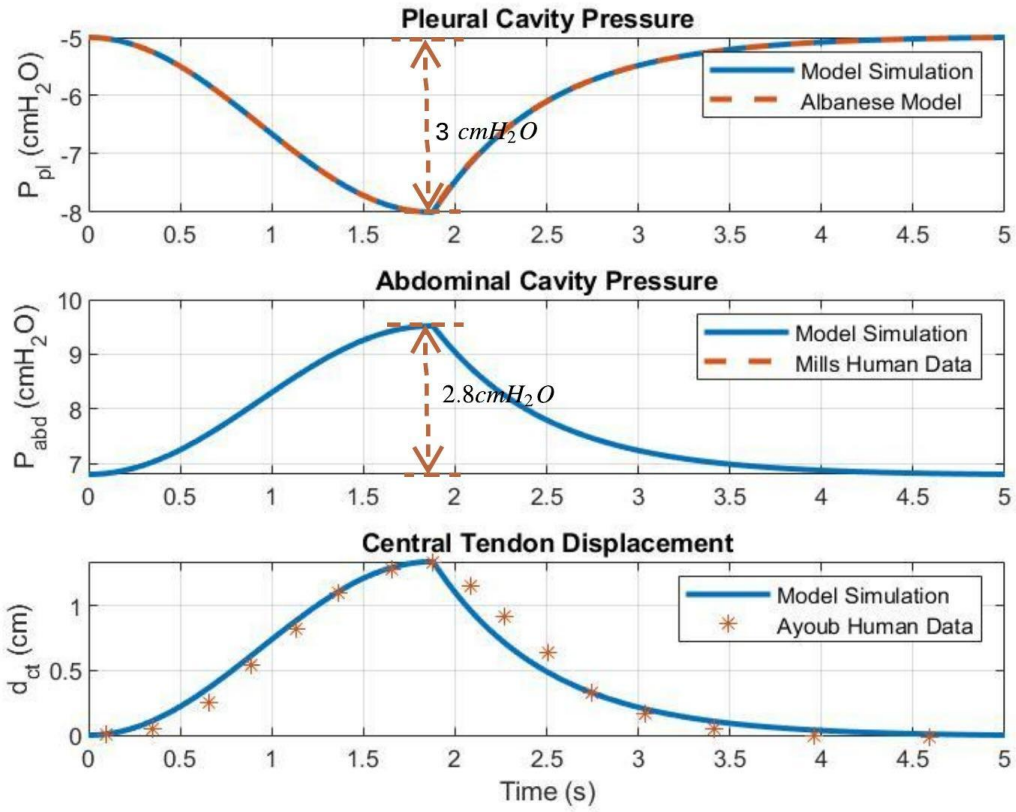

Figure 2. 7: Pleural cavity pressure, abdominal cavity pressure, and diaphragmatic central tendon displacement simulation and validation for healthy human during quiet breathing. The upper panel shows the simulated pleural cavity pressure in one breath (blue), and its validation against an validated model from Albanese [1]. The middle panel shows the simulated abdominal cavity simulation (blue), and its validation against one healthy human data from Mills [55]. The lower panel shows the diaphragmatic central tendon displacement simulation (blue), and its validation with one healthy human data from Ayoub [54].

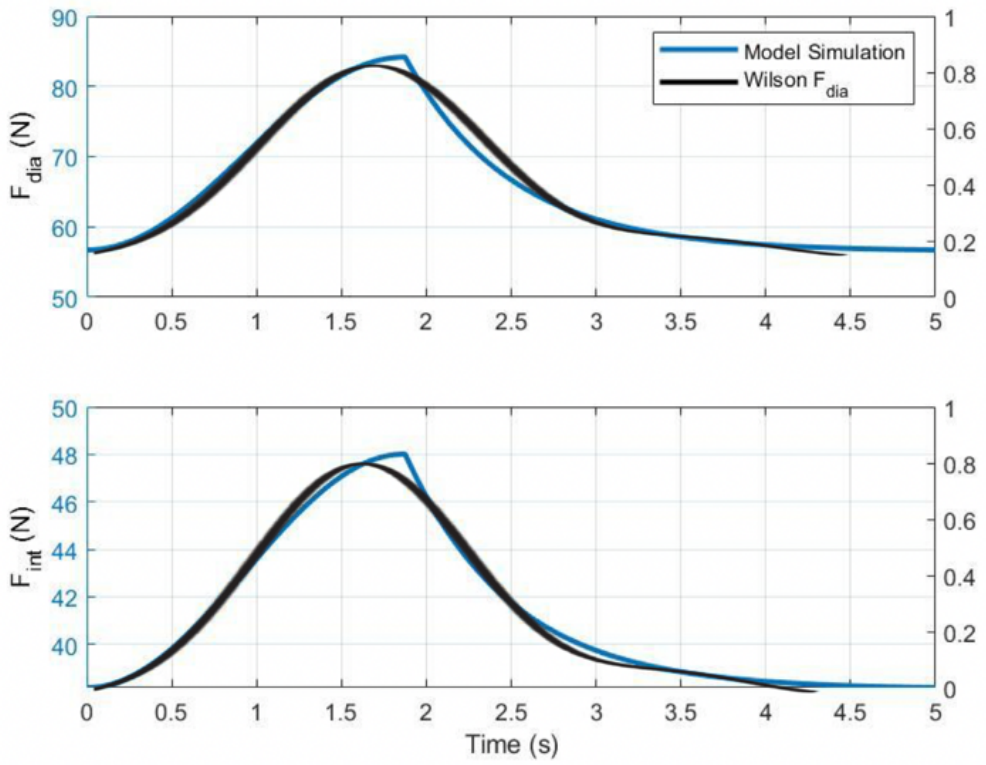

Figure 2. 8: Contraction forces of the diaphragm and the intercostal muscles during quiet breathing. The blue curves are the computed forces and the black are the unitless force reported by Wilson [62].

Though the angular rotation of the rib cage may not be a critical clinical variable to measure, it is nonetheless a state in our dynamic system, and hence we need to account for it to complete the picture of rib cage dynamics. Figure 2.9 shows the simulated angular displacements of the LRC and the URC. The measurement of human rib angular displacement during quiet breathing is unavailable from our literature review, however, we found a few recorded static values. Wilson reported a URC angular displacement of 11.1° from FRC to total lung capacity (TLC) [78]. Cassart [68] reported that the surface area of the human ZOA changes linearly from FRC to TLC. We thus apply the same assumption (linear rib rotation from FRC to TLC) to Wilson's study [78], and the study shows a human upper ribs rotation of 1.54° (0.026 rad) during quiet breathing. In Figure 2.9, the simulation shows that the URC rotates about 0.026 radians (1.54°) and the LRC rotates about 0.037 radians (2.1°). The simulated URC angular displacement matches to the reference data from

Wilson [78], and the LRC has a greater angular displacement as compared to the URC from our simulation. This is expected since the respiratory muscles, especially the diaphragm muscles (the appositional and the insertional effects), have stronger effect on the angular displacement of the LRC, while the movement of the URC is only controlled by the intercostal muscles during quiet breathing.

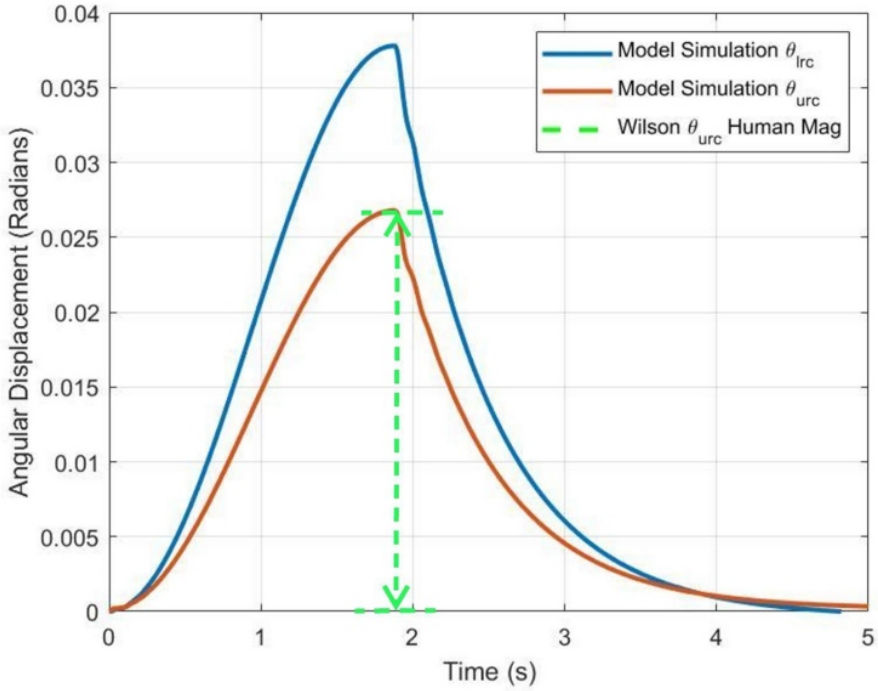

Figure 2. 9: Simulation and validation of the angular displacement of the LRC and the URC. The blue and red curves are the simulation results of the LRC and the URC, respectively. The green dashed line shows the magnitude of the URC angular displacement reported by Wilson [78].

The P_{mus} is a "lumped pressure" used to describe the collective respiratory muscle and is estimated to have a magnitude of about 4.5-5.5 cmH_2O during quiet breathing [9],[27],[39]. To compare the computed F_{dia} and F_{int} in the proposed model to the P_{mus} waveform from an accepted model [9], we have derived the muscle pressure due to the force applied to the rib cage and diaphragmatic central tendon. This muscle pressure is derived from the diaphragm force

applied to the diaphragmatic central tendon and the lower ribs ($\frac{F_{dia}^{dir}}{A_{do}} + \frac{F_{dia}^{inser}}{A_{lrc}} + \frac{F_{dia}^{appo}}{A_{lrc}}$), and the intercostal muscle force applied to the upper ribs ($\frac{F_{int}}{A_{urc}}$). Figure 2.10 shows the muscular pressure waveform from our computed muscle forces (blue) and the P_{mus} waveform from an accepted model (red) [9]. The simulation results from Albanese *et al.* [1] are validated based on the average human profile proposed by Mecklenburgh and Mapleson [57]. The computed muscle pressure has a peak magnitude of 6 cmH_2O, and Albanese *et al.* [1] adopted a P_{mus} magnitude of 5 cmH_2O. This shows that our derived P_{mus} is within a reasonable range, as compared to a validated model [1]. Since P_{mus} is an approximation of respiratory muscle effort, our model's combined muscle pressure (derived from F_{dia} and F_{int}) may in fact be more accurate.

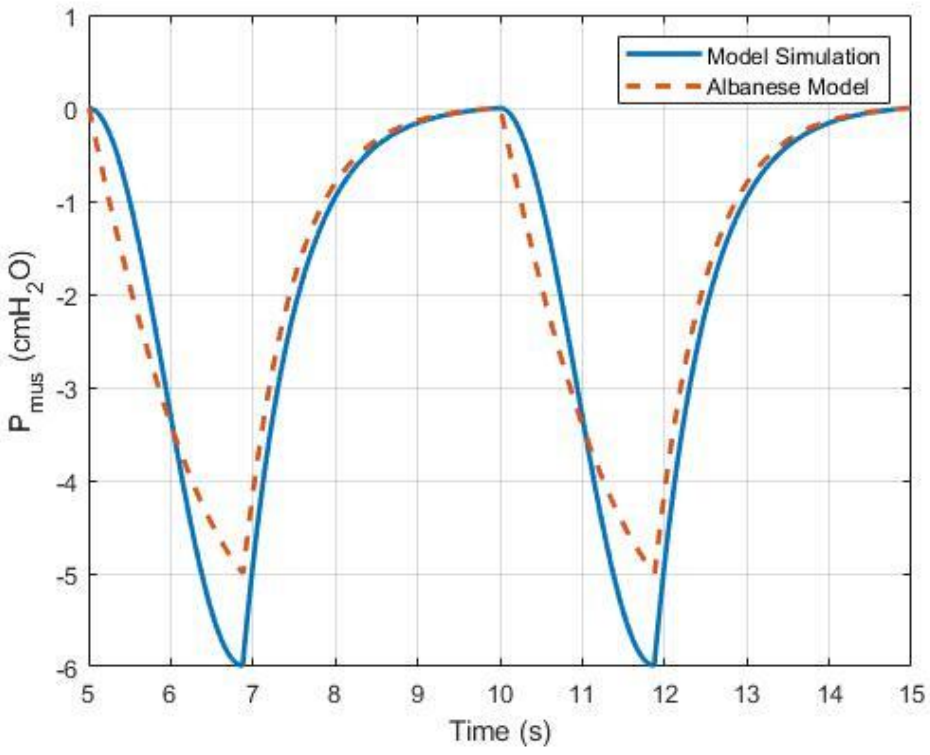

Figure 2. 10: Respiratory muscle pressure on the rib cage. The blue curve is from the model simulation, and the red curve is from an accepted model [1].

2.3.3 Sensitivity Analysis

We performed a model sensitivity analysis to quantify the effect of each model parameter on each variable. The sensitivity was evaluated via the sigma values (Σ) as shown in Table 2.2. The sigma value, computed as $\Sigma = \frac{\Delta Variable \times Parameter}{\Delta Parameter \times Variable}$, is a measure of the effect of the change in parameters on the resulting change in variables, where parameters represent material property and geometry of the system, while variables are the system outputs (or inputs) that could potentially be measured with sensors. A bigger Σ value indicates a higher sensitivity of a certain parameter to a certain variable. In Table 2.2, the sigma values were computed by changing the parameters from a 50% decrease to a 50% increase with an increment of 10%. Then, a mean sigma was generated for each parameter, reported in every cell in Table 2.2. Finally, mean sigma values for each parameter on all the variables were presented in the last column in Table 2.2 to determine which parameters are the most sensitive. The LM model variables, such as $P_A, V_A, Q, etc.$, are the most sensitive to A_{ct}, as A_{ct} directly determines the diaphragm muscle effect on P_{pl} and P_{abd}. Though, the surface area of the central tendon (or the diaphragmatic dome) (A_{ct}) may vary from person to person, it does not change up or down by 50% with disease. Therefore, A_{ct} is a sensitive parameter numerically but treated as a constant number in most disease conditions. The model variables are also sensitive to the two compliance values, C_{abd} and C_{pl}, which is expected since the compliance C_{abd} has a strong effect on abdominal pressure (Appendix Equation 2.2) and the diaphragmatic central tendon displacement during breathing (Appendix Equation 2.1). In addition, the compliance C_{pl} greatly affects the pleural cavity pressure (Appendix Equation 2.3), and thus all the pressures of different lung compartments. The model variables are less sensitive to other parameters (*e.g.* the rib length, initial rib angle, central tendon mass, and the muscle friction) compared to the compliance values. This is expected since the rib length, the initial rib angle and

the central tendon mass do not often change in adults, and they do not often cause respiratory diseases. Similarly, the change of muscle friction during muscle contraction is also negligible, since muscle friction does not often cause respiratory stress either.

Table 2.2: Sensitivity Results

Σ	P_A	V_A	V_L	Q	P_b	P_{tr}	P_l	P_{pl}	P_{abd}	θ_{urc}	θ_{lrc}	d_{ct}	Mean
C_{pl}	0.53	0.53	0.53	0.53	0.53	0.53	0.53	0.53	0.58	0.35	0.26	0.53	0.50
C_{abd}	0.38	0.38	0.38	0.38	0.38	0.38	0.38	0.38	0.42	0.25	0.19	0.47	0.36
A_{ct}	0.97	0.97	0.97	0.97	0.97	0.97	0.97	0.97	1.32	0.18	0.13	2.59	1.00
m_{ct}	0.00	0.00	0.00	0.01	0.00	0.00	0.00	0.00	0.00	0.00	0.04	0.01	0.01
l_{rb}^{u}	0.07	0.07	0.07	0.08	0.07	0.07	0.07	0.07	0.08	0.30	0.08	0.06	0.09
l_{rb}^{l}	0.09	0.09	0.09	0.09	0.09	0.09	0.09	0.09	0.10	0.47	0.66	0.02	0.17
α_{zoa}	0.10	0.10	0.10	0.10	0.10	0.10	0.10	0.10	0.11	0.12	0.21	0.10	0.11
α_{pl}	0.01	0.01	0.01	0.01	0.01	0.01	0.01	0.01	0.01	0.07	0.09	0.03	0.02
θ_{urc}^{ini}	0.01	0.01	0.01	0.02	0.01	0.01	0.01	0.01	0.01	0.60	0.20	0.03	0.08
θ_{lrc}^{ini}	0.06	0.06	0.06	0.06	0.06	0.06	0.06	0.06	0.06	0.30	0.42	0.02	0.10
b_{lrc}	0.00	0.00	0.00	0.01	0.00	0.00	0.00	0.00	0.00	0.00	0.04	0.01	0.01
b_{urc}	0.00	0.00	0.00	0.01	0.00	0.00	0.00	0.00	0.00	0.00	0.04	0.01	0.01
k_{lrc}	0.09	0.09	0.09	0.09	0.09	0.09	0.09	0.09	0.10	0.45	0.65	0.02	0.16
k	0.00	0.00	0.00	0.01	0.00	0.00	0.00	0.00	0.00	0.16	0.10	0.01	0.03
b	0.00	0.00	0.00	0.01	0.00	0.00	0.00	0.00	0.00	0.01	0.04	0.01	0.01
b_{ct}	0.00	0.00	0.00	0.01	0.00	0.00	0.00	0.00	0.00	0.00	0.04	0.01	0.01

2.3.4 Simulation and Validation for Quadriplegic Patients

To validate the proposed model in a diseased state, we leverage data from quadriplegic patients. Quadriplegic patients with injury of the cervical cord have respiratory paralysis that needs respiratory support. They rely on the electrical stimulation of the phrenic nerve so that the diaphragm gets activated to sustain respiration [65]. Phrenic pacing on the diaphragm alone allows us to examine breathing behavior so that we can better understand the breathing mechanism. Quadriplegic patients with isolated paced diaphragm have paradoxical URC and LRC movements, *i.e.*, the URC shrinks and the LRC expands during inspiration. Since the intercostal muscles are paralyzed, the negative P_{pl} effect dominates the motion of the URC and causes the URC to move inward as P_{pl} decreases during inspiration. In addition, due to the inactivity of the intercostal muscles, the rib cage loses the muscle control, thus tends to be more flexible. Therefore, the parameters of the URC and the LRC are directly affected, *i.e.* b_{lrc}, b_{urc}, b, k_{lrc}, k_{urc}, k. In order to prove that we could successfully simulate quadriplegic patients we have tuned the model parameters to fit the patient data. Note that we change and fix the parameters in order to simulate the breathing response of a quadriplegic patient. We reduced the rib cage stiffnesses and resistances from the basal values and increased abdominal compliance values. Specifically, and through an exhaustive search on the parameter values, we have replicated quadriplegic patient measurements by decreasing b_{lrc}, b_{urc} by 2 times, decreasing b by 20 times, decreasing k_{lrc}, k_{urc} by 1.8 times and 14 times respectively, and increasing C_{abd} by 2 times. In addition, as the phrenic nerve gets stimulated by electromagnetic waves, we have increased the diaphragm contraction force by 50% from the F_{dia} during quiet breathing. Figure 2.11 shows the angular displacements of the lower and the upper rib cage of quadriplegic patients. Our simulation replicates the quadriplegic patient data well, especially the angular displacement of the URC that decreases

during inspiration. Figure 2.12 shows the simulation of P_{pl}, P_{abd}, and P_{di} for quadriplegic patients, and the validation against human measurements in [56]. As shown in Figure 2.12, our simulation closely matches the real patient data with an average error of 7.69%.

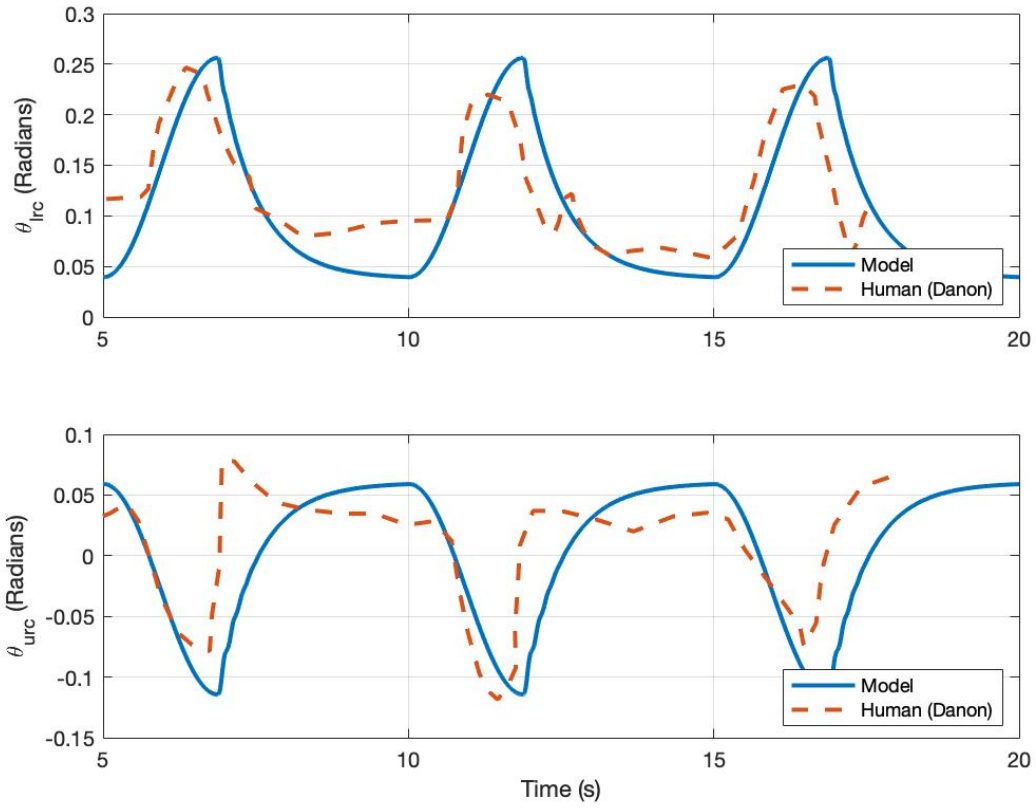

Figure 2. 11: Angular displacements of the lower and the upper rib cage. The blue curves are model simulation and the red dashed curves are real patient data from [56].

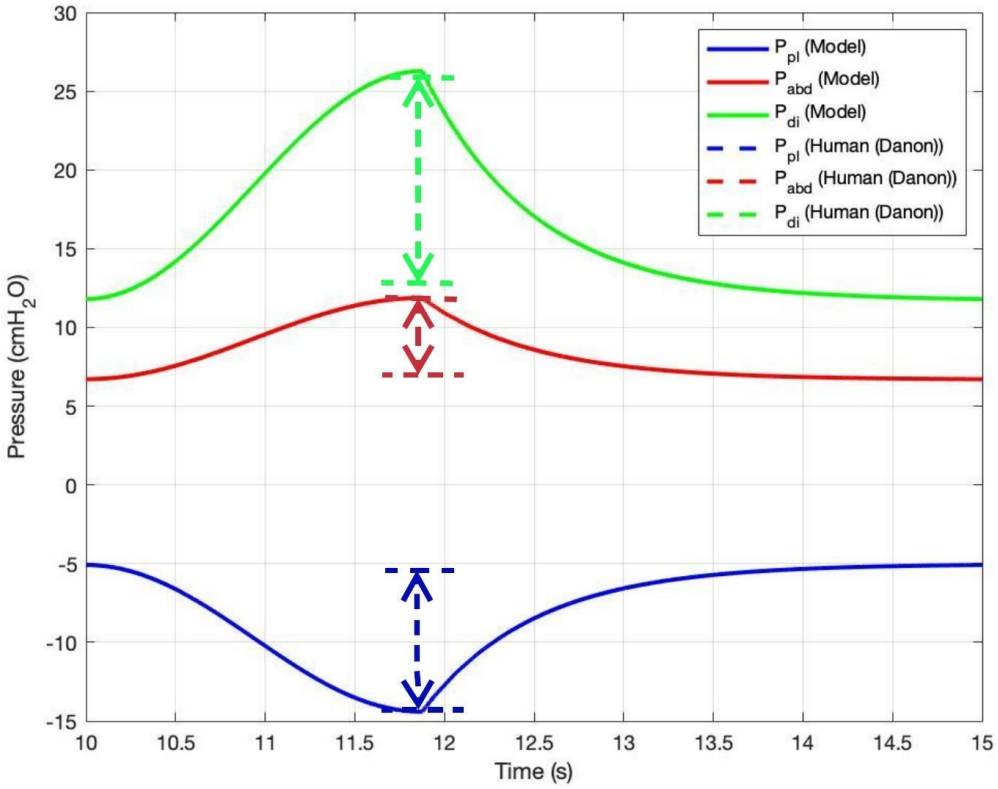

Figure 2. 12: Pleural cavity pressure (P_{pl}), abdominal cavity pressure (P_{abd}), and transdiaphramatic pressure (P_{di}) simulation, shown in blue, red, and green respectively. The pressure magnitudes are validated against [56], shown in dashed lines.

For quadriplegic patients, a drop in P_{pl} (9 $\mathrm{cmH_2O}$) is generated due to phrenic stimulation, which induces a bigger tidal volume into the lungs compared to the tidal volume during quiet breathing (a P_{pl} drop of 5 $\mathrm{cmH_2O}$). The lung mechanics variables: V_L, P_A, and Q_{air} were also simulated with this P_{pl}, as shown in Figure 2.13. The simulated lung volume reaches 4.1 liters, and the increase of the lung volume is 220% greater compared to the lung volume change during quiet breathing. Danon *et al.* reported that with a P_{di} of 13 $\mathrm{cmH_2O}$, the lung volume increased by about 2 liters from FRC, which agrees with our simulation (1.7L). The 0.3-liter offset is expected, since 1) the sample patient in the Danon's study may have lungs with different compliance values (greater C_{alv} than those in our simulation), 2) Danon's sample patient may have different lung size

compared to the model. Note that in the simulation of quadriplegic patients, we adopted lung parameters (compliances and resistances) for the healthy human from Rideout *et al.* [28], a different human study.

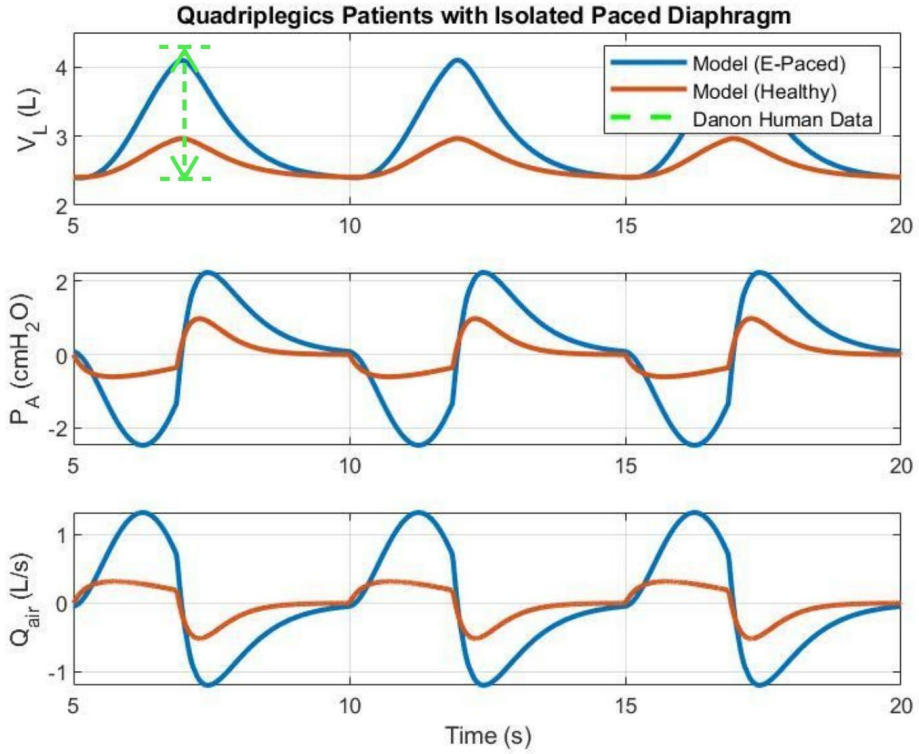

Figure 2. 13: Lung mechanics variables simulation for quadriplegic patients with isolated paced diaphragm (blue) and healthy state (red). The lung volume (V_L), alveolar pressure (P_A), and air flow (Q_{air}) are shown.

2.3.5 Model Stability and Robustness Assessment

Further, to check the stability of the proposed model, we formulate the dynamic system into a state-space form, and the state equation can be found in the Appendix Equation 2.5. We then computed the eigenvalues of the state matrix to study the stability of the system. The eigenvalues all have negative real parts, *i.e.* $-9.99 \pm 272.83i, -10.49 \pm 53.78i,$ and $-4.99 \pm 20.33i,$ indicating stability of the linearized model. For numerical stability we have simulated the model

for more than 17,000 breaths on a 2.9GHz 8GB machine and plotted the pleural cavity pressure vs abdominal cavity pressure. The pleural cavity and the abdominal cavity pressures are important indicators of the respiratory muscle efforts as discussed in early sections. We thus plot pleural cavity pressure vs abdominal pressure for a healthy (unperturbed) case and a diseased (perturbed) condition following the quadriplegic patient simulated in the Results section, see Figure 2.14. Further, when we disturb the model parameters, hence simulate with diseased parameters, the system output loops (pleural cavity pressure vs alveolar volume) are closed, indicating a well-behaved system under parameter change.

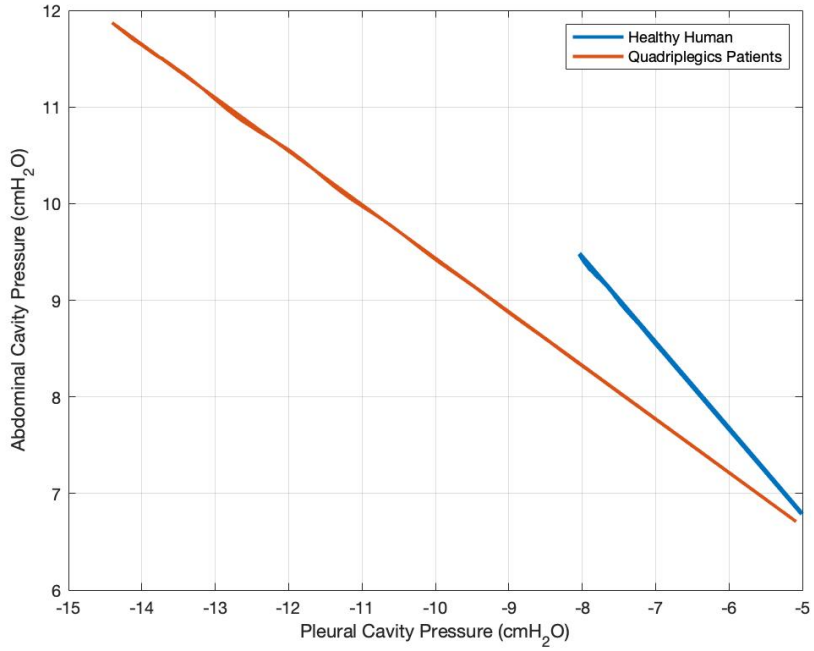

Figure 2. 14: Plot of pleural cavity pressure vs abdominal cavity pressure for long-time breathing simulation (over 17000 breaths) for healthy and quadriplegic patients.

2.4 Discussion

The respiratory muscles and rib cage effects on the lung mechanics is often modeled as solely a negative pressure input P_{mus}. The P_{mus} is a ubiquitous pressure source term that is used in the respiratory community to describe collective respiratory muscle efforts that was coined, anecdotally, by hydraulic ventilator engineers, and it is estimated to have a magnitude of about 4.5-5.5 $\mathrm{cmH_2O}$ during quiet breathing [9],[27],[39]. The value of P_{mus} is computed from a simple equation of motion of the respiratory system, $P_{mus} = P_m - RQ - EV - P_0$, where P_m is the pressure at the mouth, Q is the airflow, V is the tidal volume, R and C are the resistance and compliance of the respiratory system, and P_0 is the alveolar pressure at the end of expiration. Mecklenburgh et al. [57] computed the value of P_{mus} by first estimating the resistance and compliance values of a fully sedated patient with zero P_{mus} using the patient's P_m, Q, and V signals measured at the bed side and the least-squares approach. Then, the P_{mus} was computed from the estimated R and C parameters and the P_m, Q, and V signals measured after the same patient woke up from the sedation and started spontaneously breathing. The computation of P_{mus} is not feasible during clinical practice, since it requires not only the measurements of the pressure and flow at the patient's mouth, but also the estimated lung parameter values (R and C). The P_{mus} signal lumps all the effects of the respiratory muscles and rib cage, however, we cannot differentiate between a respiratory muscle compromised and a rib cage compromised case from a perturbation of the P_{mus} in a diseased condition. In the present work, the respiratory muscles and the rib cage mechanics have been modeled separately in rigor to best capture the latest physiology of human breathing mechanisms. Lung diseases can thus be understood from a parameter perturbation of not just a lumped P_{mus} value, but parameters like pleural cavity compliance (pleural effusion), abdominal cavity compliance (abdominal hypertension), etc.

In this study, we presented a mechanistic model of the respiratory physiology, specifically how the contraction and relaxation of the respiratory muscles affect rib cage mechanics and breathing. The model validated reasonably well against healthy subject data and quadriplegic patient data demonstrating its possible use to run what-if scenarios simulating lung conditions and diseases. As indicated in Figures 2.9, 2.11, and 2.13, the upper and lower ribs rotate about 1.48 degrees and 2.11 degrees during quiet breathing for a healthy human to reach a tidal volume of 500 ml, while the upper and lower ribs rotate about 9.9 degrees and 12.2 degrees for a quadriplegic patient in [56] to reach a tidal volume of 1700 ml. A rib rotation of 2.11 degrees during quiet breathing is a small angular displacement, and a rib rotation of 12.2 degrees can still be considered small relative to a tidal volume of 1700 ml, which is more than three times the human need during quiet breathing. This small angular rotation has a great impact on the lung mechanics variables (alveolar volume, airflow, etc.), thus affecting the gas exchange in the lungs. The diaphragm muscles, the main respiratory muscles, play a critical role in driving respiration. From our simulation, a 100% increase of the contraction force of the diaphragm muscles (input of the model) in healthy state causes an increase of 325% in the LM variables. A 100% increase of the contraction force of the intercostal muscles (input of the model) causes an increase of about 13% of the LM variables. This shows that the diaphragm muscles are the main muscles determining ventilation, and thus the activation of diaphragm muscles can efficiently provide quadriplegic patients enough air for breathing.

2.5 Conclusion

In this chapter, we have demonstrated that a mathematical rib cage mechanics model with the contraction forces of the diaphragm and the intercostal muscles can replicate the rib cage behavior

of a healthy human and of a quadriplegic patient with isolated paced diaphragm. This model includes reasonably realistic respiratory muscle behavior and rib cage mechanics: 1) the inputs of the model are the contraction forces of the diaphragm and the intercostal muscles during quiet breathing that were calculated once from real human measurements (pleural cavity pressure signal, abdominal pressure signal, and the diaphragmatic central tendon displacement measurement) and used subsequently, 2) the rotation of the ribs (bucket handle mechanism) was modeled to represent the change of the thoracic volume following rib cage anatomy, 3) the rib cage was considered as two individual parts (upper and lower rib cage) in order to study the paradoxical movements of the lower and the upper rib cage of quadriplegic patients, 4) the diaphragm direct, appositional, and insertional effects were included following the latest knowledge on the diaphragm muscles. We have also shown through sensitivity analysis that the diaphragm dome surface area, the pleural cavity compliance and the abdominal compliance have a strong impact on lung mechanics variables ($P_A, V_A, Q, etc.$). Further, the simulation of both healthy and diseased (quadriplegic patients) cases were validated with real patient measurements, and our model was able to emulate rib rotation and abdominal and pleural pressures that closely match real patient data in the diseased state. In addition, lung mechanics variables, such as airflow and pressures in different lung compartments (*i.e.* larynx, trachea, bronchi), can be predicted leveraging the proposed lung model.

In future work, personalized parameter values can be adopted in order to simulate different patients, *e.g.*, the dimensions of the rib cage, the diaphragm muscle and the intercostal muscle masses can be estimated individually as a function of a patient's height and weight. Such a model, tuned to an individual, could aid in providing a more optimal diaphragm pacing or in designing a diaphragm stimulator.

2.6 Appendix – State Equation

$$\begin{bmatrix} \dot{v}_{ct} \\ \dot{P}_{abd} \\ \dot{P}_{pl} \\ \dot{\omega}_{lrc} \\ \dot{\omega}_{urc} \\ \dot{\tau} \\ \dot{\theta}_{lrc} \\ \dot{\theta}_{urc} \end{bmatrix} =$$

$$\begin{bmatrix} -\frac{b_{dia}}{m_{ct}} & -\frac{A_{do}}{m_{ct}} & \frac{A_{do}}{m_{ct}} & 0 & 0 & 0 & 0 & 0 \\ \frac{A_{do}}{C_{abd}} & 0 & 0 & -l_{rb}^{l} A_{lrc}^{zoa} \sin(\theta_{l,o} - \theta_l) & 0 & 0 & 0 & 0 \\ -\frac{A_{do}}{C_{pl} + C_l} & 0 & 0 & -\frac{l_{rb}^{l} A_{lrc}^{pl} \sin(\theta_{l,o} - \theta_l)}{C_{pl} + C_l} & -\frac{l_{rb}^{u} A_{urc} \sin(\theta_{u,o} - \theta_u)}{C_{pl} + C_l} & 0 & 0 & 0 \\ 0 & \frac{l_{rb}^{l} A_{lrc}^{zoa} \sin(\theta_{l,o} - \theta_l)}{I_{lrc}} & \frac{l_{rb}^{l} A_{lrc}^{pl} \sin(\theta_{l,o} - \theta_l)}{I_{lrc}} & -\frac{b_{lrc}}{I_{lrc}} & 0 & -\frac{1}{I_{lrc}} & -\frac{k_{lrc}}{I_{lrc}} & 0 \\ 0 & 0 & \frac{l_{rb}^{u} A_{urc} \sin(\theta_{u,o} - \theta_u)}{I_{urc}} & 0 & -\frac{b_{urc}}{I_{urc}} & \frac{1}{I_{urc}} & 0 & -\frac{k_{urc}}{I_{urc}} \\ 0 & 0 & 0 & k & -k & -\frac{k}{b} & 0 & 0 \\ 0 & 0 & 0 & 1 & 0 & 0 & 0 & 0 \\ 0 & 0 & 0 & 0 & 1 & 0 & 0 & 0 \end{bmatrix} \begin{bmatrix} v_{ct} \\ P_{abd} \\ P_{pl} \\ \omega_{lrc} \\ \omega_{urc} \\ \tau \\ \theta_{lrc} \\ \theta_{urc} \end{bmatrix}$$

$$+ \begin{bmatrix} \frac{1}{m_{ct}} & 0 \\ 0 & 0 \\ 0 & 0 \\ 0 & 0 \\ 0 & l_{rb}^{u} \cos(\theta_{u,o} - \theta_u) \\ 0 & 0 \\ 0 & 0 \\ 0 & 0 \end{bmatrix} \begin{bmatrix} F_{dia} \\ F_{int} \end{bmatrix} \qquad (2.5)$$

Chapter III: Pulmonary Function Monitoring: Physiology-based Optimization Algorithm

In this chapter, we present the optimization algorithms that we use to assess patient lung health breath-by-breath. These algorithms take non-invasive measurements at the patient's mouth (airway opening pressure and airflow) and estimate lung resistance, lung compliance, and the patient breathing effort due to the respiratory muscle activity (spontaneous breaths). For passive patients, *i.e.*, completely sedated and ventilated (no spontaneous breaths), well established algorithms have been implemented in modern mechanical ventilators. However, for spontaneous breathing patients, say, when a patient starts to wake up from sedation, while still on ventilatory support, the estimation of the lung parameters is challenging due to the added patient's breathing effort. We can tackle this added difficulty in modeling. In estimation, however, this becomes a challenging problem, one that can no longer be solved using the existed approach for fully sedated patients and demands an iterative technique. To solve this estimation problem, parametric optimization was used with two optimization methods: least-squares (nonetheless, since applications use least-squares during sedation and spontaneous breaths) and the interior point method. A patient lung emulator was built to collect the data to be used for estimation. The lung emulator is a motor-controlled bellow system with adjustable resistance and compliance values built by Quadrus Medical Technologies. The motor applies programmable forces on the bellow system to emulate the human respiratory muscle effect on the lungs. We measure the pressure waveforms at the mouth and inside the bellow (to represent the airway and the lung pressure), and the airflow at the mouth via sensors. Utilizing the developed optimization algorithms along with the data collected from the lung emulator, we manage to estimate the lung mechanics parameters and the respiratory muscle effort within an average percent error of only 5%.

3.1 Introduction

The health of the respiratory system can typically be described by two parameters: 1) the resistance (R_{rs}) and 2) the elastance (E_{rs}), or compliance ($C_{rs} = 1/E_{rs}$). The resistance value measures the tendency of the pulmonary system to oppose airflow, and the compliance measures the lung's ability to stretch and expand. Pulmonary conditions, such as Acute Respiratory Distress Syndrome (ARDS), Chronic Obstructive Pulmonary Distress (COPD), and Idiopathic Pulmonary Fibrosis (IPF) have alterations in the lung resistance and/or compliance values [84][85][86]. In addition, one of the Coronavirus Disease (COVID-19) types is known to have low lung compliance value [19]. Therefore, these two lung mechanics parameters (R_{rs} and C_{rs}) are critical in representing the lung disease since they closely reflect the state of health and functionality of the respiratory system. Unfortunately, however, these two quantities, like most parameters, are not measurable via sensors. Hence, tracking these two parameters can aid clinicians to better diagnose certain diseases and to easily monitor the progression of certain respiratory disease as the patient recovers (the lung mechanics parameters return to the normal values in time). Quantitative assessment of the R_{rs} and C_{rs} also has the potential to optimize the ventilator settings to best meet the patient's ventilation needs. Two common approaches to estimate the lung resistance and the compliance values are available in modern ventilators: 1) a well-established technique that requires a ventilator maneuver, *i.e.*, the end-inspiratory pause maneuver, known as EIP [87], and 2) a noninvasive, maneuver-free method using least-squares (LS). Both approaches do not require invasive measurements, however, the first approach requires maneuver that interferes the normal operation of mechanical ventilation and might cause a little discomfort to patients and cannot continuously report the R_{rs} and C_{rs} values. Although the second method (LS) provides accurate results, it only applies to fully sedated patients. For partially sedated or non-sedated mechanical

ventilated patients, (or for patients waking up from sedation), the contraction of the respiratory muscles (diaphragm, intercostal, and accessary muscles) increases the pleural cavity volume via chest wall expansion, generating a negative pressure on the patient lungs along with the mechanical ventilation, known as P_{mus}. When the patient is breathing spontaneously, P_{mus} is not a negligible driving force. Therefore, when applying the same approaches used for sedated patients on patients who breathe spontaneously, the estimation performance degrades significantly (we have re-created this scenario). The goal of this work is to develop an algorithm that monitor the respiratory mechanics (R_{rs}, C_{rs}) and the respiratory muscle effort (P_{mus}) breath by breath for spontaneous breathing patients with ventilator support. In addition, the algorithm shall 1) use measurements that are routinely measured at the bedside, and 2) shall require no additional instrumentation, and 3) shall cause no interference with the normal operation of the ventilator.

Our group has previously proposed two approaches to non-invasively estimate $R_{rs}, C_{rs},$ and P_{mus} waveform [27][88]: 1) a parametric optimization algorithm utilizing LS, and 2) a constrained nonlinear optimization using MATLAB toolbox. In the first method, linear functions are adopted to approximate the P_{mus} waveform during inspiration and expiration based on respiratory muscle physiology. The P_{mus} waveform is thus parameterized to two pressure values to estimate, the pressure at the beginning of inspiration and at the end of inspiration. Instead of estimating a P_{mus} value at every sampling time (sampling frequency = 100 Hz), only two values are estimated per breath, which is much more computationally efficient. In the second method, the quadprog (quadratic programming) MATLAB function is leveraged to perform the estimation, including constraints on the P_{mus} waveform. Using that built-in function, a P_{mus} value is estimated at every data sampling time. In this work, we continue to improve the estimation performance following

our old work, and program the optimization algorithm without leveraging any built-in MATLAB function.

This work proposes a parametric optimization that adopts a more physiological P_{mus} waveform (2^{nd} order functions) using interior point method (IPM) with Newton-Raphson method to solve nonlinear constrained optimization problems. We programmed IPM and a backtracking line search technique to compute the optimal solution, whose details are shown in the Method section. We have also compared the proposed algorithm to the LS optimization method from [27][88]. To test our algorithm, we built a lung emulator that represents human lungs' physical properties and generates patients' spontaneous breathing. Data collected from this lung emulator was used to test the algorithm.

In the Method section, we first introduce the setup of the patient lung emulator and the data collection. We then describe the optimization methods and the programming routine. In the results section, we present and compare the estimation results using different algorithms, least squares and interior point method. In the Discussion section, we analyze and summarize the algorithm performance, *i.e.*, why least-squares may fail in the optimization problem. Finally, we conclude and highlight future extensions of this work.

3.2 Method

3.2.1 Lung Emulator and the Simplistic Lung Mechanics Model

We have built a lung emulator to represent human lungs in the lab of Quadrus Medical Technologies as shown in Figure 3.1. The passive bellow system is a product called QuickLung from IngMar Medical. This device emulates the mechanical properties of the respiratory system (resistances and compliances) with adjustable parabolic resistances (5, 20, 50 $cmH_2O/L/s$) and

compliances (50, 20, 10 mL/cmH_2O). However, the QuickLung does not generate spontaneous breaths, hence it can only emulate fully sedated patients. In order to test algorithms on patients who breathe spontaneously, we have applied a programmable torque on the QuickLung bellow to emulate the respiratory muscle effects on the lungs. As shown in Figure 3.1, two aluminum lift arms (wings) are rotated by the controlled motor torque. These two arms lift the upper plate of the QuickLung causing bellow expansion, and spontaneous breath happens.

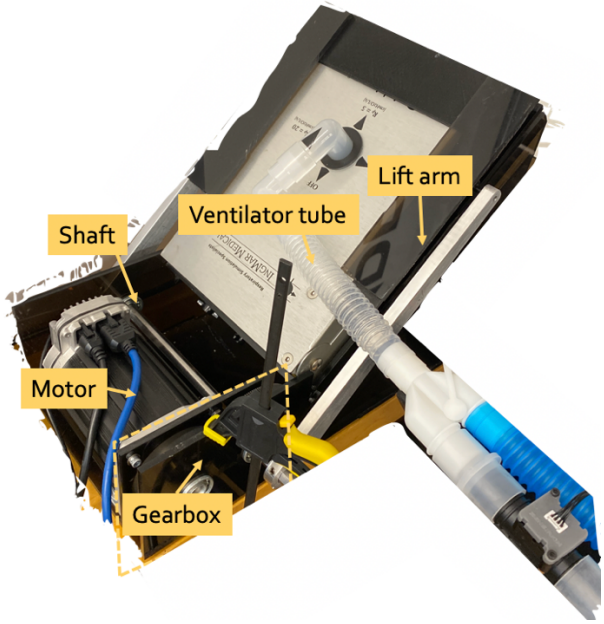

Figure 3. 1: Lung emulator with adjustable resistance, compliance values, and programmable respiratory muscle efforts.

The lung emulator is developed to represent a simplistic human respiratory system, more specifically, a single-compartment first-order linear model that is widely accepted in the respiratory research community [25]. We describe this simplistic lung mechanics model using a linear graph as shown in Figure 3.2. We employ this graphing technique to allow for a systematic formulation of the system's dynamic equations [9]. These equations consist of variables and parameters. Parameters represent material property and geometry of the lung compartments, such as hydraulic resistances and capacitors. Pressures and volumes are termed variables, which could

potentially be measured through an instrument. In Figure 3.2, every node (solid circle) represents the pressure within a compartment of the respiratory system, *e.g.*, P_L represents the lung pressure. Every line with an arrow represents a flow between two compartments and is labeled with the associated parameter of that segment. The P_{mus} value, note as the straight-dashed line in Figure 3.2, is the negative pressure generated by the contraction of the respiratory muscles, and the P_{mus} serves as the reference pressure of the lung pressure (P_L). The atmospheric pressure (P_{atm}) serves as the reference pressure of the airway pressure (P_{ao}).

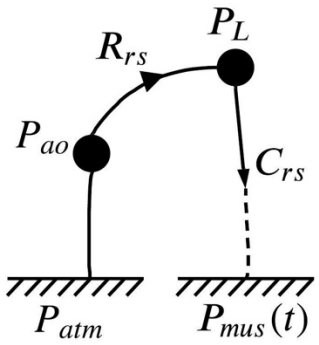

Figure 3. 2: Linear graph of the simplistic lung mechanics system. P: pressure, R: resistance, C: compliance, ao: airway opening, L: lungs, rs: respiratory system, atm: atmosphere, mus: respiratory muscles.

The dynamic equation of the system is thus derived as the following:

$$\dot{P}_L = \frac{1}{C_{rs}}\left(\frac{P_{ao} - P_L}{R_{rs}}\right) + \dot{P}_{mus} \tag{3.1}$$

where P_L is the lung pressure, P_{ao} is the airway opening pressure, P_{mus} is the negative pressure generated by the respiratory muscles, R_{rs} is the lung resistance, and C_{rs} is the lung compliance.

Our goal is to construct an equation of motion that relates the non-invasive measurements (P_{ao}, airflow) at the bedside to the parameters of interest, R_{rs}, C_{rs} and P_{mus}. To achieve this, we add $R_{rs}Q(t)$ on both sides of Equation 3.1 and solve for Pao, which yields the following equation of motion:

$$P_{ao}(t) = \frac{1}{C_{rs}} V(t) + R_{rs} Q(t) + P_{mus} + P_0 \tag{3.2}$$

where $V(t)$ represents the volume of air inhaled from the beginning of the breath ($t = 0$), and P_0 is the pressure at the airway opening at $t = 0$ ($V(0) = Q(0) = P_{mus}(0) = 0$). This is the equation of motion that relates the parameters of interest directly to pressure and flow data measured at patient's mouth. This model is also well-known in the literature as the linear first-order single-compartment model of respiratory mechanics [25].

The P_{mus} waveform for healthy human during quiet breathing is shown in Figure 3.3. The input to the lung model P_{mus} is represented in Equation 3.3 from Albanese *et al.* [1]. The P_{mus} waveform is modeled as exponential functions, generating negative pressures during inspiration, and returns back to zero during expiration.

$$P_{mus}(t) = \begin{cases} -\frac{P_{mus,min}}{T_I T_E} t^2 + \frac{T \cdot P_{mus,min}}{T_I T_E} t & (Insp) \\ \frac{P_{mus,min}}{\left(1 - e^{-\frac{T_E}{\tau}}\right)} \left(e^{-\frac{t - T_I}{\tau}} - e^{-\frac{T_E}{\tau}}\right) & (\text{Exp}) \end{cases} \tag{3.3}$$

where T_I is the inspiration time, T_E is the expiration time, T is the total time for one breath, τ is the time constant of the exponential expiratory profile, and $P_{mus,min}$ is the minimum end inspiratory pressure value representing the amplitude of the inspiratory efforts. During quiet breathing, $P_{mus,min}$ is 5 cmH_2O, τ is 0.44 s, the respiratory rate is set as 12 breaths/min (bpm), and the I:E ratio (ratio of the inspiratory time to the expiratory time) to 0.6 [1]. The motor of the lung emulator was programmed to generate a force waveform that is applied on the bellow to emulate P_{mus} with adjustable P_{mus} magnitude, respiratory rate, IE ratio, and time constant by controlling the pulse width modulation command to the motor.

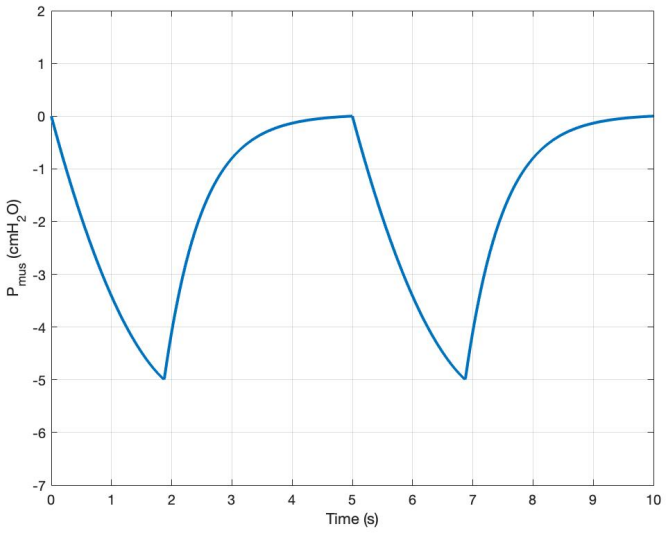

Figure 3. 3: The P_{mus} waveform in time for healthy human during quiet breathing.

3.2.2 Data Collection

From the lung emulator, we measured the pressure and the flow waveforms via the Allsensors pressure sensors and a Sensirion flow sensor. Sample data with 100 Hz sampling frequency are shown in Figure 3.4 with patient settings: R_{rs} 5 cm H_2O /L/s, C_{rs} 0.05 L/cm H_2O, P_{mus} 5 cmH_2O, RR 12 bpm, and ventilator settings: PSV mode, IE ratio 0.6, pressure 15 cmH_2O. The sample data contains 33 consecutive breaths of three measurements: the airway opening pressure, airflow, and the lung pressure. Note that a major difference between the human data and the lung emulator data is that the lung emulator data does not contain the frequency component from the cardiac cycle (heart beats). Thus, we do not observe the higher frequency noise from the heart beats. However, the respiratory characteristics are maintained in these waveforms, which is adequate to estimate the lung mechanics parameters and the respiratory muscle efforts as shown in the accepted equation of motion above (Equation 3.2).

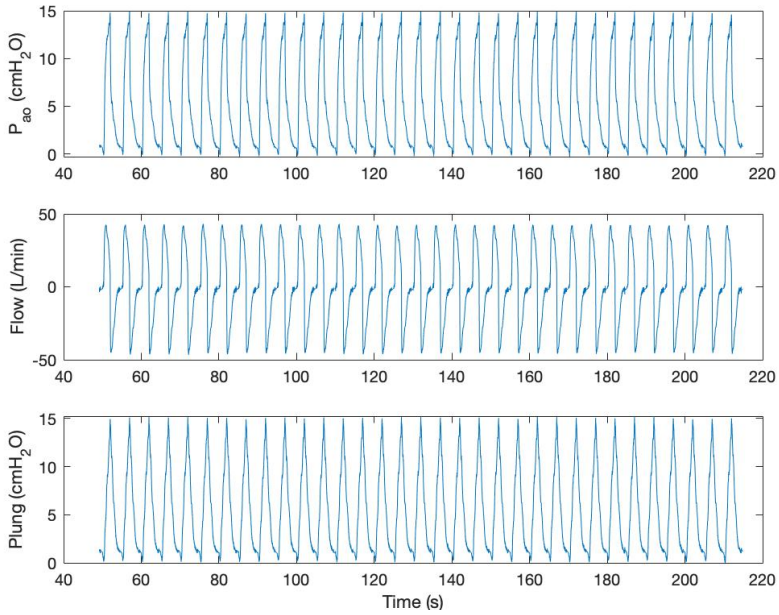

Figure 3. 4: Sample data of airway opening pressure, airflow and lung pressure for patient settings: R_{rs} 5 $\mathrm{cmH_2O/L/s}$, C_{rs} 0.05 $L/\mathrm{cmH_2O}$, P_{mus} 5 $\mathrm{cmH_2O}$, RR 12 bpm, and ventilator settings: PSV mode, IE ratio 0.6, and pressure 15 $\mathrm{cmH_2O}$.

3.2.3 Optimization Methods

In this section, we first introduce the least-squares approach and interior point method (IPM). Then we describe how we use parametric optimization to estimate the resistance value, the compliance value, and P_{mus} waveform breath by breath using the data that was collected from the lung emulator device.

3.2.3.1 Least-squares Approach

Many physical systems may be represented as a linear system of equations, $Ax = b$, where the matrix A and the vector b are known measured signals, and the vector x is an unknown parameter vector, *e.g.*, the proposed simplistic lung mechanics model (Equation 2) is an algebraic equation that can be written in such form. If A is a square, invertible matrix, then there exists a unique

solution x for every b. However, when A is either singular or rectangular, there may be one, none, or infinitely many solutions, depending on the b and A matrix. Take the respiratory system of a sedated patient as an example, since there are more data (100 sampling frequency) than unknowns (R_{rs}, C_{rs}), the system is an overdetermined system (*i.e.*, a tall-skinny A matrix). Follow the equation of motion, *i.e.*, $P_{ao} = E_{rs}V + R_{rs}Q$, we can formulate it as $Ax = b$, as:

$$\begin{bmatrix} V(0) & Q(0) \\ \vdots & \vdots \\ V(t_t) & Q(t_t) \end{bmatrix} \begin{bmatrix} E_{rs} \\ R_{rs} \end{bmatrix} = \begin{bmatrix} P_{ao}(0) \\ \vdots \\ P_{ao}(t_t) \end{bmatrix} \tag{3.4}$$

The goal is to find the solution x of this overdetermined system that minimizes the sum-squared error $\|Ax - b\|_2^2$, the so-called least-squares solution. The solution can be computed via singular value decomposition (SVD) of A matrix: $A = \tilde{U}\tilde{\Sigma}\tilde{V}^T$, where U is an orthogonal matrix whose columns are the eigenvectors of $AA^\top$, known as the left-singular matrix, V is an orthogonal matrix whose columns are the eigenvectors of $A^\top A$, known as the left-singular matrix, and Σ is a diagonal matrix of the form whose elements are the square roots of the eigenvalues of $A^\top A$, known as singular values of A. Each of these matrices can be inverted, resulting in the Moore-Penrose left pseudo-inverse [89]: $A^\dagger = \tilde{V}\tilde{\Sigma}^{-1}\tilde{U}^T$. The solution x can thus be computed from $x = A^\dagger b$.

3.2.3.2 Interior Point Method

The IPM method is hereby introduced. We start from a general constrained optimization as the following:

$$\begin{aligned} &\text{Minimize} \quad f_o(x) \\ &\text{Subject to: } f_i(x) < 0, i = 1, \dots, m \\ &Ax = b \end{aligned} \tag{3.5}$$

where f_0 is the objective function, f_i is the inequality constraint function and $Ax = b$ is the equality constraints. Assume $f_o, \dots, f_m$ are convex and twice continuously differentiable, and $A \in R^{p \times n}$ with rank $A = p < n$. We can use the interior point method with the barrier method [90] to solve convex optimization problems that include equality and inequality constraints. This method reduces the original optimization problem to an equality constrained problem by presenting inequality constraints as log functions in the objective function. The basic idea of the barrier method is to punish the objective function whenever inequality conditions do not hold. The original optimization problem thus converts into the following:

$$\text{Minimize} \quad f_0(x) - \frac{1}{t}\sum_{i=1}^{m} \log(-f_i(x)) \tag{3.6}$$

$$\text{Subject to: } Ax = b$$

The new objective here is still convex, since $-\frac{1}{t} log(-f_i(x))$ is convex and differentiable. The $-\sum_{i=1}^{m} \log(-f_i(x))$ is called the logarithmic barrier for the problem. Note that the new optimization problem is only an approximation of the original problem. As the parameter t increases, the new problem (Equation 3.6) is converging to the original problem (Equation 3.5). However, when the parameter t is large, the objective function is difficult to minimize by Newton's method, since its Hessian, *i.e.*, the square matrix of the second-order partial derivatives of the objective function, varies rapidly near the boundary of the feasible solution. This is because the punishment term $-\frac{1}{t} log(-f_i(x))$ shoots to positive infinity as the solution gets closer to the boundary of the feasible solution. To resolve this issue, the centering path, *i.e.*, an iterative process with increasing t values, is adopted. As shown in Figure 3.5A, the centering path associated with the problem is defined as the set of points $x^*(t)$ with increasing positive *t* values, which we call the central points. In optimization theory, one optimization problem may be viewed from either of two perspectives, the primal or the dual problem. The solution to the dual problem provides a lower

bound to the solution of the primal problem (the original optimization problem Equation 3.6). In the centering path, every central point ($x^*(t)$) yields a dual feasible point, and hence a lower bound on the optimal value. The duality gap, *i.e.*, the difference between the primal and dual solutions, associated with $x^*(t)$ and its dual solution is m/t. Therefore, when the optimization terminates at a duality gap (m/t) less than an error value ϵ set by the user, we call this optimal solution as the ϵ-suboptimal solution of the original problem. The step to compute $x^*(t)$ given a t value is called a centering step. The algorithm routine is summarized in Figure 3.5A.

Figure 3.5B summarized the centering step, where we use the Newton-Raphson method to solve for the Karush–Kuhn–Tucker (KKT) conditions, the necessary condition of the optimization problem. The KKT condition has:

$$\begin{cases} \nabla f_0(x) + \sum_{i=1}^{m} \frac{1}{-t f_i(x)} \nabla f_i(x) + A^T \lambda = 0 \\ Ax = b \end{cases} \tag{3.7}$$

λ is the Lagrange multiplier. Equation 3.7 is derived from the first order derivative of the objective function, and the equality constrains. To compute the Newton step (search direction) from Equation 3.7, we form the Taylor approximation for the nonlinear term ($\nabla f_0(x) + \sum_{i=1}^{m} \frac{1}{-t f_i(x)} \nabla f_i(x)$) occurring in the first equation. For v small, we have the Taylor approximation:

$$\nabla f_0(x+v) + \sum_{i=1}^{m} \frac{1}{-t f_i(x+v)} \nabla f_i(x+v) \approx \nabla f_0(x) + \sum_{i=1}^{m} \frac{1}{-t f_i(x)} \nabla f_i(x) + \nabla^2 f_0(x) v +$$

$$\sum_{i=1}^{m} \frac{1}{-t f_i(x)} \nabla^2 f_i(x)\, v + \sum_{i=1}^{m} \frac{1}{-t f_i(x)^2} \nabla f_i(x) \nabla f_i(x)^T v \tag{3.8}$$

which can be written as

$$Hv + A^T \lambda = -g \tag{3.9}$$

where

$$H = \nabla^2 f_0(x) + \sum_{i=1}^{m} \frac{1}{-tf_i(x)} \nabla^2 f_i(x) + \sum_{i=1}^{m} \frac{1}{-tf_i(x)^2} \nabla f_i(x) \nabla f_i(x)^T$$

$$g = \nabla f_0(x) + \sum_{i=1}^{m} \frac{1}{-tf_i(x)} \nabla f_i(x)$$

H is the Hessian matrix (the last three terms on the right side of the Equation 3.8), and g is the Jacobian matrix (the first two terms on the right side of the Equation 3.8). To solve for the search direction, *i.e.*, the Newton step, we write the above equations into the matrix form:

$$\begin{bmatrix} H & A^T \\ A & 0 \end{bmatrix} \begin{bmatrix} \Delta x \\ \lambda \end{bmatrix} = \begin{bmatrix} -\mathrm{g} \\ 0 \end{bmatrix} \tag{3.10}$$

where Δx is the searching direction, λ is the Lagrange multiplier, and A is the matrix of the equality constraints.

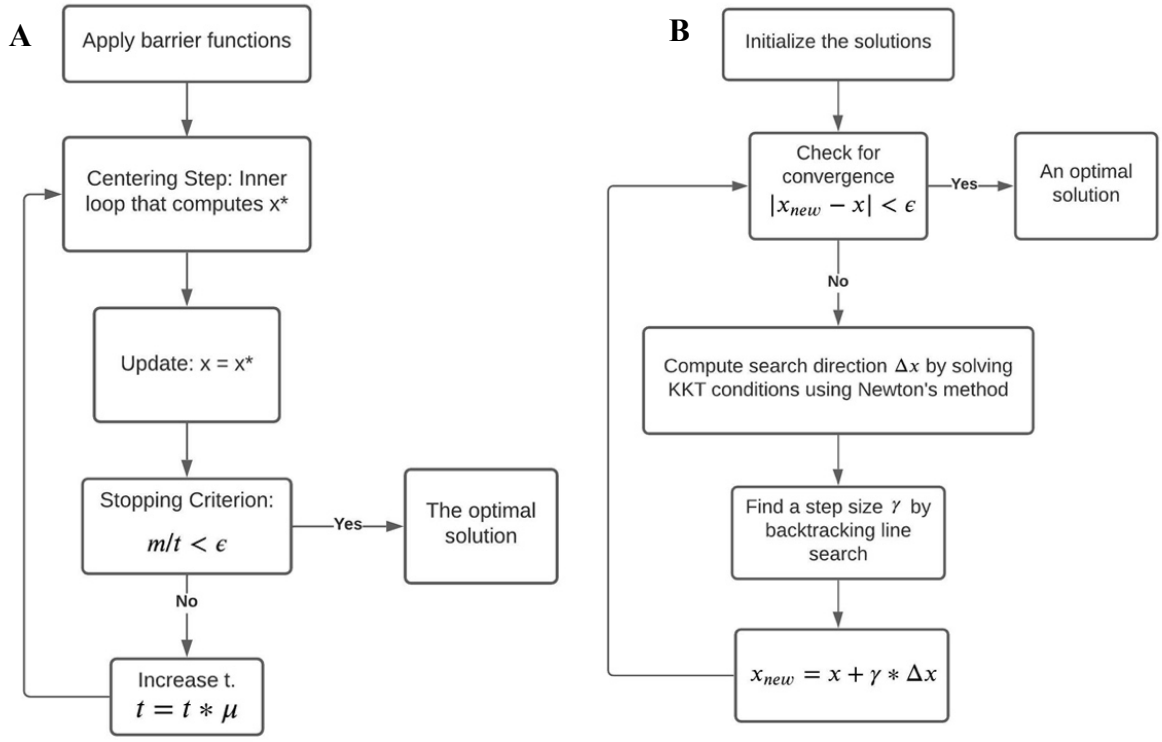

Figure 3. 5: Interior point method optimization routine. A: the centering path, B: the centering step.

Once we find the search direction, we use a backtracking line search technique to find the step size γ [90]. A backtracking line search technique is termed as such because it starts with unit step size and then reduces it (backtracks) by the factor β until the stopping condition $f\ (x\ + \gamma \Delta x)\ \leq\ f\ (x)\ +\ \alpha\gamma \nabla f\ (x)^T\ \Delta x$ holds, with $0 < \alpha < 0.5, 0 < \beta < 1$.

3.2.4 Parametric Optimization

The lung equation of motion (Equation 3.2) can be rewritten as $P_{ao}(t) = \frac{1}{C_{rs}} V(t) + RQ(t) + \tilde{P}_{mus}$, where $\tilde{P}_{mus} = P_{mus} + P_0$. Hence, we have the objective function:

$$Min\ J = \sum_{t=0}^{t=t_t} \left(P_{ao}(t) - \left(RQ(t) + EV(t) + \tilde{P}_{mus}(t) \right) \right)^2 \tag{3.11}$$

where J is the cost of the objective function. Researchers have used parametric optimization to estimate respiratory mechanics and respiratory muscle effort [88]. Based on respiratory muscle physiology, Vicario *et al.* parameterized the P_{mus} waveform as linear functions for inspiration ($0 \leq t < t_m$), muscle force releasing ($t_m \leq t < t_r$) and muscle relaxation ($t_r \leq t < t_t$) shown in Figure 3.6A. By doing so, a simple but realistic mathematical expression is structured to represent P_{mus}(t) with only two pressure values. The piecewise function representing the P_{mus} waveform shown in Figure 3.6A is derived as:

$$\tilde{P}_{mus} = \begin{cases} P_q \left(1 - \dfrac{t}{t_m}\right) + P_m \dfrac{t}{t_m} & 0 \leq t < t_m \\ P_q(1 + \dfrac{t - t_q}{t_q - t_m}) + P_r(1 - \dfrac{t - t_m}{t_q - t_m}) & t_m \leq t < t_q \\ P_q & t_q \leq t < t_t \end{cases} \tag{3.12}$$

where P_q is the initial $\tilde{P}_{mus}$ pressure and the pressure after muscle force releasing, P_m is the pressure at the end of inspiration, t_m is the time at the end of inhalation, t_r is the time at the end

of muscle force releasing, and t_t is the time at the end of exhalation. The $\tilde{P}_{mus}$ is parameterized as two unknowns, P_r, and P_q.

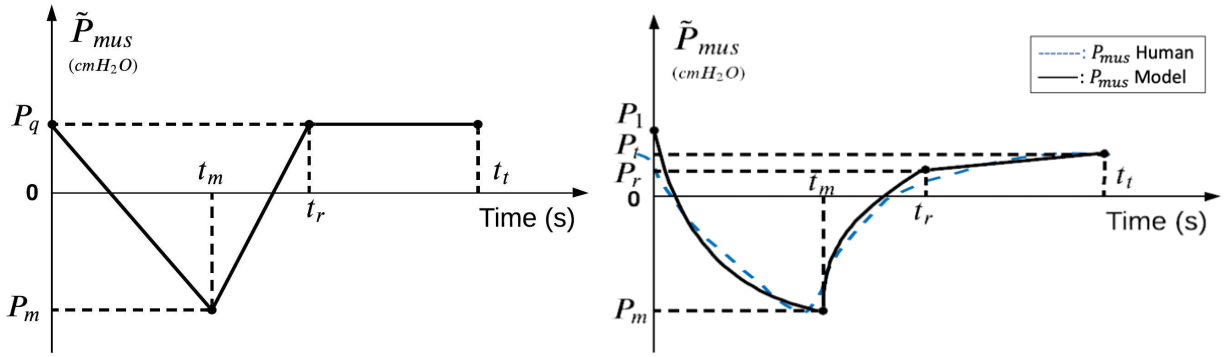

Figure 3. 6: Parameterized P_{mus} waveforms. A: linear P_{mus} parametric function for inspiration and exhalation. P_q: the P_{mus} pressure at the beginning of inspiration and the end of expiration, P_m: the pressure at the end of inspiration, t_m: time at the end of inhalation, t_r: time at muscle relaxation, t_t: time at the end of exhalation. B: quadratic P_{mus} parametric function (black), and real human P_{mus} waveform (blue) measured by Mecklenburgh [57]. P_1: initial P_{mus} pressure, P_r: the P_{mus} pressure at the end of muscle force releasing, P_t: P_{mus} pressure at the end of exhalation.

In this work, we parameterized the $\tilde{P}_{mus}$ waveform based on the real human P_{mus} measurement by Mecklenburgh [57], plotted as blue dashed line in Figure 3.6B. The blue dashed line shows the shape of human P_{mus} waveform, serving as the guide to the P_{mus} parametric function. A closer matching to the real human data can be achieved by approximating the P_{mus} waveform as quadratic functions for inspiration ($0 \leq t < t_m$) and muscle force releasing ($t_m \leq t < t_r$), and we approximate the muscle relaxation ($t_r \leq t < t_t$) as a linear function, as shown as black solid line in Figure 3.6B. We also set the pressure values different at 0, t_r and t_t, unlike the work by Vicario *et al.* (same pressure values at 0, t_r and t_t). The piecewise function that represents the P_{mus} waveform is derived as the following:

$$\tilde{P}_{mus} = \begin{cases} P_1 \dfrac{(t-t_m)^2}{t_m^2} + P_m \left(1 - \dfrac{(t-t_m)^2}{t_m^2}\right) & 0 \le t < t_m \\ P_m \left(\dfrac{t-t_3}{t_3-t_m}\right)^2 + P_r \left(1 - \left(\dfrac{t-t_3}{t_3-t_m}\right)^2\right) & t_m \le t < t_r \\ P_t \left(1 + \dfrac{t-t_t}{t_t-t_r}\right) + P_r \left(1 - \dfrac{t-t_r}{t_t-t_r}\right) & t_r \le t < t_t \end{cases} \quad (3.13)$$

where P_1 is the initial $\tilde{P}_{mus}$ pressure, P_m is the pressure at the end of inspiration, P_r is the $\tilde{P}_{mus}$ pressure at the end of muscle force releasing, P_t is the $\tilde{P}_{mus}$ pressure at the end of exhalation, t_m is the time at the end of inhalation, t_r is the time at end of muscle force releasing, and t_t is the time at the end of exhalation. The $\tilde{P}_{mus}$ is parameterized as four unknowns that are $P_1, P_m, P_r, and\ P_t$.

3.2.5 Optimization Setup

We have two P_{mus} parametric functions (Equation 3.12 and 3.13) and two optimization algorithms (LS and IPM). In this work, we test the two optimization algorithms with both P_{mus} parametric functions separately, using the lung emulator data.

As shown in Figure 3.7, the initial set of t_m, t_r values in both parametric functions (Equation 3.12 and 3.13) are determined from the P_{ao} measurement. The time when P_{ao} reaches its maximum within one breath is taken to be t_m. The value of t_r is approximated by the intersection between the P_{ao} at zero and a linear line between the maximal P_{ao} value and the following hump. Then we vary the initial approximation of the t_m, t_r pair and solve for the optimal solutions from the given t_m, t_r pair. We fix $t_m < t_r$ and vary t_m, t_r by – 0.5 to 0.5 second for a breath of 5 seconds. Finally, we select the pair of t_m and t_r that has the minimal cost (residual sum of squares) as summarized in Figure 3.8.

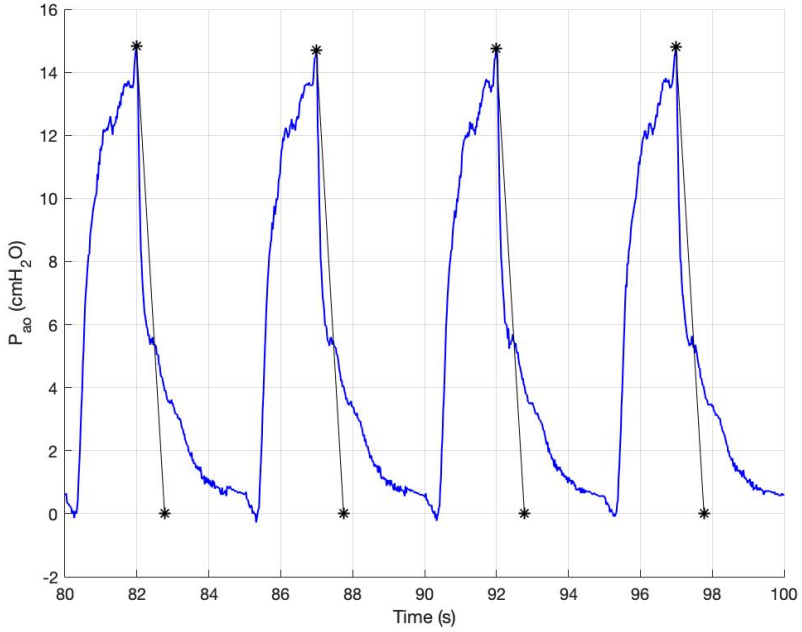

Figure 3. 7: The initial approximate of time stamps t_m, t_r (black asterisks) from P_{ao} waveform (blue).

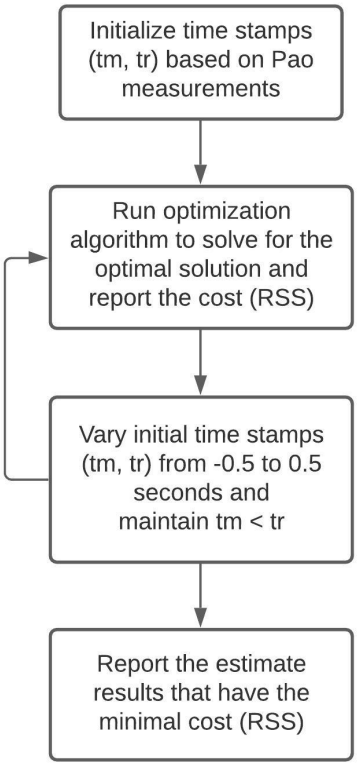

Figure 3. 8: Programming routine of finding the best pair of t_m, t_r. RSS: residual sum of squares.

In the following, taking the IPM method with the quadratic parametric P_{mus} function as an example, we show the setup of the optimization problem.

For the IPM method, we setup the optimization problem by implementing the $\tilde{P}_{mus}$ piecewise function, we have:

$$Minimize\ J = \sum_{t=0}^{t=t_m-\Delta t} \left(P_{ao}(t) - (R_{rs}Q(t) + E_{rs}V(t) + \frac{(t-t_m)^2}{t_m^2} P_1 + (1 - \frac{(t-t_m)^2}{t_m^2})P_m) \right)^2$$

$$+ \sum_{t=t_m}^{t=t_r-\Delta t} \left(P_{ao}(t) - (R_{rs}Q(t) + E_{rs}V(t) + \left(\frac{t-t_r}{t_r-t_m}\right)^2 P_m + (1 - \left(\frac{t-t_r}{t_r-t_m}\right)^2)P_r) \right)^2$$

$$+ \sum_{t=t_r}^{t=t_t} \left(P_{ao}(t) - (R_{rs}Q(t) + E_{rs}V(t) + P_t\left(1 + \frac{t-t_t}{t_t-t_r}\right) + P_r\ \left(1 - \frac{t-t_r}{t_t-t_r}\right)) \right)^2$$

$$Subject\ to\ 0 \le R_{rs} \le 100, 0 \le E_{rs} \le 100, P_m < P_r < P_t, P_m < P_1$$

where the three terms in the cost function J are the equation of motion (Equation 3.11) in the three breathing states defined in the quadratic parametric function (3.11), i.e., inspiration, muscle force releasing and muscle relaxation. We choose to minimize the sum of squared errors of the lung mechanics model instead of formulating the entropy as our objective function, because we are interested in a good fit of the lung mechanics model, and not in optimizing energy.

The bounded physiological constraints [0,100] are included for R_{rs} and E_{rs}. It is a range that covers all the physiological lung mechanics parameter values [88]. The shape of P_{mus} waveform is maintained with the constraints $P_m < P_r < P_t$ and $P_m < P_1$. Then we can follow the programming routine in Figure 3.5 to compute the optimal solution.

For the LS approach, the least-squares setup follows the work from Vicario *et al.* [27], which is derived from Equation 3.2, written in the form of $b = Ax$, where b is the P_{ao} signal, and A consists of flow, volume and the coefficients of the P_{mus} parametric function.

$$\begin{bmatrix} P_{ao}(0) \\ \vdots \\ P_{ao}(t_m - \Delta t) \\ P_{ao}(t_m) \\ \vdots \\ P_{ao}(t_r - \Delta t) \\ P_{ao}(t_r) \\ \vdots \\ P_{ao}(t_t - \Delta t) \end{bmatrix} =$$

$$\begin{bmatrix} Q(0) & V(0) & \frac{(0-t_m)^2}{t_m^2} & (1-\frac{(0-t_m)^2}{t_m^2}) & 0 & 0 \\ \vdots & \vdots & \vdots & \vdots & \vdots & \vdots \\ Q(t_m-\Delta t) & V(t_m-\Delta t) & \frac{(t_m-\Delta t-t_m)^2}{t_m^2} & (1-\frac{(t_m-\Delta t-t_m)^2}{t_m^2}) & 0 & 0 \\ Q(t_m) & V(t_m) & \frac{(t_m-t_m)^2}{t_m^2} & (1-\frac{(t_m-t_m)^2}{t_m^2}) & 0 & 0 \\ \vdots & \vdots & \vdots & \vdots & \vdots & \vdots \\ Q(t_r-\Delta t) & V(t_r-\Delta t) & 0 & \left(\frac{t_r-\Delta t-t_r}{t_r-t_m}\right)^2 & (1-\left(\frac{t_r-\Delta t-t_r}{t_r-t_m}\right)^2) & 0 \\ Q(t_r) & V(t_r) & 0 & \left(\frac{t_r-t_r}{t_r-t_m}\right)^2 & (1-\left(\frac{t_r-t_r}{t_r-t_m}\right)^2) & 0 \\ \vdots & \vdots & \vdots & \vdots & \vdots & \vdots \\ Q(t_t-\Delta t) & V(t_t-\Delta t) & 0 & 0 & \left(1-\frac{t_t-\Delta t-t_r}{t_t-t_r}\right) & \left(1+\frac{t_t-\Delta t-t_t}{t_t-t_r}\right) \end{bmatrix} \begin{bmatrix} R_{rs} \\ E_{rs} \\ P_1 \\ P_m \\ P_r \\ P_t \end{bmatrix}$$

(3.14)

The matrix $[R_{rs}, C_{rs}, P_1, P_m, P_r, P_t]^T$ in Equation 3.14 can be solved by applying the pseudo-inverse of the A matrix, $x = A^{\dagger}b$.

3.3 Results

In this section, the optimization algorithms with two parameterized P_{mus} waveforms are tested with the data collected from the lung emulator.

3.3.1 Parametric Optimization – Least-squares with Linear P_{mus} Function

We first test the parametric optimization algorithm proposed by Vicario *et al.*, *i.e.*, linear P_{mus} parametric function and the least-squares optimization algorithm. The estimation of resistances, compliances and P_{mus} magnitudes for every breath are shown in Figure 3.9. The blue dots are the estimation using parametric optimization (LS), and the red dots are the true parameter values. Since the resistance setting of the lung emulator is flow dependent, we compute the true R_{rs} leveraging the invasively measured signal P_{lung} to validate the resistance estimates. We compute $R_{rs}^{true} = Q^{\dagger}\left(P_{ao} - P_{lung}\right)$ from the continuity equation, $Q = \frac{P_{ao} - P_{lung}}{R_{rs}}$. Using the collected data, we formulate this equation into matrix form, *i.e.*, $\begin{bmatrix} Q(0) \\ \vdots \\ Q(t_t) \end{bmatrix}[R_{rs}] = \begin{bmatrix} P_{ao}(0) - P_{lung}(0) \\ \vdots \\ P_{ao}(t_t) - P_{lung}(t_t) \end{bmatrix}$. The true R_{rs} can thus computed by $Q^{\dagger}\left(P_{ao} - P_{lung}\right)$.

In Figure 3.9, using LS approach with linear parametric function (Equation 3.12), the average percent errors for the lung resistance, the lung compliance, and the P_{mus} magnitude estimates are 19.99%, 1.43% and 4.53% respectively. The lung compliance and P_{mus} estimations are fairly accurate with a percent error of less than 5%, however, the resistance estimate has poor performance. This is expected, since the real P_{mus} pressure values at different states, *i.e.*, the beginning of inspiration, the end of muscle force releasing and the end of expiration, are not the same according to the P_{mus} measurement shown in Figure 3.6B. In addition, the linear shape assumption of the P_{mus} parametric function (Equation 3.12) does not agree with the measured human data. Linear P_{mus} parametric function may be an acceptable approximation as a first step, however, the true P_{mus} waveform is not linear during inspiration and expiration as shown in Figure 3.6B. In the following, we adopt the parabolic P_{mus} parametric function (Equation 3.13) that has

different pressure values at different breathing states (four pressure values), and we expect better estimation results.

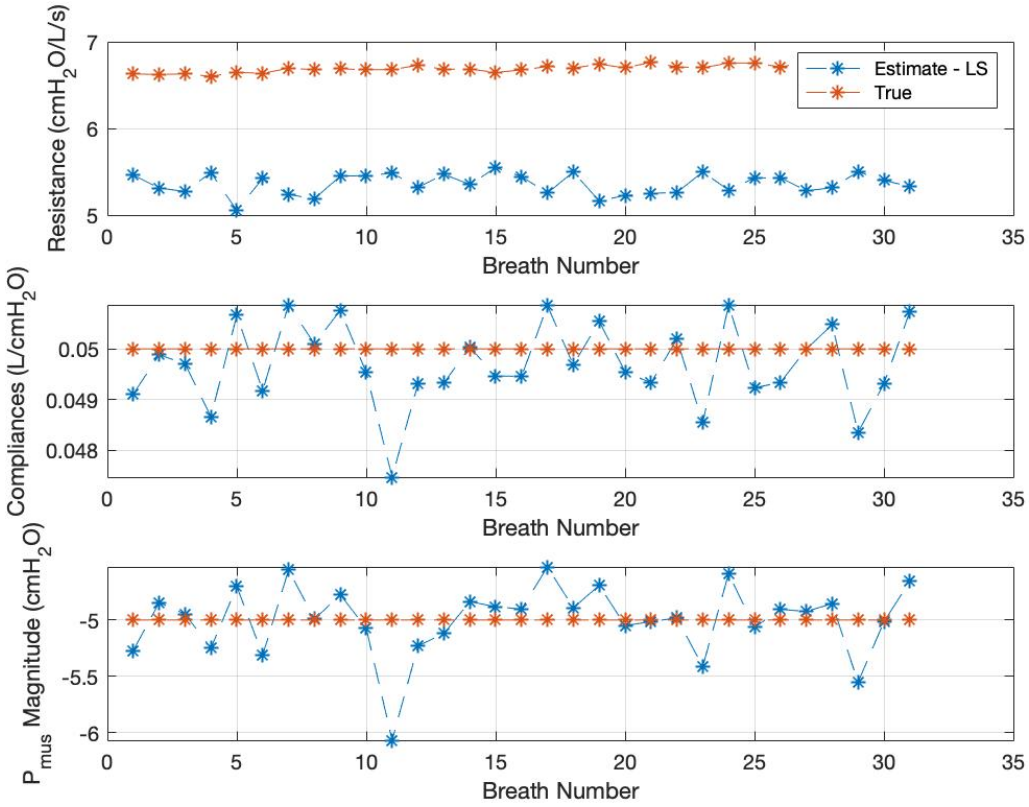

Figure 3. 9: The resistance, compliance and P_{mus} magnitude estimates using least-squares (blue) and IPM with Newton-Raphson's method (black). The true parameter values are plotted in red. This estimation uses the linear P_{mus} parametric function (Figure 3.6A).

3.3.2 Parametric Optimization – Least-squares and IPM with Quadratic P_{mus} Function

Figure 3.10 shows the lung resistance, the lung compliance, and the P_{mus} magnitude estimates using least-squares (blue) and IPM method (black) with the quadratic P_{mus} parametric function (Equation 3.13). The average percent errors using the IPM method are 2.47%, 1.27% and 5.38% for the lung resistance, the lung compliance, and the P_{mus} magnitude, respectively. The interior point method with Newton-Raphson method successfully estimate the lung mechanical properties and the respiratory muscle effort with minimal error. Comparing to the LS method with the linear

P_{mus} function, the resistance estimate improved with a percent error increase of 17.53% (from 19.99% to 2.47%). For the least-squares method, the average percent errors are 5.73%, 52.11% and 138.90% for the lung resistance, the lung compliance, and the P_{mus} magnitude, respectively. The least-squares with quadratic P_{mus} function completely failed the estimation. Figure 3.11 shows the P_{mus} waveform estimate using least-squares (blue) and IPM with Newton-Raphson's method (black). Same conclusion can be drawn that least-squares failed the estimation, while IPM method succeeds. The potential reasons for why LS fails are discussed in the later discussion section. Figure 3.12 shows the root mean squared deviation of the P_{mus} waveforms between the two methods. The optimization algorithm performances are summarized in Table 3.1. The IPM method with the quadratic P_{mus} parametric function estimates the lung mechanics and the respiratory muscle effort more accurate than other algorithms with an average percent error of all parameters 3.04%.

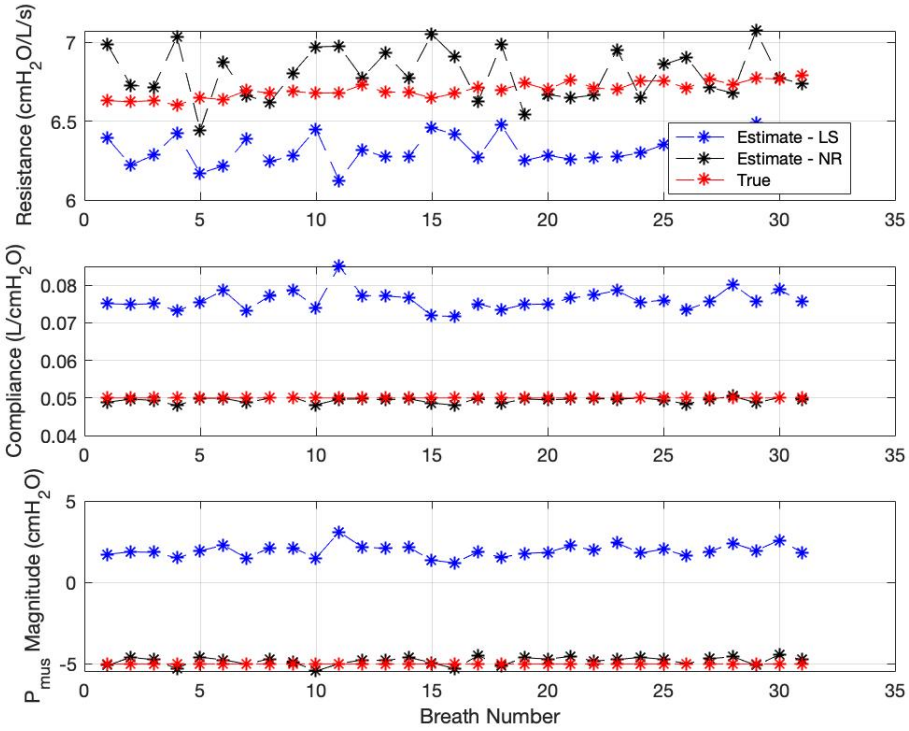

Figure 3. 10: The resistance, compliance and P_{mus} magnitude estimates using least-squares (blue), IPM with Newton-Raphson's method (black). The true parameter values are plotted in red. This estimation uses the quadratic P_{mus} parametric function (Figure 3.6B).

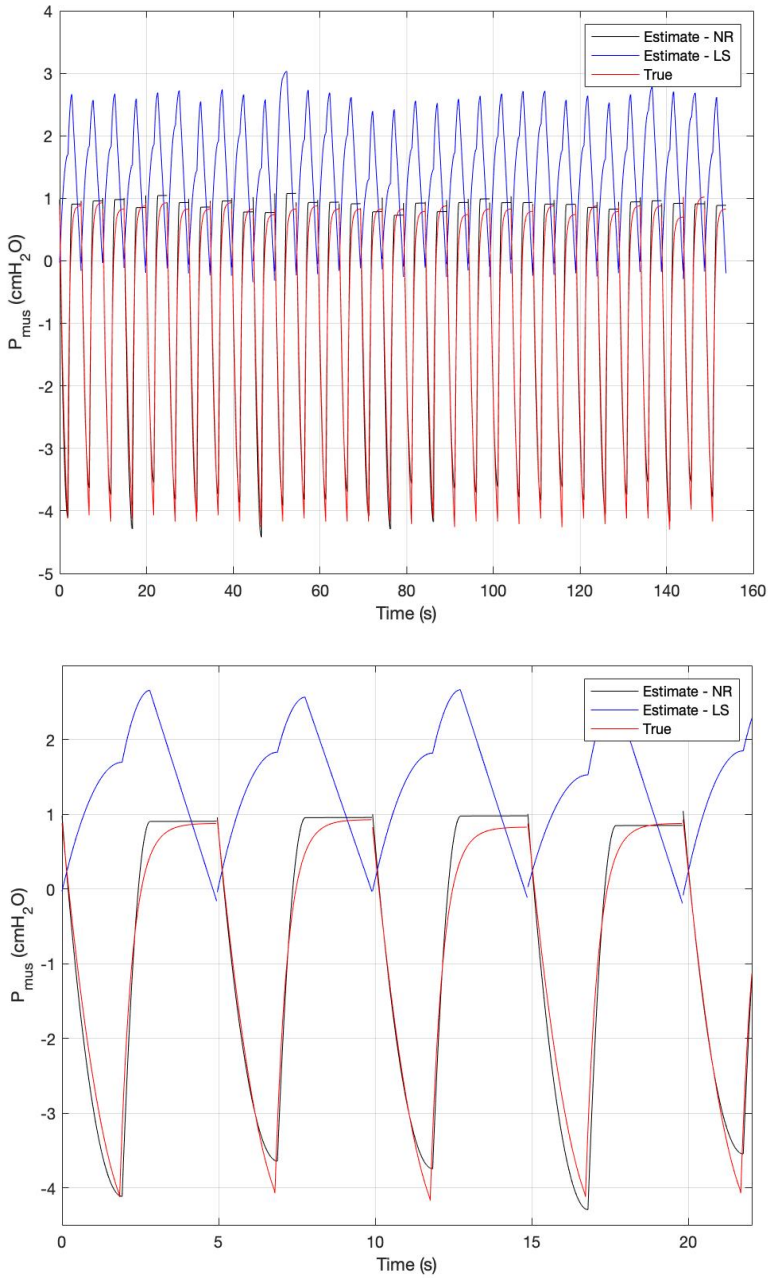

Figure 3. 11: The P_{mus} waveform estimated using least-squares (blue) and IPM with Newton-Raphson's method (black). The true P_{mus} waveform programmed in the motor is plotted in red. This estimation uses the quadratic P_{mus} parametric function (Figure 3.6B). A: all the estimation results. B: the first four estimation results.

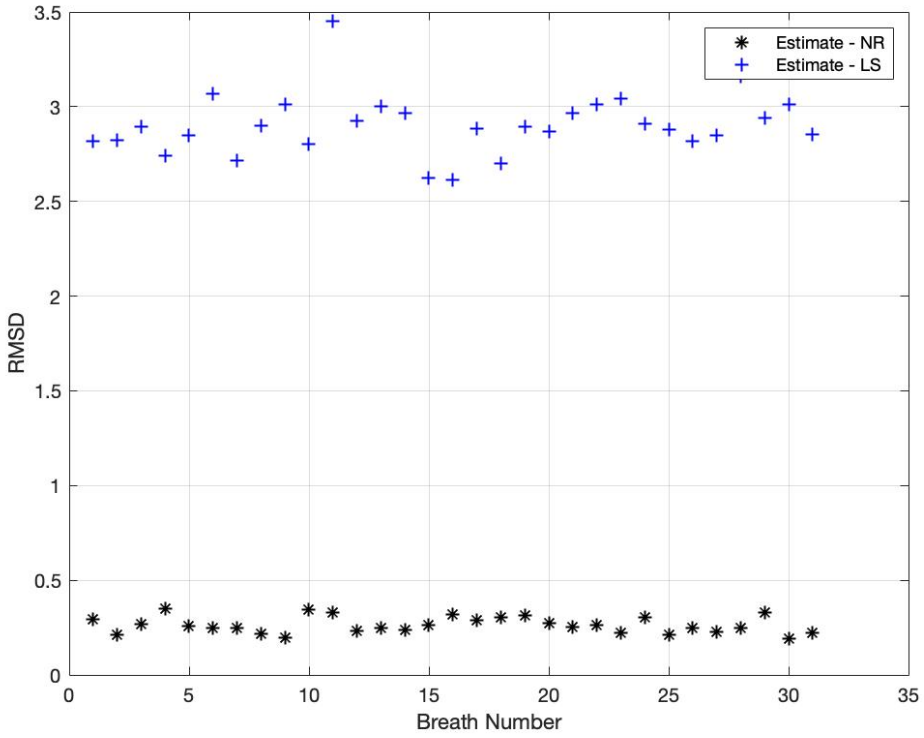

Figure 3. 12: Root mean squared deviation of the P_{mus} waveforms using IPM with Newton-Raphson's method (black) and least-squares (blue). This estimation uses the quadratic P_{mus} parametric function (Figure 3.6B).

Table 3. 1: Optimization Algorithm Performance Comparison Between Least-Squares and Interior Point Method with Newton-Raphson (IPM-NR)

Lung resistance (R_{rs})		
% error	P_{mus} (linear)	P_{mus} (quadratic)
Least-squares	19.99%	5.73%
IPM – NR	-	2.47%
Lung compliance (C_{rs})		
% error	P_{mus} (linear)	P_{mus} (quadratic)
Least-squares	1.43%	52.11%
IPM – NR	-	1.27%
P_{mus} magnitude		
% error	P_{mus} (linear)	P_{mus} (quadratic)
Least-squares	4.53%	138.9%
IPM – NR	-	5.38%

Figure 3.13 shows the cost (RSS) of the IPM optimization algorithm with different t_m and t_r pair variation. The best t_m, t_r pair that gives the optimal lung parameter estimate is determined by the minimal cost value. The minimal cost of the reported IPM algorithm in Table 3.1 corresponds to a time variation of 0.12 seconds as shown in Figure 3.13. Hence, a variation of 0.12 seconds in the positive direction from the initial approximation of the P_{ao} waveform is applied.

Figure 3.14 shows the disturbance analysis of the IPM algorithm. A zero-mean gaussian noise with changing variance has been introduced to the patient measurements, P_{ao} and Q. The percent errors of the estimates from the data with noise are plotted against the noise variances in Figure 3.14. The percent errors increase monotonically as the variance increases. This is expected, since the Gaussian noise with higher variance induces bigger estimation errors.

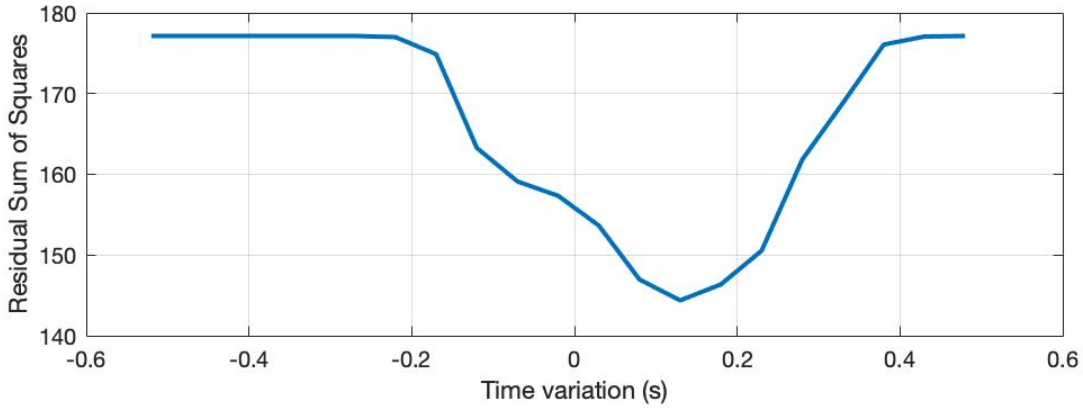

Figure 3. 13: Costs (RSS) vs time stamps (t_m, t_r) variation from -0.5 to 0.5 sec using IPM with Newton-Raphson method.

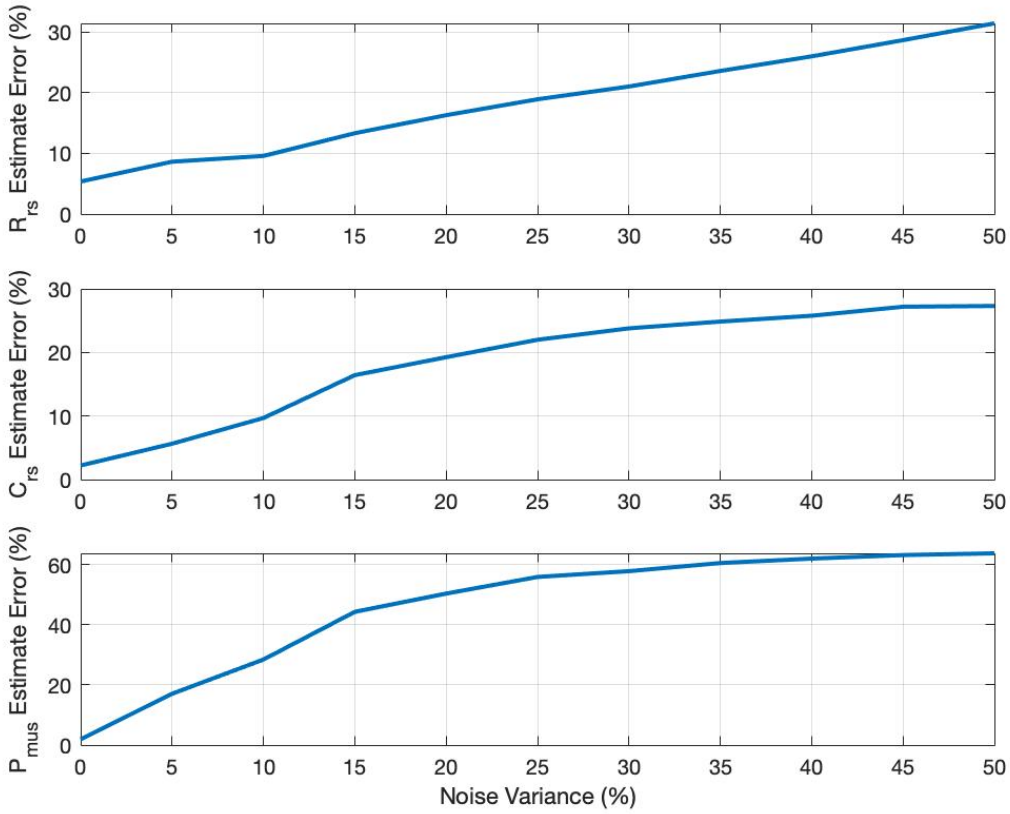

Figure 3. 14: IPM algorithm disturbance analysis. The percent errors of R_{rs}, C_{rs}, and P_{mus} magnitude are plotted against noise variance percent.

In order to find a confidence metric for our estimation, we sought to find the ranges of estimated parameters during one breath. We choose to quantify the confidence ranges of the estimates (akin to confidence intervals) by varying (increasing and decreasing) the measured signals by 20%, and then run the developed optimization algorithm. Take the flow measurement as an example, with a change of flow data from -20% to 20%, the estimates of lung resistances are found to be in the range [5.43, 8.15] $\mathrm{cmH_2O}/L/s$, lung compliances in the range [0.04, 0.06] $L/\mathrm{cmH_2O}$, and P_{mus} magnitudes in the range [-3.85, -5.78] $\mathrm{cmH_2O}$. All three ranges envelop the true parameter values, which gives more credence in the proposed algorithm.

3.4 Discussion

In this section, we discuss the potential reasons of why least-squares approach failed the quadratic parametric optimization. In order to answer this question, we analyze the second order derivative of the objective function, *i.e.*, Hessian matrix. The eigen analysis of the Hessian matrix provides good intuition of the shape of the search dimension. We also performed a principal component analysis (PCA) on the data matrix (*A* matrix) to compare the most important data signals under different *A* matrix structures, *i.e.*, in the linear and quadratic parametric optimization.

3.4.1 Eigen Analysis

The objective function (Equation 3.11) is twice continuously differentiable. We can compute the Hessian matrix of the objective function as follows:

$$H = \begin{bmatrix} 2Q^2(t) & 2Q(t)V(t) & 2Q(t) \\ 2Q(t)V(t) & 2V^2(t) & 2V(t) \\ 2Q(t) & 2V(t) & 2 \end{bmatrix}$$

The eigenvalues of the Hessian matrix are 0, 0, $V^2(t) + Q^2(t) + 1$. Note that the matrix H of the objective function J has non-negative eigenvalues, implying H is a positive-semidefinite matrix. Since H is the second derivative of the J with respect to unknowns and it is positive-semidefinite, the cost function is convex. However, the cost function is not strictly convex because the two eigenvalues are equal to 0. This implies that the corresponding eigenvectors span the plane of solutions with same minimum cost, in other words, the linear combinations of the corresponding eigenvectors do not contribute to cost reduction. Hence, different linear combinations of these two eigenvectors give rise to the infinitely many solutions of the estimation, and the optimal solution may not make physiological sense. However, in the IPM method, the physiological constraints are introduced in the optimization problem aiming to restrict the search dimension for the solution that we are after.

3.4.2 Principal Component Analysis

We performed a PCA analysis of the data matrix in the least-squares formulation, *i.e.*, the two *A* matrices in the quadratic (Equation 3.13) parametric optimization and in the linear (work from Vicario *et al.* [88]) parametric optimization. We compute the variances of the column data in *A* matrix in principal component space. For the linear parametric optimization, the data that has the highest variance in the principal component space is the volume waveform (V), while the data that has the highest variance in the principal component space is the flow waveform (Q) for the quadratic parametric optimization. Note that these two different algorithms use the same dataset, and the only difference is the way the *A* matrix is structured, since the structure of the *A* matrix depends on the parametric function. In the equation of motion, $P_{ao}(t) = \frac{1}{C_{rs}}V(t) + RQ(t) + \tilde{P}_{mus}(t)$, when the volume signal does not have the highest variance in the principal component space, $\tilde{P}_{mus}$ is estimated to increase during inspiration since the sum of $\frac{1}{C_{rs}}V$ and $\tilde{P}_{mus}$ can then match the shape of P_{ao} that also increases during inspiration. Note that the poor estimate of the P_{mus} waveform in the LS quadratic parametric optimization has a shape that is similar to the P_{ao} measurement, *i.e.*, the P_{mus} estimate increases during inspiration and decreases during expiration. On the other hand, when the volume is the principal component with the highest variance, like in the linear parametric optimization, $\tilde{P}_{mus}$ decreases during inspiration and increases during expiration, which agrees with the respiratory physiology.

3.4.3 Information Criterion

We also computed the Akaike Information Criterion (AIC) of the two parametric optimization algorithms, *i.e.*, the two models of the P_{mus} functions. AIC measures the trade-off between the goodness of fit of the model and the simplicity of the model. It also estimates the relative amount of information lost by a given model, *i.e.*, the less information a model loses, the higher the quality of that model. Thus, AIC provides a means for model selection that deals with both the risk of overfitting and the risk of underfitting. AIC is computed as $AIC = n\,log(\sigma^2) + 2K$, where $\sigma^2 = \frac{\sum(\epsilon_i)^2}{n}$, and the ϵ_i is the estimated residual from the fitted model, K is the total number of parameters in the model, including the intercept and σ^2. The AIC values for the linear parametric optimization and quadratic parametric optimization are -142.45 and -214.93 respectively. The smaller AIC value of the quadratic parametric optimization also supports that a quadratic formulation of P_{mus} waveform performs better in estimation.

3.5 Conclusion

In this work, we have developed a constrained nonlinear optimization algorithm to continuously monitor the respiratory mechanics (lung resistance and compliance), and the respiratory muscle effort (P_{mus}). This algorithm performs accurate estimation in spontaneous breathing patients with ventilator support. It is based on a physiological mathematical model of the lung mechanics, more specifically on a single-compartment first-order linear model that is widely accepted in the respiratory research community. This algorithm uses measurements that are routinely monitored at the patient bedside without additional instrumentation and interference of normal ventilation operation. Estimating resistance and compliance values can aid clinicians to differentiate between restrictive or obstructive diseases, monitor disease progression, and

optimally adjust ventilator settings to best meet patient's needs. In addition, estimating P_{mus} waveform can help to detect patient-ventilator dyssynchrony, avoid diaphragmatic fatigue and/or atrophy, and assess patient readiness to extubation. Comparing to the previous work, we include a more physiological quadratic P_{mus} function, *i.e.*, four pressure values to estimate versus two pressure values, and proved the estimation performance improvement. In future work, we will further validate the algorithm with animal or human data.

Chapter IV: Modeling of Transport Mechanisms in the Respiratory System: Validation via Congestive Heart Failure Patients

Circulation of blood in the body takes place in the pulmonary system. The pulmonary circulation carries deoxygenated blood away from the right ventricle, to the lungs for oxygen and carbon dioxide exchange, and return oxygenated blood to the left atrium and ventricle of the heart. For congestive heart failure patients, since the blood does not flow out the (left) heart normally due to congestion, fluid (plasma) backs up into the vessels in the pulmonary circulation. The accumulation of the fluid in the pulmonary circulation increases the microvascular hydraulic pressure. As a result, fluid could seep into the alveolar space (pulmonary edema) within minutes. This excess fluid induces extra stress during breathing that affects respiratory health. In this chapter, we focus on the effect that high pulmonary capillary pressure has on the development of this extravascular lung water (EVLW). A mathematical model of pulmonary fluid and mass transport mechanisms is developed in order to quantitatively analyze the transport phenomena in the pulmonary system. The proposed microvascular exchange module is validated on 15 male heart failure patients from published literature [91]. The model shows reasonable estimation of EVLW in heart failure patients, which is useful in assessing the severity of pulmonary edema.

4.1 Introduction

Pulmonary edema caused by increased capillary pressure is known as cardiogenic pulmonary edema. In congestive heart failure, the heart is not able to pump efficiently. This causes fluid from the heart to back up in the pulmonary vessels and increases the pulmonary capillary pressure. Figure 4.1 shows the circulation between the heart and the lungs. High pulmonary capillary pressure breaks the force balance across the capillary membrane (glycocalyx) and causes fluid to

leak into the alveolar interstitium. When the fluid seeping into the interstitium exceeds the fluid clearance by the lymphatic system, interstitial fluid builds. This interstitial edema then damages the epithelium and causes alveolar flooding. The total fluid outside the pulmonary capillaries (inside the interstitium and alveolar space) is termed extravascular lung water (EVLW). EVLW induces high stress during breathing, which can lead to life-threatening issues. In an effort to understand and explain the pulmonary edema of heart failure patients, we develop a mechanistic mathematical model of the human pulmonary microvascular exchange system (MVES).

In the following, we first describe our MVES model (basic physiology and modeling approach). Then, we present simulation results and compare them to Heijmans' model and clinical data of 15 heart failure patients. Finally, we conclude by summarizing the accomplishments, describing the limitations, and highlighting future extensions of this work.

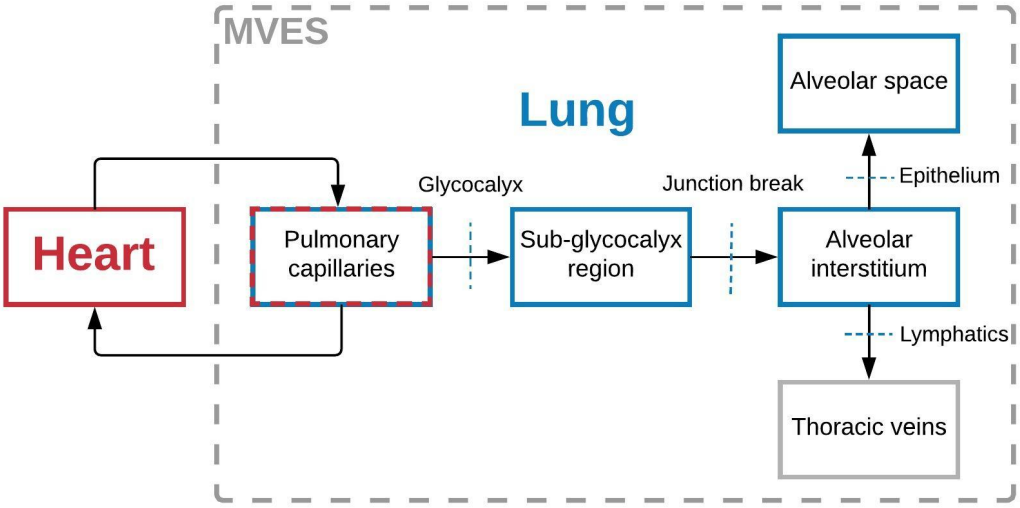

Figure 4. 1: Schematic block diagram of the heart-lung circulation and the microvascular exchange system (MVES).

4.2 Model Development

4.2.1 Literature Review

Many researchers have attempted to quantify fluid and mass transport in the MVES [92]–[94]. Heijmans *et al.*, in particular, developed an MVES model [95] to simulate edema development in the human pulmonary system. However, the model uses simple linear lymphatic and alveolar flows and the traditional Starling equation. Drake *et al.* developed a model of interstitial-lymphatic clearance using both a lymphatic pumping mechanism and a nonlinear lymphatic resistance [96]. However, their model includes few compartments and their parameters are for dogs, limiting the application in humans. Michel and Weinbaum have developed a revised form of the Starling equation [97], [98]. They claim that the Starling forces, which move fluid across the microvessels, are not determined by the hydraulic and osmotic pressure differences across the endothelium. Instead, the forces are determined by pressure differences across the endothelial glycocalyx, a complex fiber matrix covering the endothelial cells. It is now well accepted that the glycocalyx serves as the primary molecular sieve for fluid and mass transport. More recently, several studies and simulation models of the endothelial glycocalyx have supported the revised Starling hypothesis and equation [99], [100]. Our human MVES model is the first to include nonlinear lymphatics, a revised Starling equation with a lumped sub-glycocalyx region, and endothelial glycocalyx filtration regulation.

4.2.2 Physiology

Figure 4.1 also shows a simplified microvascular fluid and mass exchange diagram. The fluid and mass transports discussed herein occur transversally across a capillary (microvessel), which is around 0.2 micron thin in humans [101]. Fluid and mass move from the pulmonary capillaries into

the alveolar interstitium through the sub-glycocalyx region. From the interstitium, fluid can move into the thoracic veins through the lymphatic vessels and/or into the alveolar space (lungs) through the epithelium. In healthy scenarios, very little fluid enters the alveolar space.

Figure 4.2 shows the schematics of the pulmonary blood circulation. In Figure 4.2, the blood stream is noted as a red arrow, and the water and solute flow is noted as a blue arrow. The main blood stream at the pulmonary microvessels flows into the pulmonary veins, and returns to the heart. However, some water can transport across the pulmonary endothelium due to the hydraulic pressure gradient and the osmotic pressure gradient at the pulmonary microvessels and the interstitium, or a leaky (sick) interface. Some solutes (*e.g.*, albumin and globulin) flow crosses endothelium due to diffusion and advection effects. Figure 4.2 A shows a macroscopic view of fluid and mass transport in the pulmonary system, and Figure 4.2 B shows a microscopic view of fluid and mass transport, where endothelium is sub-divided into the glycocalyx layer and the junction strand, where the junction strand includes sub-glycocalyx region with junction breaks. Detailed descriptions of important MVES compartments that differentiate our model follow.

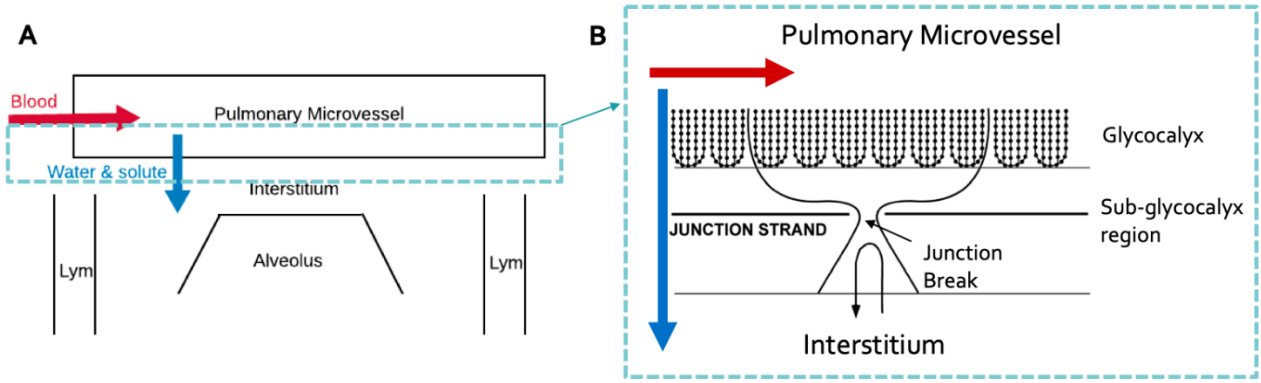

Figure 4. 2: Pulmonary Blood Circulation Schematics. A: blood circulation in the pulmonary system from the pulmonary microvessels to the interstium, the alveolar space, and the lymphatic system B: water and solute transport across endothelium in more details (glycocalyx, sub-glycocalyx region, junction strand, junction break, and interstitium).

4.2.2.1 The Glycocalyx

The endothelial cells in the microvessels are coated with the glycocalyx layer, which is a fuzzy and filamentous coat that comprises sulfated proteoglycan, hyaluronan, glycoproteins, and plasma proteins [102]. Glycocalyx is also a highly charged layer of membrane-bound biological macromolecules. Due to its complex structure, glycocalyx passively limits fluid and mass flow and actively regulates the endothelial permeability via mechanotransduction. The glycocalyx layer serves as a mediator for cell-cell interactions and protects a cell membrane from the direct action of physical forces and stresses allowing the membrane to maintain its integrity. When the glycocalyx senses the fluid stress in the vessel, its integrity is altered via released nitric oxide and reactive oxygen species. Dull found that during increased pulmonary microvascular pressure, endothelial filtration coefficient increases significantly [103].

4.2.2.2 The Sub-glycocalyx Region

Between the glycocalyx layer and the junction break is a 'protected region' known as the sub-glycocalyx region [102]. Since the glycocalyx layer strictly selects the mass flow crossing the microvessels, the protein concentration difference between the microvessels and the sub-glycocalyx region is great. Therefore, sub-glycocalyx osmotic pressure, π_{sg}, replaces interstitial osmotic pressure, π_{int}, in the revised Starling equation [97], [98].

4.2.2.3 The Junction Break

The endothelial cells of the pulmonary capillaries form as a tight junction strand with few breaks, resulting in very small pathways for fluid and mass to traverse. The pathways are known as the junction break.

4.2.2.4 The Lymphatic System

The primary function of the pulmonary lymphatic system is to maintain interstitial fluid balance. The lymphatic system returns excess interstitial fluid to the blood circulation via the thoracic duct. It plays an important role in homeostasis by controlling interstitial fluid volume. The interstitial hydraulic pressure is lower than the thoracic vein pressure. To pump lymphatic fluid against this pressure gradient (lymph propulsion), lymphangion smooth muscles rhythmically contract. Drake proposed a pumping pressure be added in modeling lymphatic flow. He also found that an increase in interstitial fluid volume causes the lymph vessels to dilate, thus decreasing their resistance [96].

4.2.3 Modeling

The microvessels, the sub-glycocalyx region, and the interstitium are three model compartments connected in series (Figure 4.1). The glycocalyx is a first membrane (filter) between the microvessels and the sub-glycocalyx, and the junction break is a second filter between the sub-glycocalyx and the interstitium. Connected in parallel to the interstitium, the lymphatic vessels and the alveolar epithelium filter the fluid and mass passing through them. Two proteins, albumin and globulin, are modeled as they are the most common plasma proteins and affect osmotic pressure most.

To model the complex MVES, we use the linear graph approach [38]. This approach can describe a complex dynamic system graphically via simple energy storage and dissipative elements. Figure 4.3 describes four transport mechanisms for both water and protein in the pulmonary microvascular system. Every node (filled circle) represents a physical compartment and is labeled

with a variable, pressure or concentration, depending on the transport mechanism. Every line with an arrow represents a flow and is labeled with a parameter like a resistance or a capacitance.

The oblong ellipses are transducers, and they represent the transport mechanisms' effects on one another. The red lines represent hydraulic transport, yellow osmosis, purple diffusion, and green advection. The hollow circles represent sources and the shaded lines represent reference variables. The direction of the arrows on the lines is picked by convention but the true direction is determined by the net fluid (or mass) flow at any time instant. For example, the protein concentration at the interstitium is determined by equating the mass flows entering to the mass flows leaving and mass being stored at that location. Mass flows entering are from the sub-glycocalyx region by two mechanisms, mass flows leaving are to the thoracic veins and/or alveolar space by advection, and mass stored is due to the capacitance (dashed line denoted V_{int}) of the interstitium. This is seen in Figure 4.3 by the green and purple lines connected to $\mathcal{C}_{int}$. The pumping pressure, P_p, which is a function of P_{int}, is the added source into the lymphatic vessels (+ sign).

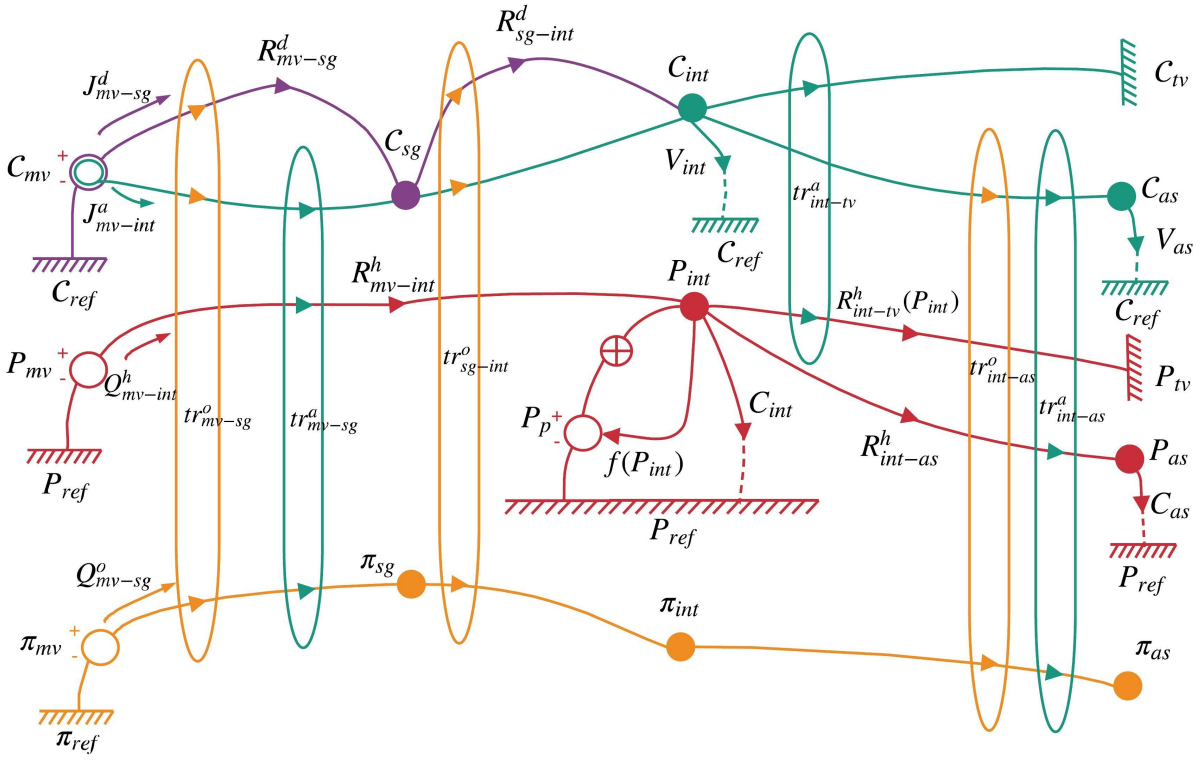

Figure 4. 3: Microvascular exchange system linear graph. Red color represents hydraulic, yellow represents osmotic, purple represents diffusive, and green represents advective mechanisms. P, hydraulic pressure; π, osmotic pressure; $\mathcal{C}$, protein concentration; Q^h, hydraulic fluid flow; Q^o, osmotic fluid flow; J^a, advective mass flow; J^d, diffusive mass flow; R^h, hydraulic resistance; R^d, diffusive resistance; V, fluid volume; C, fluid capacitance; tr^o, osmotic transducer; tr^a, advective transducer; mv, microvessel; sg, sub-glycocalyx region; int, interstitium; tv, thoracic vein; as, alveolar space; lym, lymphatics; ref, reference; glx, glycocalyx; $jcnbrk$, junction break; epi, epithelium; $endo$, endothelium; ref, reference; P_p, pumping pressure.

4.2.3.1 Equations

From the linear graph, we can write the dynamic equations to solve for the variables in time at each node. The equations are derived from the laws of conservation of mass. Typically, the conservation equations give rise to differential equations while transducers generate (linear or nonlinear) algebraic equations. As an example, to solve for the fluid flow from the microvessels to the interstitium via hydraulic and osmotic mechanisms, we can derive the following:

$$\frac{dP_{int}}{dt} = \frac{1}{C_{int}} \cdot (Q_{mv-int} - Q_{int-tv} - Q_{int-as}) \tag{4.1}$$

$$Q^{h}_{mv-int} = \frac{1}{R^{h}_{endo}} \cdot (P_{mv} - P_{int}) \tag{4.2}$$

$$Q^{o}_{mv-sg} = Q^{o}_{sg-int} = -\frac{1}{R^{h}_{endo}} \cdot \sigma_{glx} \cdot (\pi_{mv} - \pi_{sg}) \tag{4.3}$$

$$Q_{mv-int} = Q^{h}_{mv-int} + Q^{o}_{sg-int} = \frac{1}{R^{h}_{endo}} \cdot [(P_{mv} - P_{int}) - \sigma_{glx} \cdot (\pi_{mv} - \pi_{sg}) \tag{4.4}$$

Equations (4.1-4.4) are derived from the linear graph in Fig. 2. Note that Equation (4.4) is in fact the same as the revised Starling equation proposed by Michel and Weinbaum [97], [98]. The model has 34 equations and 34 unknown variables.

4.2.3.2 Parameter Assignment

Parameters, the coefficients multiplying the variables in the preceding equations, typically, represent material property and geometry. The model has a total of 14 parameters that are determined from curves in animal experiments or previously published studies. Table 4.1 shows examples of four parameters for the healthy human. The endothelial filtration coefficient, K_{endo}, is derived from the steady-state flow for a healthy human, where Bert and Pinder used 1.12 ml/hr/mmHg for K_{endo} [94], while Dull measured 6.6 ml/hr/mmHg per 100 g predicted lung weight from 116 rat experiments [103]. The interstitial capacitance, C_{int}, is assumed as in [94]. The glycocalyx reflection coefficient, σ_{glx}, was adopted from Adamson [99]. The permeability coefficient of albumin at the glycocalyx layer, PS^{alb}_{glx}, is solved via steady-state mass balance as 1.2 ml/hr, while it is estimated as 3 ml/hr for the entire endothelium [94].

Table 4. 1: Parameter Values for a Healthy Human

Parameters	Definition	Value
K_{endo} (ml/hr/mmHg)	Filtration coefficient of the endothelium	7.64
C_{int} (ml/mmHg)	Interstitial capacity	4.4 [94]
σ_{glx}	Reflection coefficient of the glycocalyx	0.94 [99]
PS_{glx}^{alb}(ml/hr)	Permeability coefficient of albumin at the glycocalyx	1.2

4.3 Results

4.3.1 Simulation and Validation for Healthy Subjects

Table 4.2 holds the normal steady-state values of critical variables for a healthy human. As shown in Table 4.2, the proposed model's steady-state outputs stay within the range of values published in the literature (*e.g.*, V_{int}, Q_{int-tv}) or in agreement with the outputs of a published model (*e.g.*, P_{int}, Q_{mv-int}, $C_{int}^{glo}/C_{mv}^{glo}$,and $C_{int}^{alb}/C_{mv}^{alb}$). The interstitial pressure has not been directly measured for human lungs, but the value from our model closely matches that of Heijmans' model [93], [95]. The interstitial fluid volume, as predicted by simulation, is in very good agreement with values reported by Staub [104]. To solve for the pulmonary lymphatic flow, P_p is assumed to be 39 mmHg for normal pulmonary lymphatics. This value is measured at the arms' lymphatics of 16 normal subjects [105]. Similar to Drake, we consider P_p (lymphatic pump pressure source) as a linear function of interstitial hydraulic pressure, P_{int}, and consider the lymphatic resistance as a nonlinear function of the interstitial fluid volume, V_{int} [96]. In steady-state, the flow going from the microvessels to the interstitium should equal the lymphatic flow to maintain fluid balance. As expected, via simulation, the fluid flow from the microvessels to the interstitium, Q_{mv-int}, indeed equals the fluid flow from the interstitium to the thoracic veins,

Q_{int-tv}. Due to the limited physical space of the sub-glycocalyx region, our assumption of no fluid or mass storage capacity for the sub-glycocalyx region to be also justified by Equation 4.4. Therefore, the protein concentration of the fluid in the sub-glycocalyx region (C_{sg}^{pro}) equals the protein concentration of the fluid that flows across the glycocalyx layer. From the literature, no C_{sg}^{pro} values were found. The albumin and globulin concentration ratios between the microvascular plasma and the interstitial fluid are reported in Table 4.2 and are in good agreement with the values reported by Yoffey [106].

Table 4. 2: Steady-state Simulation Variable Values for a Healthy Human

Variables (Human)	**Simulation Value (Proposed Model)**	**Simulation Value (Heijmans [93])**	**Experimental Value/Range from Literature**
P_{int} (mmHg)	-3.02	-3.3	-
V_{int} (ml)	378.75	378.4	383 [104] 274 [107] range: 331-406
Q_{mv-int} (ml/hr)	8.81	8.8	-
Q_{int-tv} (ml/hr)	8.81	8.92	range: 10-20 [104] range: 5-10 [108]
C_{sg}^{pro} (g/ml)	0.036	-	-
$C_{int}^{glo}/C_{mv}^{glo}$	0.49	0.4	0.55 [106]
$C_{int}^{alb}/C_{mv}^{alb}$	0.63	0.6	0.8 [106]

4.3.2 Simulation and Validation for Heart Failure Patients

Figure 4.4 shows a heart failure simulation induced by setting the pulmonary microvascular pressure to 25 mmHg, which is a typical high value for heart failure patients. Fluid volumes of the interstitium V_{int} and the alveolar space V_{as} are plotted in time under healthy and diseased scenarios. The disease condition followed the Dull study [103] where at P_{mv} of 25 mmHg the endothelial filtration coefficient (K_{endo}) increased 5 fold. Due to the drastic increase in both hydraulic pressure

and filtration coefficient, the interstitial fluid volume increases immediately. As Miff, Prichard, and Staub suggest, alveolar flooding happens when V_{int} reaches approximately 450 – 600 ml [104], [109], [110]. Heijmans [93] suggested the onset of alveolar flooding occurs at an interstitial fluid volume of 460 ml. When V_{int} reaches 460 ml, alveolar edema develops. Rimoldi [111] claimed that acute decompensated heart failure patients can develop flash pulmonary edema, *i.e.* within minutes. Our model, indeed, shows that in about 7 minutes the interstitial fluid starts to seep into the alveolar space (after V_{int} exceeds 460 ml). Heijmans, on the other hand, reported the onset of alveolar flooding as more than 5 hours and at an even higher pressure (P_{mv} = 35 mmHg). Their reported time to development of alveolar edema, hence, may be too long for heart failure. There is little clinical data in the literature on human interstitial and alveolar edema development in time.

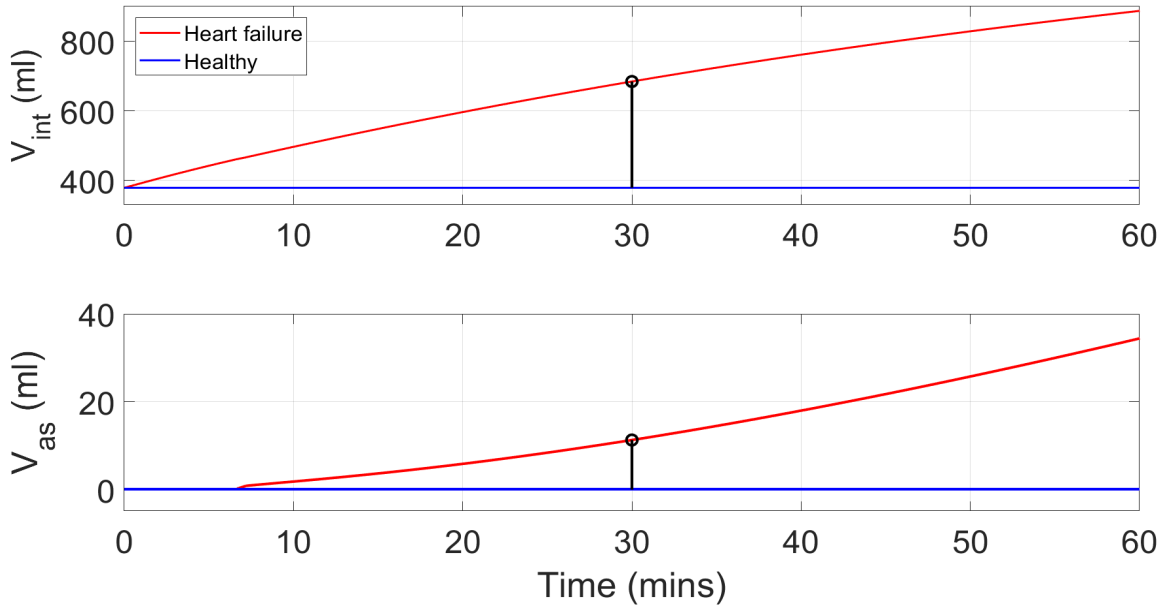

Figure 4. 4: Congestive heart failure dynamic simulation with P_{mv} = 25 mmHg. Model outputs V_{int}, V_{as} for heart failure and healthy human

Figure 4.5 shows simulation results of fluid accumulation in the interstitium and lungs (EVLW) in red with P_{mv} varying from 12 to 32 mmHg and for durations of 0.5 hours to 10 days or more. We compare our results to experimental invasive EVLW measurements by Grover *et al.* [91]

containing 7 chronic heart failure (HF) patients (blue) and 8 acute HF patients (cyan), as well as to Heijmans' [93] simulation model (magenta). The 0.5 hour to 1 day simulation results best matched Grover's acute HF patients, while the 10 days or more results best matched the chronic HF patients. Grover reported capillary pressure to be 23.2 ± 3.6 mmHg for the chronic HF group and 25.8 ± 8.1 mmHg for the acute HF group, after a duration of symptoms (difficulty breathing) of 28 ± 14 hours and 9 ± 4 hours, respectively.

In the chronic group, EVLW was measured to be in the range of 13.12 to 24.75 ml/kg, while Heijmans simulates EVLW to be roughly 5.89 to 6.28 ml/kg for a P_{mv} range of 23.2 ± 3.6 mmHg. Their value underestimates EVLW for HF patients as compared to Grover. For the same P_{mv} range, our model predicts an EVLW range between 11.25 to 35.84 ml/kg (10 day, red), a closer adherence to the clinical measurements of chronic HF patients (blue) than [93]. Similarly, for the acute HF patient group, our model's acute HF EVLW estimates (5.93 to 14.33 ml/kg) cover the range of experimental results more closely than [93]. Further, just as the experimental values show lower EVLW for acute patients than for chronic patients, so do our simulation results. Hence, knowing the HF patient's symptom duration and capillary pressure, our model can provide reasonable estimation of EVLW non-invasively.

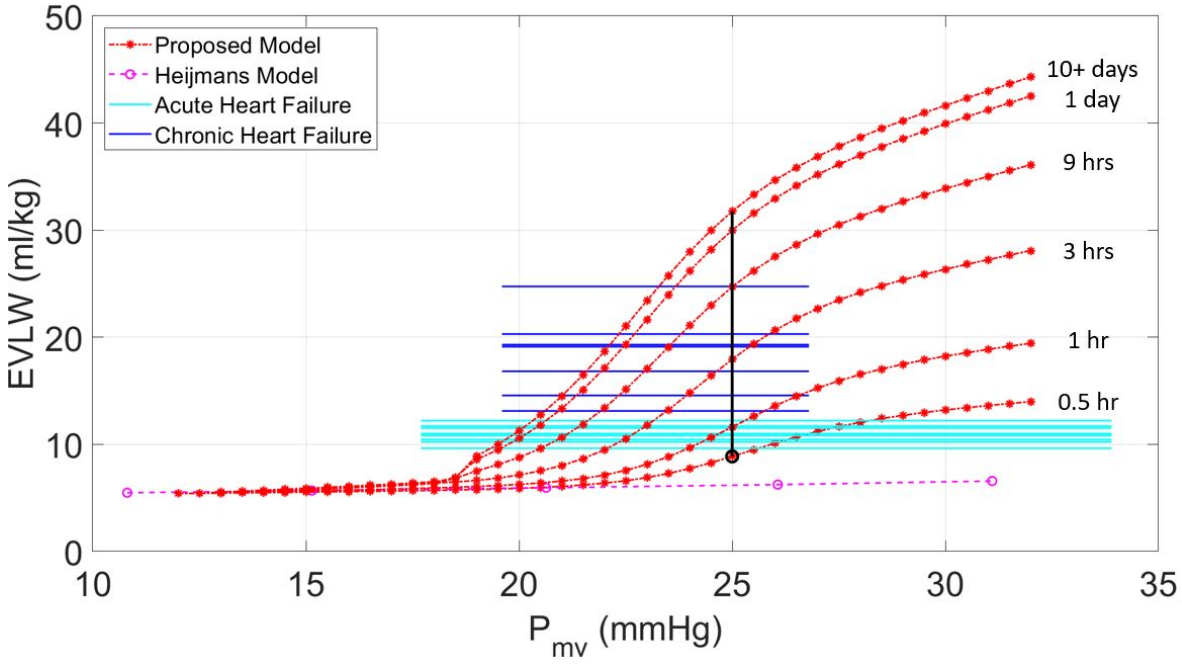

Figure 4. 5: EVLW accumulation at different pulmonary capillary pressures

Figure 4.5 shows pulmonary blood capillary pressure (x-axis) and extravascular fluid volume (y-axis). The red lines show fluid accumulation at different P_{mv} values. From bottom to top, a black stem line shows fluid accumulation in time at a sustained P_{mv} value. As an example, at half an hour after insult (P_{mv} = 25 mmHg, 70 kg person, shown as black dot) EVLW is 8.87 ml/kg. This volume indeed equals the sum of the volumes corresponding to the two black dots in Figure 4.4.

4.3.3 Sensitivity Analysis

To evaluate the effects of model parameters (filtration coefficients, reflection coefficients, osmotic reflection coefficients and permeability coefficients) on the MVES variables (hydraulic pressure and the volume of the interstitial space, fluid flow, protein concentration, etc.), we performed a sensitivity analysis of the MVES variables to changes in parameters via sigma (Σ) values, as shown in Table 4.3. Sigma values were computed to quantify the sensitivity, as

$\frac{\Delta Variable \times Parameter}{\Delta Parameter \times Variable}$. The sigma value is a measure of the effect of the change in parameters to changes in variables, where parameters represent material property and geometry of the system (first column of Table 4.3), while variables are the system outputs (first row of Table 4.3). A bigger Σ value indicates a higher sensitivity. Each sigma value is computed using a change in a parameter and corresponding changes in variables. For comparison purposes, we have selected a common range of parameter change in Table 4.3 (50% decrease to a 100% increase in 10% increments). The range -50% to 100% corresponds to halving and doubling each parameter, thereby covering a reasonable range to study negative and positive changes of the nominal value. A mean sigma was then generated for each parameter (across all variables) and reported in the cells of Table 4.3.

Table 4. 3: Sensitivity Results

Σ	P_{int}	V_{int}	V_{as}	Q_{mi}	Q_{il}	C_{int}^{pro}	C_{sg}^{pro}	C_{as}^{pro}	**Mean**
K_{endo}	0.2466	0.0126	0	0.1011	0.1012	0.0341	0.0198	0	0.0644
σ_{endo}^{alb}	1.7948	0.0885	0.0185	0.6641	0.6641	0.3341	0.5175	0.0478	0.5162
σ_{endo}^{glo}	2.1046	0.0828	0.0185	0.5742	0.5741	0.4817	0.4155	0.0467	0.5373
σ_{glx}	2.2334	0.1621	0.185	1.4096	1.4096	0.4229	0.2421	0.9392	0.8755
PS_{glx}^{alb}	0.6048	0.0245	0	0.1411	0.1411	0.0479	0.0798	0	0.1299
PS_{glx}^{glo}	0.2217	0.0123	0	0.0738	0.0738	0.0412	0.0416	0	0.0581

Table 4.3 quantifies the sensitivity of the MVES variables to parameter change.

As seen in Table 4.3, the MVES variables (fluid pressures, fluid flows, protein concentrations) are very sensitive to the glycocalyx reflection coefficient (σ_{glx}). This is expected, since the glycocalyx layer serves as the main sieve for the fluid and mass transport due to its complex

structure. In addition, reflection coefficient represents the restrictive effect of a pathway to the protein mass flow. The osmotic pressure demined by the reflection coefficient is one of the two pressure potentials (hydraulic and osmotic pressures) that drives the fluid flow. Hence, the reflection coefficients are expected to play an important role. Also, since the protein molecule size is much larger than the water molecule, when the pathway is wide enough to pass a protein, water molecules supposed to pass easily as well. Therefore, the hydraulic pressure is highly sensitive to the glycocalyx reflection coefficient. Among all the parameters, the MVES variables are more sensitive to the mass flow coefficients, *i.e.*, endothelial reflection coefficients for albumin and globulin, osmotic reflection coefficient of the glycocalyx layer, and the permeability coefficients of albumin and globulin at the glycocalyx layer). This is expected with the similar reasons as mentioned above, *i.e.*, 1) osmotic pressure gradient is greatly affected by the protein mass flow, and 2) water molecules are much smaller than protein molecules, thus fluid flow is sensitive to the mass flow coefficients. As expected, the change of the reflection coefficients greatly affects the MVES variables, especially for the interstitial pressure and the fluid flow. Note that in this sensitivity analysis, each parameter is changed individually without affecting the other parameters. In real patients, as the membrane gets more permeable, all the parameters that relate to the filtration of fluid and mass flow will alter at the same time, *i.e.*, the filtration coefficients, the reflection coefficients, and the permeability coefficients.

4.3.4 Model Stability and Robustness Assessment

To assess the stability and robustness of the proposed model, we generate phase plane plots for unperturbed and perturbed long-time simulations, and assess feasible parameter ranges. For numerical stability we have simulated the model for more than 4000 breaths (300+ simulation

hours) on a 2.9GHz 8GB machine and plotted the interstitial volume vs interstitial pressure for healthy subject and heart failure patients as shown in Figure 4.6 upper and lower panels, respectively. The interstitial volume and pressure, two important variables that dictate the lymphatic pumping pressure, determine the interstitial fluid balance. We plot these two variables (interstitial volume vs interstitial pressure) against each other for both healthy (unperturbed) and diseased (perturbed) cases. Both variables reach steady state and have negligible variations that are caused by the pulsatile pulmonary capillary pressure input. As shown in Figure 4.6 upper panel (unperturbed case), the interstitial pressure oscillates around -3.02 mmHg, and the interstitial volume oscillates around 378.75 ml, which are in agreement with the reported values in the literature [93] [104] [107]. In the perturbed case, (Figure 4.6 lower panel), both the interstitial pressure and volume increase as expected due to the increase in porosity of the endothelium for a heart failure condition. The system outputs (interstitial volume vs interstitial pressure) are closed, indicating a well-behaved system under both healthy and diseased cases. Through these analyses, system stability is maintained when multiplicative factors perturbing the parameters (representing lung diseases) are bound by the following limits: $K \geq 0$, PS ≥ 0, $0 \leq \sigma \leq 1$, and $C_{int} > 0$. Note that physiological systems typically have positive-only parameters, since negative parameter values do not have physical meaning.

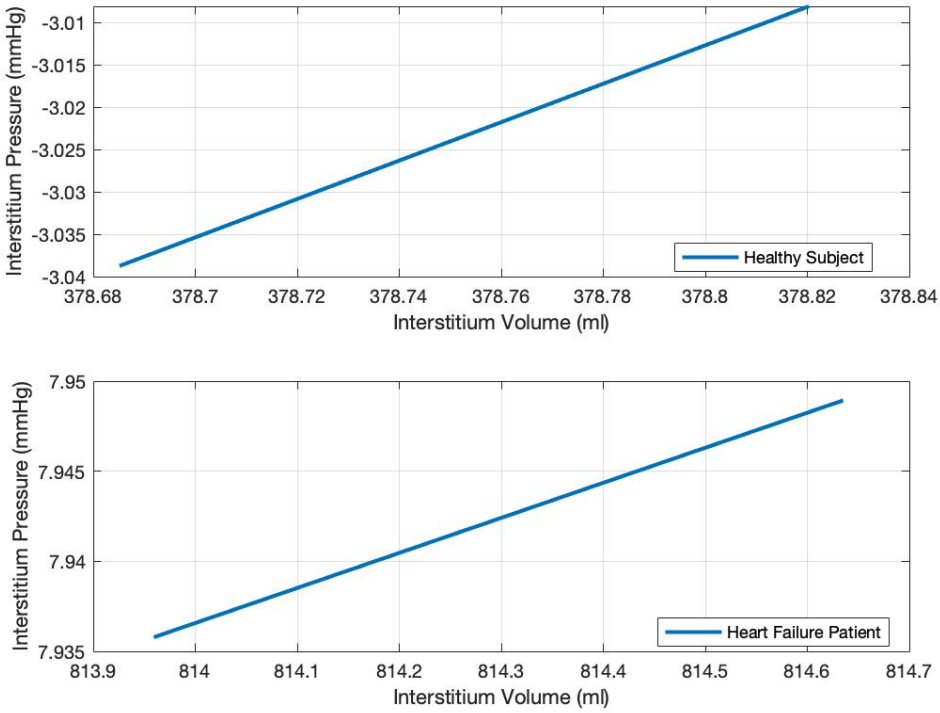

Figure 4. 6: Interstitium volume vs interstitium pressure for long-time breathing simulation in healthy subject (upper panel) and heart failure patients (lower panel).

4.4 Conclusion

In this chapter, we demonstrated via simulation studies that a mathematical microvascular exchange system (MVES) model, which has 1) a nonlinear lymphatic system, 2) a revised Starling equation including a lumped sub-glycocalyx region, and 3) endothelial glycocalyx filtration regulation via mechanotransduction, shows reasonable extravascular lung water (EVLW) estimation when compared to published clinical data. Such a model can be used to aid in clinical diagnostic or therapeutic decisions for heart failure patients. Prediction of the onset of edema or the amount of edema fluid in time could be used to better indicate when to move to a more invasive or costly diagnostic tests or when to administer therapies such as diuretics (to remove the excess

fluid). In future work, we will expand our model to include sodium-potassium pump, additional ions, and more accurate fluid alveolar compliance and pulmonary lymphatic pumping pressure values. Further exploration into the change in the tissue properties of acute and chronic heart failure patients is needed to better understand and simulate lung edema development.

Chapter V: Integrative Pulmonary Model with Lung Gas Exchange System and Pulmonary Blood Circulation

The main function of the lungs is to provide freshly breathed oxygen (O_2) to the blood capillaries, while taking carbon dioxide (CO_2) in exchange from them and expelling it to the atmosphere. The oxygenated blood can thus be delivered to all parts of the body so that organs maintain functional. In this chapter, we introduce 1) the pulmonary gas exchange system that describes the oxygen (O_2) and carbon dioxide (CO_2) transport between the pulmonary capillaries and the alveolar space, and 2) the pulmonary blood circulation module that describes blood transport from the heart to the pulmonary system. Linking these two lung modules (the pulmonary gas exchange system and the pulmonary blood circulation) to the other four lung modules introduced in the previous chapters, namely, the lung mechanics, the alveolus elasticity, the respiratory muscles and rib cage mechanics, and the microvascular exchange modules, we then have an integrative dynamic pulmonary system that quantitatively describes human breathing mechanism. Each subsystem was developed based on the latest knowledge of lung physiology and was validated using either patient data or other accepted physiology-based models. To our knowledge, the combined six-module model could be one of the most rigorous lung dynamic model in the literature. In this chapter, we simulate and validate this integrative lung model against three data sources: 1) blood gas content of healthy patients, 2) the ARDS patient of Chapter I, and 3) the quadriplegic patients who breathe via isolated phrenic paced diaphragm in Chapter II. This integrative lung model helps to better understand the lung normo- and patho-physiology. It can determine and forecast the state of breathing mechanisms under healthy and diseased conditions. Different therapeutic scenarios could now be tested on the proposed dynamic respiratory model so

that the optimal therapy can be found for patients. In addition, system identification techniques can be applied to this, or part of this, model to achieve personalized medicine.

5.1 Introduction

In this work, we complete the human respiratory model by linking the lung gas exchange system and the pulmonary blood circulation to the four respiratory modules described in previous chapters, namely, the lung mechanics, the alveolus elasticity, the respiratory muscles and rib cage mechanics, and the microvascular exchange modules. The gas exchange system describes the oxygen (O_2) and carbon dioxide (CO_2) transport between the pulmonary capillaries and the alveolar space, and the pulmonary blood circulation module describes blood transport from the heart to the pulmonary system. Both the gas exchange and the blood circulation systems are largely based on the work of Ursino *et al.* [112], [113], and Albanese *et al.* [3],[8].

Albanese *et al.* [3],[8] developed a dynamic cardio-pulmonary (CP) model based on the work of Ursino *et al.* [112], [113] that includes cardiovascular circulation, respiratory mechanics, tissue and alveolar gas exchange, as well as neural control. Karamolegkos *et al.* [2] improved the cardiac section of the CP model by focusing on the heart-lung interaction phenomena, while the pulmonary system remains simplistic. This dissertation contributes a more rigorous human pulmonary system in order to 1) better understand the lung normo- and patho-physiology, and 2) achieve personalized medicine when system identification techniques are applied to this, or part of this, model.

This model mathematically articulates the pulmonary physiology as follows. During quiet breathing (non-ventilated patients), the nerve that originates in the neck (C3–C5) sends electric signals to activate the diaphragmatic and intercostal muscles. The contraction of respiratory muscles expands the thoracic cavity, generating a negative hydraulic pressure in the pleural cavity.

In the respiratory muscles and rib cage mechanics module (Chapter II), the pleural cavity pressure (module output) is computed from the respiratory muscle activity (module input). The pleural cavity pressure is a negative pressure that generates a pulling force to expand the lungs and to reduce the alveolar pressure. In the lung mechanics module (Chapter I), the change of lung volume and the lung pressure (module outputs) during normal breathing are computed as the pleural cavity pressure (module input) changes. As the alveolar volume increases during inspiration, the alveolar pressure drops. The air thus flows into the alveoli following the pressure gradient through mouth/nose, larynx, trachea and bronchi. The trachea and bronchi are airway tubes that divide repeatedly into tubes of smaller and smaller diameters. One of the other main determinants of the lung volume expansion is the alveolar compliance that is determined by two factors: 1) the lung fibers (elastin and collagen) elasticity as quantified by the fiber volume and fiber quality (stress-strain relation), and 2) the pulmonary surfactant concentration. The surfactant is a mixture of lipids and proteins that line the inside of the alveoli, forming a film that reduces surface tension to keep alveoli open. The alveolus elasticity module (Chapter II) computes the time-varying alveolar compliance value (module output) as a function of lung fiber elasticity and the surfactant concentration (module inputs). In the lung mechanics module (Chapter I), lung pressures and volumes are computed using the time-varying alveolar compliance as an input. A normal surfactant concentration is maintained by a healthy pulmonary microvascular exchange system (Chapter IV). This system simulates the water and protein (albumin and globulin) transport between the pulmonary capillaries and the alveolar space. The water transport depends on the hydraulic pressure gradient and osmotic pressure gradient, and the protein transport depends on the diffusive and advective effects across the endothelium and epithelium. During a diseased situation, water in the pulmonary capillaries seeps into the alveolar space due to abnormal capillary pressure and/or

leaky endothelium or epithelium (permeability coefficients become high). The water accumulated in the lungs reduces the pulmonary surfactant concentration, which increases surface tension that could collapse the alveoli [12]. The water in the lungs thus serves as an input to the alveolus elasticity module for determining the surfactant concentration. The pulmonary blood circulation simulates the blood transport from the right ventricle to the left atrium, passing pulmonary arteries, capillaries, and veins. The blood pressures and volumes at these locations are computed in time as the heart pumps, and the heart rate is also determined by the neural system. Finally, the pulmonary gas exchange system computes blood gas contents (module outputs), such as PaO_2, $PaCO_2$, etc., based on the blood in the pulmonary capillaries and the gas in the alveolar space (module inputs). The blood gas contents are computed as results of oxygen (O_2) and carbon dioxide (CO_2) transport between the pulmonary capillaries and the alveolar space described in the gas exchange system.

In this chapter, we introduce and link the lung gas exchange module and the pulmonary blood circulation module to the four modules that are described in the previous chapters (lung mechanics, alveolus elasticity, respiratory muscles and rib cage mechanics, and microvascular exchange) to complete the integrative pulmonary system. The relation among these six modules and their connections are shown in Figure 5.1.

In the following Method section, we first summarize the physiology of the pulmonary blood circulation and the gas exchange system. We then describe the development of these two modules (modeling approach, equations, and parameters). In the Results section, we present simulation results and compare them to healthy human data [114], ARDS patient data [21], and quadriplegic patient data [56]. Finally, we report the model sensitive analysis, prove the model stability and robustness, and conclude on the potential applications of the proposed integrative lung model.

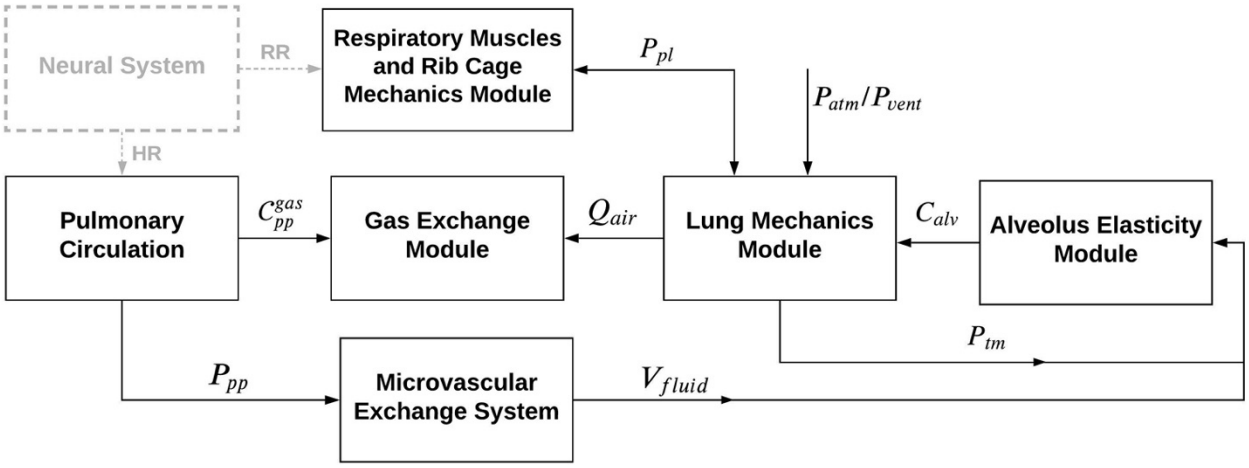

Figure 5. 1: Block diagram of the integrative dynamic pulmonary model. The six modules highlighted in black are described in this dissertation. The full respiratory model comprises: lung mechanics, alveolus elasticity, respiratory muscles and rib cage mechanics, pulmonary microvascular exchange, pulmonary gas exchange, and pulmonary circulation modules. P_{atm}: atmospheric pressure; P_{vent}: ventilator pressure; P_{pl}: pleural cavity pressure; P_{tm}: transmural pressure; C_{alv}: alveolar capacitance; Q_{air}: airflow into and out of the lungs; C_{pp}^{gas}: pulmonary peripheral gas (O_2, CO_2) concentration; P_{pp}: pulmonary peripheral pressure; V_{fluid}: lung fluid volume; RR: respiratory rate; HR: heart rate.

5.2 Method

In this section, the model development of the pulmonary blood circulation and the lung gas exchange systems are introduced. For each module, we first describe the physiology, then we derive the dynamic equations and assign parameter values. The mathematical models of the pulmonary blood circulation and the gas exchange systems have been developed by researchers [1], [2], [44], [112], [113]. We leverage the work of Ursino *et al.* [112], [113], and Albanese *et al.* [3],[8] to verify our equations and parameter values.

5.2.1 The Pulmonary Blood Circulation System

Figure 5.2 shows the schematics of the pulmonary circulation. In the pulmonary circulation, the blood streams from the right ventricle to the left atrium, passing the pulmonary arteries, the pulmonary peripheral vessels, and the pulmonary veins. A pulmonary shunt compartment is added in parallel to the pulmonary peripheral circulation, between the pulmonary arteries and the pulmonary veins to account for the normal physiological amount of blood that bypasses the gas exchange process. When the venous blood (low in O_2 and high in CO_2) enters the pulmonary capillaries, it is in contact with the alveolar space that is rich in O_2 and poor in CO_2. Thereby, gas exchange happens. The resulting O_2 rich blood returns to the heart, and gets transported through the body to deliver O_2.

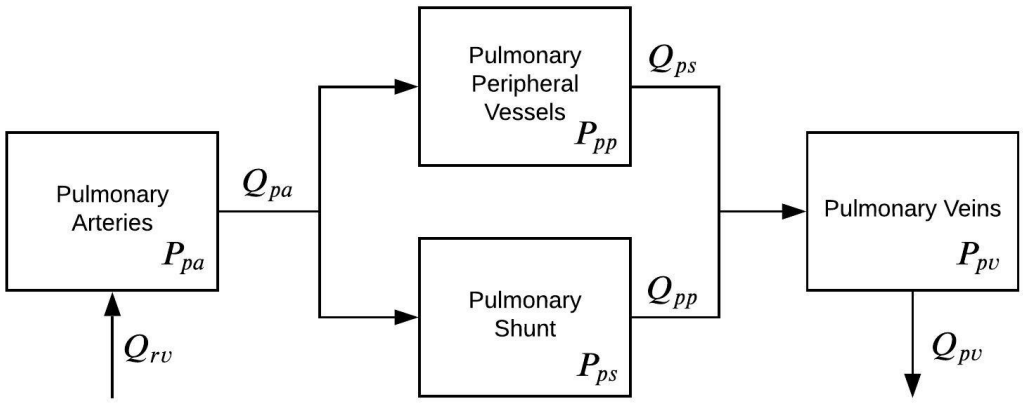

Figure 5. 2: Pulmonary circulation schematics. pa: pulmonary arteries, pp: pulmonary peripherals, pv: pulmonary veins, ps: pulmonary shunts, rv: right ventricle, P: hydraulic pressure, Q: fluid flow.

Each vascular compartment shown in Figure 5.2 is described by traditional Windkessel models, *i.e.* a hydraulic resistance to account for pressure energy losses, and a hydraulic compliance to account for energy storage (blood volume stored at a given pressure). For the compartments where inertial forces in blood are significant, *i.e.*, long pulmonary arteries, inertance is also included as a third parameter to account for kinetic energy storage in the Windkessel type

model. In this work, we adopt the linear graph technique to represent this dynamic system and write its dynamic equations of motion. The pulmonary circulation linear graph is marked in Figure 5.3, and it is drawn in green representing the hydraulic domain. We employ this graphing technique to allow for a systematic formulation of the system's dynamic equations [38]. These equations consist of variables and parameters. Parameters represent material property and geometry of the lung compartments, such as hydraulic resistances and capacitors. Pressures and volumes are termed variables, which could potentially be measured through an instrument. In the pulmonary circulation linear graph (green), every node (solid circle) represents pressure within a compartment of the vascular system. Every line with an arrow represents a flow between two compartments and is labeled with the associated parameter of that segment. We derive the dynamic equations of the pulmonary circulation system as:

$$C_{pa}\frac{d\left(P_{pa}-P_{pl}\right)}{dt}=Q_{rv}-Q_{pa} \tag{5.1}$$

$$L_{pa}\frac{dQ_{pa}}{dt}=P_{pa}-P_{pp}-R_{pa}Q_{pa} \tag{5.2}$$

$$\left(C_{ps}+C_{pp}\right)\frac{d\left(P_{pp}-P_{pl}\right)}{dt}=Q_{pa}-\frac{P_{ps}-P_{pv}}{R_{ps}}-\frac{P_{pp}-P_{pv}}{R_{pp}} \tag{5.3}$$

$$P_{ps}=P_{pp} \tag{5.4}$$

$$C_{pv}\frac{d\left(P_{pv}-P_{pl}\right)}{dt}=\frac{P_{pp}-P_{pv}}{R_{pp}}+\frac{P_{ps}-P_{pv}}{R_{ps}}-\frac{P_{pv}-P_{la}}{R_{pv}} \tag{5.5}$$

where Q is blood flow, P is hydraulic pressure, C is hydraulic capacitance, L is inertance, R is resistance. The subscripts pa represents pulmonary arteries, pp represents pulmonary peripherals, pv represents pulmonary veins, ps represents pulmonary shunts, rv represents right ventricle, and pl represents the pleural cavity pressure. Since the pulmonary shunts and the pulmonary peripherals are assumed to be in parallel and no gravitational effects are considered, the pressures

inside these two compartments are hence assumed to be equal. Note that the only difference between the pulmonary shunts and the pulmonary peripherals are the blood gas concentration, since the blood in the shunts bypasses the gas exchange process. The parameters of the equations in the pulmonary blood circulation are summarized in Table 5.1, including resistances, compliances and inertance at each vascular compartment.

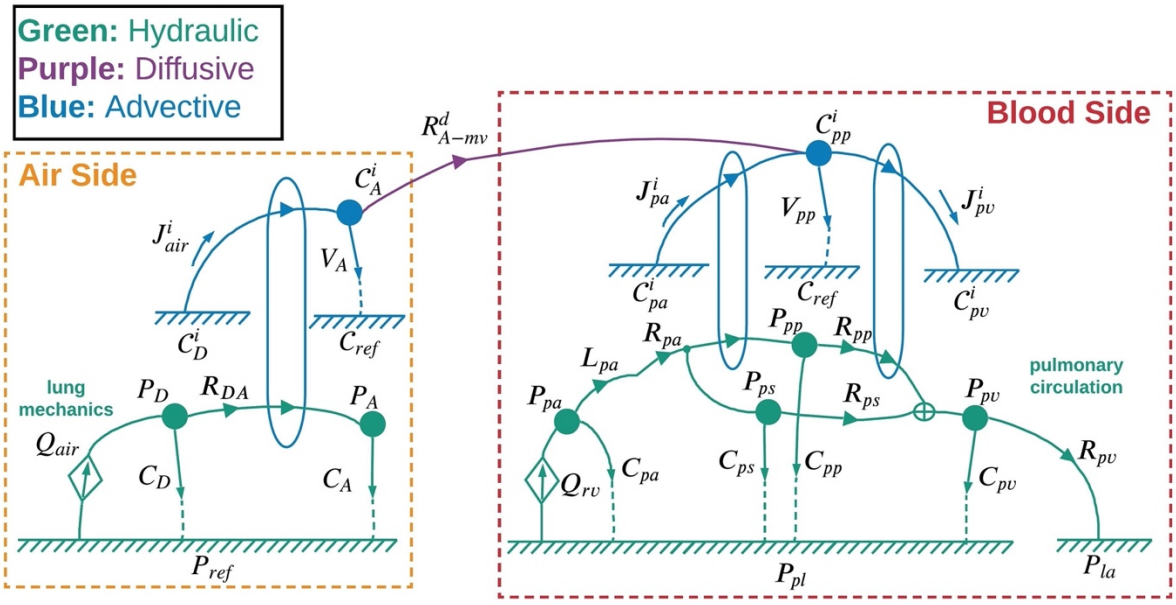

Figure 5. 3: Linear graph of the pulmonary gas exchange and the pulmonary circulation systems. The yellow box represents the gas transport in the lungs, and the red box represents the blood transport in the pulmonary circulation. The purple line represents the gas (O_2, CO_2) diffusion between the air side and the blood side. The green, the purple, and the blue represent hydraulic, diffusion, and advection domains, respectively. pa: pulmonary arteries, pp: pulmonary peripherals, pv: pulmonary veins, ps: pulmonary shunts, A: alveolar space, D: dead space, DA: dead space to alveolar space, ref: reference, rv: right ventricle, la: left atrium, pl: pleural cavity, P: hydraulic pressure, $\mathcal{C}$: concentration, Q: fluid flow, J: mass (gas molecule) flow, V: volume, C: capacitance, R: resistance, L: inertance, i: gas (O_2, CO_2).

Table 5. 1: Parameters of the Pulmonary Circulation

Compliances (ml/mmHg)	**Resistances** $\mathbf{(mmHg \cdot s \cdot ml^{-1})}$	**Inertance** $\mathbf{(mmHg \cdot s^2 \cdot ml^{-1})}$
C_{pa} = 0.76 [112]	R_{pa} = 0.023 [112]	L_{pa} = 0.18e-3 [112]
C_{ps} = 0.0986 [1]	R_{pp} = 0.0909 [1]	
C_{pp} = 5.7014 [1]	R_{ps} = 5.2588 [1]	
C_{pv} = 25.37 [112]	R_{pv} = 0.056 [112]	

5.2.2 The Lung Gas Exchange System

Figure 5.4 shows a schematic block diagram of the lung gas exchange system. The gas exchange system includes: 1) the air side (boxed in yellow) has the anatomical dead space (larynx, trachea, and bronchi in the lung mechanics module) where gas exchange does not take place, and the alveolar space, where gas exchange takes place, and 2) the blood side (boxed in red), *i.e.*, pulmonary peripheral vessels and pulmonary shunts in the pulmonary blood circulation module. Between the air side and the blood side, O_2 enters the blood from the alveoli compartment, and CO_2 gets expelled into the alveoli compartment from blood. In this module, only O_2 and CO_2 gas species are considered, and they are assumed to be ideal gases. Also, every compartment is assumed to be homogenous and perfectly-mixed. The gas fractions in the lungs are computed from their partial pressures via the ideal gas law. Thus, we have FIO_2 = 21.04 % and $FICO_2$ = 0.04 % calculated from the air components.

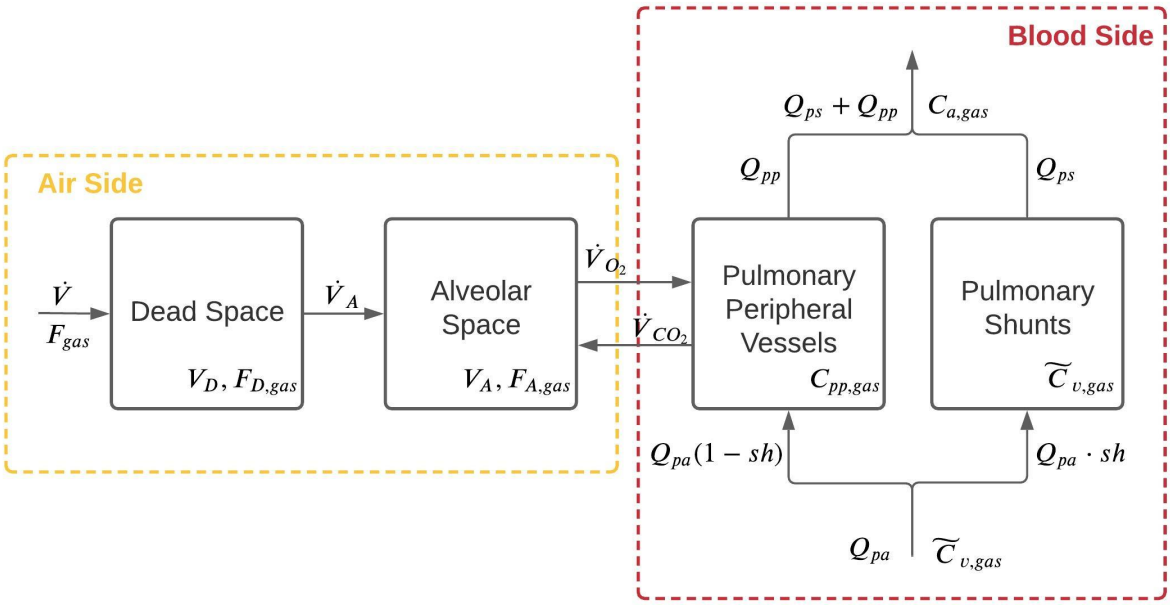

Figure 5. 4: Pulmonary gas exchange system schematics. The yellow box represents the gas transport in the lungs, and the red box represents the blood transport in the pulmonary circulation. $\dot{V}$: airflow into the lungs, $\dot{V}_A$: airflow into the alveoli, $\dot{V}_{O_2}$: oxygen flow, $\dot{V}_{CO_2}$: carbon dioxide flow, F_{gas}: inhaled gas fraction (O_2 and CO_2), V_D: volume of the dead space, V_A: alveolar volume, $F_{A,gas}$: alveoli gas fraction (O_2, CO_2), $F_{D,gas}$: dead space gas fraction (O_2, CO_2), Q_{pa}: blood flow at pulmonary arteries, Q_{pp}: blood flow at pulmonary peripherals, Q_{ps}: blood flow at pulmonary shunt, $\tilde{C}_{v,gas}$: gas concentration at the pulmonary veins, $C_{a,gas}$: gas concentration at the pulmonary arteries, $C_{pp,gas}$: gas concentration at the pulmonary peripherals.

We use linear graph to represent the dynamic gas exchange system as shown in Figure 5.3. In the lung mechanics part (green), air flows into the alveoli due to hydraulic pressure gradient. The gas species that enters the alveolar space follows the bulk air flow (marked in blue) via advection (or convection). The ring that crosses the hydraulic domain and the advection relates the total airflow and the gas (O_2, CO_2) flow via gas fractions. The ring represents an ideal energy transducer (transformer). Each transducer is characterized by a ratio, in this case, the ratio is the gas fraction. Similarly, on the pulmonary circulation side, the ring relates the blood flow and the gas species

flow via the blood gas concentration. From the linear graph, we derive the system dynamic equations following the conservation of mass:

$$V_D dF_{D,gas} = u(\dot{V})\dot{V}(F_{gas} - F_{D,gas}) + u(-\dot{V})\dot{V}_A(F_{D,gas} - F_{A,gas}) \tag{5.6}$$

$$V_A dF_{A,gas} = u(\dot{V})\dot{V}_A(F_{D,gas} - F_{A,gas}) - K\left(Q_{pa}(1-sh)(C_{pp,gas} - \tilde{C}_{v,gas}) + V_{pp}\frac{dC_{pp,gas}}{dt}\right) \tag{5.7}$$

where the subscript gas indicates either O_2 or CO_2, D indicates the dead space, A represents alveoli, u is the Heaviside step function, sh represents the percentage of pulmonary shunts (assumed to be equal to 1.7% [115], see Table 5.2), K is a proportionality constant that allows to convert volumes from BTPS (body temperature pressure saturated) to STPD (standard temperature pressure dry) conditions, V is volume, F is gas fraction, Q is flow, and C is concentration.

In Figure 5.3, the O_2 and CO_2 diffusion between the alveoli and the pulmonary capillary is marked in purple. Empirical dissociation curves [116] are adopted to simulate this gas exchange mechanism, *i.e.*, relating the gas partial pressure in the alveoli to the gas concentration in the pulmonary peripherals. The dissociation curve for O_2 transport is represented in Equations 5.8 and 5.9, and the dissociation curve for CO_2 transport is represented in Equations 5.10 and 5.11.

$$C_{pp,O_2} = C_{pp,O_2}\frac{\left(X_{pp,O_2}\right)^{\frac{1}{h1}}}{1 + \left(X_{pp,O_2}\right)^{\frac{1}{h1}}} \tag{5.8}$$

$$X_{pp,O_2} = P_{A,O_2}\frac{1+\beta_1 P_{A,CO2}}{K_1(1+\alpha_1 P_{A,CO2})} \tag{5.9}$$

$$C_{pp,CO_2} = C_{pp,CO_2}\frac{\left(X_{pp,CO_2}\right)^{\frac{1}{h2}}}{1 + \left(X_{pp,CO_2}\right)^{\frac{1}{h2}}} \tag{5.10}$$

$$X_{pp,CO_2} = P_{A,CO_2}\frac{1+\beta_2 P_{A,O2}}{K_2(1+\alpha_2 P_{A,O2})} \tag{5.11}$$

where $P_{A,gas} = F_{A,gas}(P_{atm} - P_{ws})$, P_{ws} is the water vapor pressure, $h_1, h_2, \alpha_1, \alpha_2, \beta_1, \beta_2, k_1, k_2$ are coefficients in the dissociation curves. The parameter values of the dissociation curves are summarized in Table 5.2.

After solving for the $C_{pp,gas}$, which is the blood concentration of O_2 and CO_2 in the pulmonary peripheral vessels, the blood gas concentration in the arterial blood ($C_{a,gas}$) is then computed via a mixing equation as shown in Equation 5.12. It is the weighted average of the blood coming from the pulmonary capillaries and from the pulmonary shunts:

$$C_{a,gas} = \frac{Q_{pp}C_{pp,gas} + Q_{ps}\tilde{C}_{v,gas}}{Q_{pp} + Q_{ps}} \tag{5.12}$$

where Q_{pp} and Q_{ps} are the blood flow from the pulmonary peripheral vessels and the pulmonary shunts, $C_{pp,gas}$ and $\tilde{C}_{v,gas}$ are the gas (O_2 and CO_2) concentration at the pulmonary peripheral vessels (where gas exchange happens) and at the pulmonary shunts (where gas exchange does not happen), respectively. Note that the blood gas concentration at the pulmonary veins equals to the blood gas concentration at the pulmonary shunts. From the arterial blood gas concentrations, C_{a,O_2} and C_{a,CO_2}, the corresponding partial pressures can be computed by applying the inverse of the dissociation functions. Finally, arterial oxygen saturation can be computed:

$$S_{a,gas}\% = \frac{C_{a,O_2} - P_{a,O_2} \cdot \frac{0.003}{100}}{Hgb \cdot 1.34} \cdot 100 \tag{5.13}$$

where Hgb is the hemoglobin concentration (in per of blood), 1.34 is the oxygen capacity (in g per ml of Hgb) and the term 0.003/100 represents the solubility of O_2 in blood (in ml of O_2 per ml of blood per $mmHg$).

Table 5. 2: Parameters of the Gas Exchange System

ENVIRONMENTAL CONDITIONS	FIO_2 = 21.04 % $FICO_2$ = 0.04% K = 1.21	P_{atm} = 760 mmHg P_{ws} = 47 mmHg
DISSOCIATION CURVES [116]	$C_{sat,O2}$ = 9 mmol/L h_1 = 0.3836 α_1 = 0.03198 $mmHg^{-1}$ β_1 = 0.008275 $mmHg^{-1}$ k_1 = 14.99 mmHg	$C_{sat,CO2}$ = 86.11 mmol/L h_2 = 1.829 α_2 = 0.05591 $mmHg^{-1}$ β_2 = 0.03255 $mmHg^{-1}$ k_2 = 194.4 mmHg
PHYSIOLOGICAL STATUS	sh = 1.7 [115]	Hgb = 15 g/dl [117]

5.3 Results

In this section, the proposed model is first compared to healthy human data reported in [114]. Then, we simulate ARDS and validate against ARDS patient data [21] from Chapter I. We also simulate the gas contents of the quadriplegic patient who breathes via isolated phrenic paced diaphragm as a continuation of Chapter II [56]. Finally, we report the model sensitivity analysis, and assess the stability and robustness of the proposed model.

5.3.1 Simulation and Validation for Healthy Subjects

Upon simulation of the integrative model, normal breathing simulation for a healthy human is shown in Figure 5.5. The partial pressure of oxygen (PaO_2), the partial pressure of carbon dioxide ($PaCO_2$), and the arterial oxygen saturation (SaO_2) are plotted with respect to time. Our simulation results show that the PaO_2 and SaO_2 increase during inspiration and decrease during expiration. However, $PaCO_2$ changes in the opposite direction to PaO_2. This trend is expected, since O_2 enters the blood and CO_2 gets expelled from the blood during inspiration, causing PaO_2 increases while $PaCO_2$ decreases. The healthy simulation has an averaged PaO_2 value of 87.5 mmHg, an averaged $PaCO_2$ value of 40.7 mmHg, and an averaged SaO_2 of 95.8%. All of these values stay in the healthy

range as reported by Castro *et al.* [114]. In addition, there are two periodicities in the signal, the slower one, follows the respiratory rate, while the faster one follows the heart rate. This healthy patient simulation serves as an acceptable preliminary validation of our model.

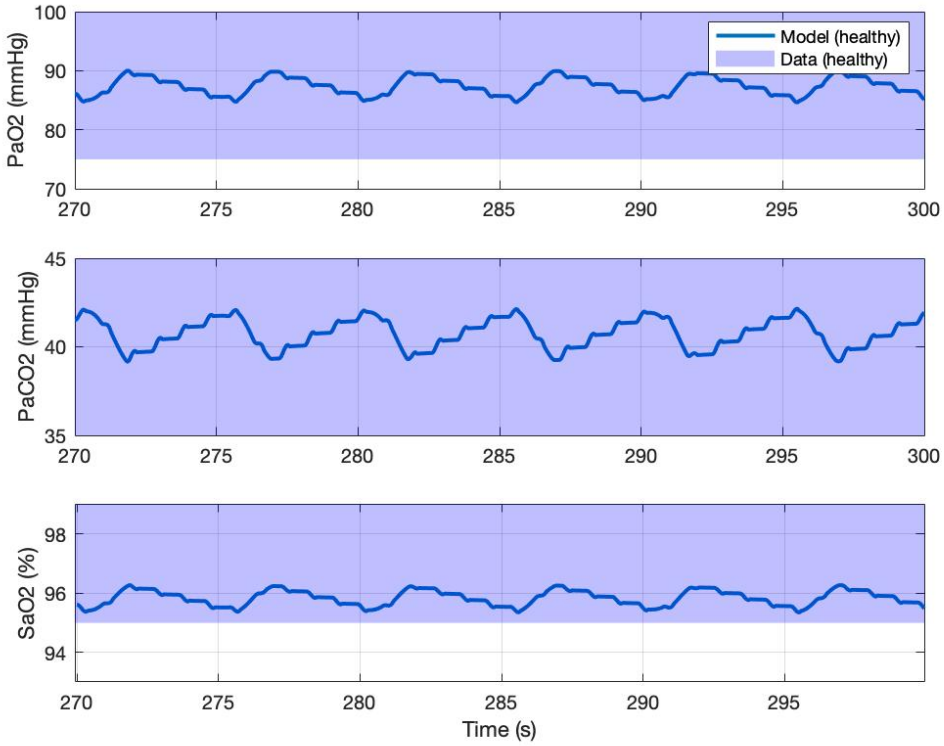

Figure 5. 5: Model simulation of a healthy subject during normal breathing, compared to healthy human data reported in literature [114]. The arterial partial pressure of oxygen (PaO_2), the arterial partial pressure of carbon dioxide ($PaCO_2$), and the arterial oxygen saturation (SaO_2) are reported in the upper, middle, lower panel, respectively.

5.3.2 Simulation and Validation for ARDS Patients

In Chapter I, the lung mechanics variables (airflow, alveolar pressure and alveolar volume) are simulated for ARDS patients with different severity levels defined by Fujioka *et al.* [37]. In this work, since the pulmonary gas exchange system is linked to the lung mechanics module, the blood gas for such ARDS cases are simulated. In Figure 5.6, the arterial oxygen partial pressures (PaO_2)

in time are shown for the healthy (blue) and the two ARDS severity levels (red and yellow): 1) low severity, *i.e.*, 20% reduction in surfactant concentration, and 2) high severity, *i.e.*, 40% reduction in surfactant concentration and 8 times more of collagen volume. For the low and high ARDS severity cases, PaO_2 values are reduced when compare to the healthy patient simulation. The PaO_2 values are reduced to 60 mmHg (31% reduction) and 47 mmHg (46% reduction) for the low and high severities, respectively. This reduction of PaO_2 is expected since an abnormal alveolar compliance causes a low tidal volume, which reduces arterial partial pressure of O_2. Note that both simulated PaO_2 values (low and the high severity cases) fall out of the normal range [114].

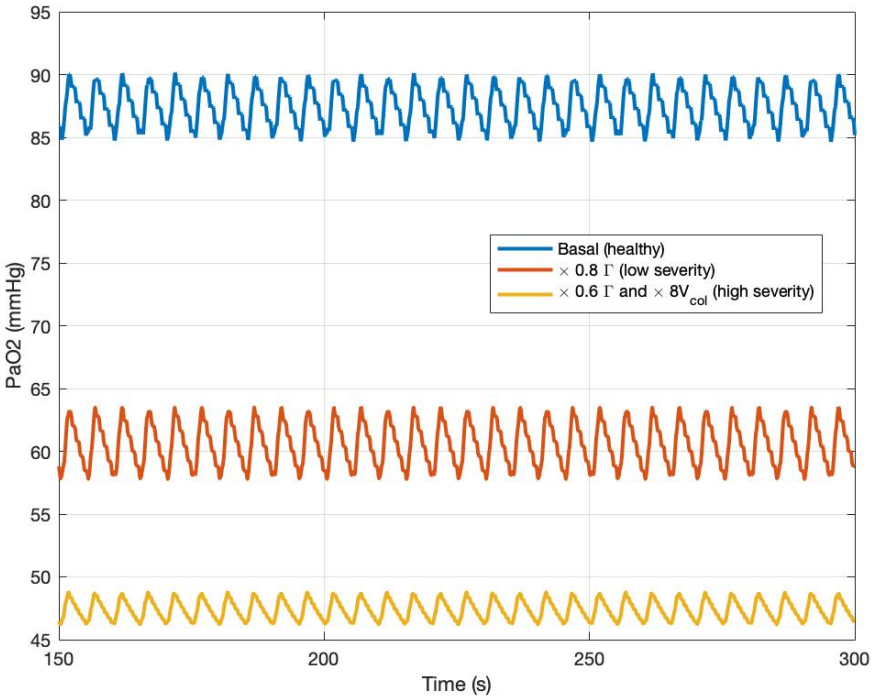

Figure 5. 6: ARDS simulation: healthy (blue) and two severity levels (red and yellow): 1) 20% reduction in surfactant concentration, and 2) 40% reduction in surfactant concentration and 8 times more of collagen volume. The arterial partial pressure of oxygen (PaO_2) is shown.

In the validation of the lung mechanics and the alveolus elasticity modules in Chapter I, Servillo *et al.* [21] reported one exemplary ARDS patient data with a measured PaO_2/FIO_2 (PF ratio). In Chapter I, we estimated the values of the surfactant concentration and the collagen volume of this exemplary patient to replicate the patient's measured PV curve. In this work, as the gas exchange system is linked, we also compute the patient's PF ratio and compare to the reported data. In Figure 5.7, the simulated PF ratio for this ARDS patient in time is plotted in blue, and the PF ratio reported in [21] is shown in red. The simulated PF ratio has an averaged value of 78.9 mmHg, which is highly close to the value reported in [21], 79 mmHg. In this simulation, since the heart rate and venous blood gas concentration are not reported in the literature, a normal heart rate of 70 bpm and a normal venous blood concentration of C_{V,O_2} 15 ml/dl and C_{V,CO_2} of 52 ml/dl are assumed in the simulation.

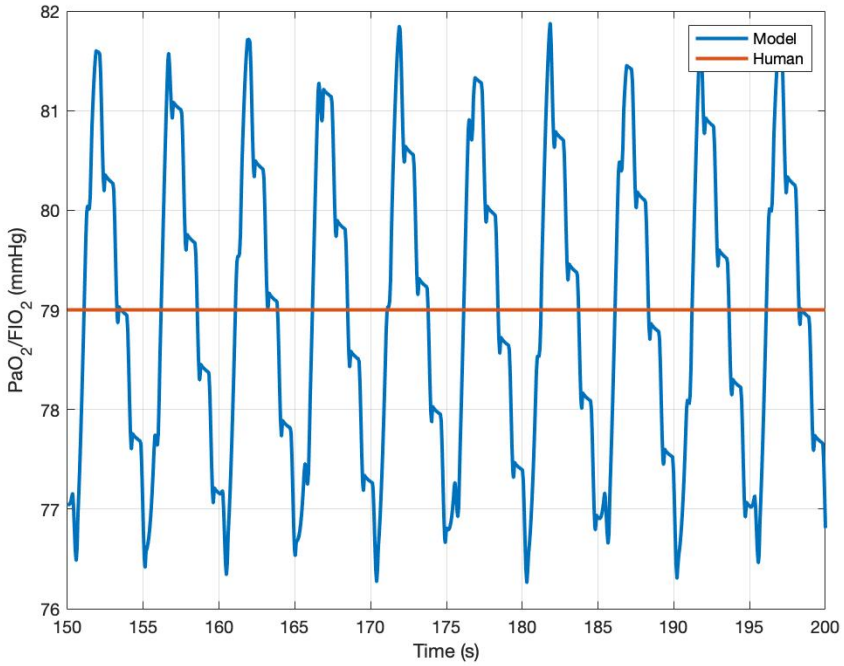

Figure 5. 7: Model validation against ARDS patient from Servillo *et al.* [21]. The blue line represents the simulated PaO_2/FIO_2 ratio, and the red is the measured PaO_2/FIO_2.

5.3.3 Simulation and Validation for Quadriplegic Patients

In the validation of the respiratory muscles and rib cage mechanics module, the quadriplegic patient with phrenic paced diaphragm data [56] was adopted in Chapter II. In Chapter II, we replicated the patient's measured pressure values (abdominal pressure, pleural pressure, and the transmural pressure), the angular displacement of the lower and upper ribs during respiration, and the patient's tidal volume. Figure 5.8 shows the blood gas simulation (PaO_2, $PaCO_2$, SaO_2) of this quadriplegic patient [56]. Since the heart rate and venous blood gas concentration are not reported in the literature, we assumed a normal heart rate of 70 bpm (beats per minute) and a normal venous blood O_2 concentration of 15 ml/dl and CO_2 concentration of 52 ml/dl in the simulation. Due to the support of the phrenic paced diaphragm, the blood gas variables of this quadriplegic patient are all in normal range which agree with the literature [56].

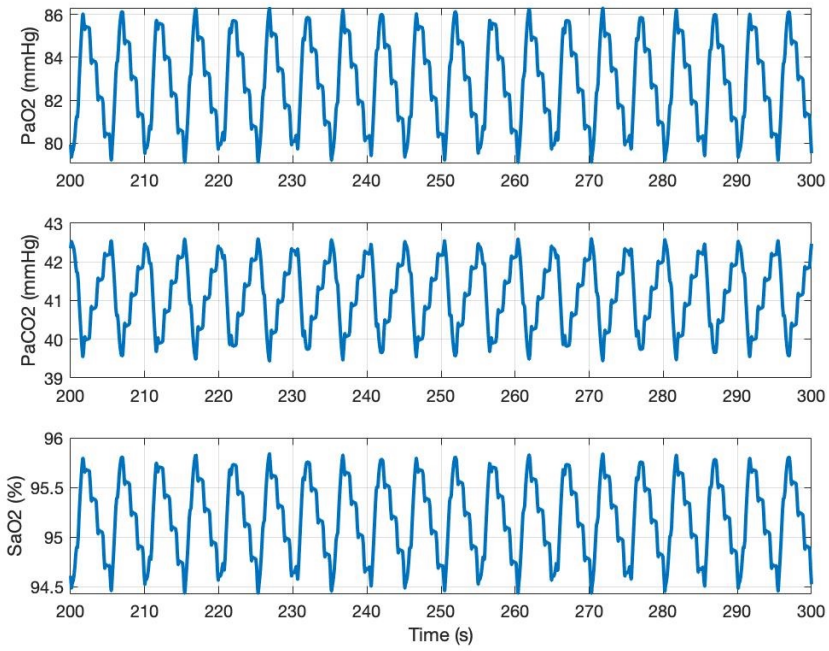

Figure 5. 8: Model simulation of a quadriplegic patient with phrenic paced diaphragm. The partial pressure of oxygen (PaO_2), the partial pressure of carbon dioxide ($PaCO_2$), and the arterial oxygen saturation (SaO_2) are reported in the upper, middle, lower panel, respectively.

5.3.4 Sensitivity Analysis

To evaluate the effects of model parameters on the gas exchange system variables we have performed a sensitivity analysis of the gas exchange variables to changes in parameters. We have computed the sigma (sensitivity) values (Σ) values, and tabulated them in Table 5.3. Sigma values were computed to quantify the sensitivity as $\frac{\Delta Variable \times Parameter}{\Delta Parameter \times Variable}$. The sigma value is a measure of the effect of the change in parameters to changes in variables, where parameters represent material property and geometry of the system (rows of Table 5.3), while variables are the system outputs (columns of Table 5.3). A bigger Σ value indicates a higher sensitivity. Each sigma value is computed using a change in a parameter and corresponding changes in variable. For comparison purposes, we have selected a common range of parameter change in Table 5.2 (50% decrease to a 100% increase in 10% increments). The range -50% to 100% corresponds to halving and doubling each parameter, thereby covering a reasonable range to study negative and positive changes of the nominal value. A mean sigma was then generated for each parameter (across all variables), and reported in the table. For instance, we have discovered that surfactant concentration is the most sensitive parameter across all gas exchange variables and has an average sensitivity of 0.22. This is expected, since the surfactant concentration greatly affects the alveolar compliance that affects the tidal volume, as learnt in Chapter I. The sensitivity analysis of the lung mechanics and alveolar elasticity modules (Chapter I) also agrees that surfactant concentration has a high Σ value. The pleural cavity compliance (C_{pl}) in the respiratory muscles and rib cage mechanics module is the second highest sensitive parameter, across all variables, and has an average sensitivity of 0.098. This agrees with the sensitivity analysis in Chapter II that the lung mechanics variables (pressures and volumes at different lung compartments) are indeed sensitive to C_{pl}. The pulmonary physiology also supports this sensitivity result that pleural cavity pressure (P_{pl}), which is

determined by C_{pl}, dictates the airflow going in and out of the lungs. Hence, C_{pl} is a critical parameter that reflects pulmonary health. Note that, in Chapter I, P_{pl} is modeled as the input to the lung mechanics system. The gas exchange system variables are also very sensitive to the collagen elasticity parameters (c_1, c_2). This result is consistent with the sensitivity results in Chapter I. The importance of the collagen elasticity parameters makes sense, since LM variables are sensitive to the collagen elasticity parameters (shown in the sensitivity analysis in Chapter I), and the LM variables directly affect ventilation, thus the blood oxygenation. The resistances and compliances of the upper airways (R_{bA},R_{tb}, R_{lt}, C_l, C_{tr}, and C_b) were the least sensitive parameters. This observation is expected since parameters affecting the alveolar compartment (and not the upper airways) are the main determinants of respiratory conditions such as ARDS and IPF [12]–[17].

Table 5. 3: Sensitivity analysis

Σ	PaO_2	$PaCO_2$	SaO_2	CaO_2	$CaCO_2$	*Mean*
Γ	0.6871	0.1577	0.0985	0.1057	0.0884	0.22748
C_{pl}	0.3193	0.0553	0.0398	0.0433	0.0341	0.09836
c_2	0.3001	0.0504	0.0397	0.0429	0.0313	0.09288
c_1	0.2851	0.0463	0.0356	0.0387	0.0292	0.08698
C_{abd}	0.209	0.0502	0.023	0.0256	0.0284	0.06724
V_{col}	0.1596	0.0297	0.0184	0.0202	0.018	0.04918
R_{ml}	0.07	0.015	0.0077	0.0086	0.0088	0.02202
C_b	0.0608	0.0125	0.0067	0.0075	0.0074	0.01898
R_{tb}	0.014	0.0031	0.0015	0.0017	0.0018	0.00442
C_{tr}	0.0123	0.0026	0.0013	0.0015	0.0015	0.00384
R_{bA}	0.0079	0.0017	0.0009	0.001	0.001	0.0025
R_{lt}	0.0068	0.0013	0.0007	0.0008	0.0008	0.00208
C_l	0.0005	0.0001	0.0001	0.0001	0.0001	0.00018

Next, let us compute a confidence metric of our simulation based on the sensitivity analysis. Sensitivity analysis tells us what is the most/least sensitive parameter, however, it does not give an indication on the confidence ranges of those variables. We choose to quantify the confidence

ranges of the model variables (akin to confidence intervals) by varying (increasing and decreasing) the basal parameters by 10%, and then performing model simulation. Take the surfactant concentration (the most sensitive parameter) as an example, with a change of normal surfactant concentration from -10% to 10%, the simulation of SaO_2 values are in the range [94.58, 96.59] %, PaO_2 values in the range [79.17, 94.33] mmHg, and $PaCO_2$ values in the range [40.01, 41.38] mmHg. All the ranges are enveloped by the healthy variable ranges reported in the literature [114], which gives further credence to the integrative lung model. Similarly, the range of the lung mechanics variables are also simulated to be within the healthy variable ranges, *e.g.*, tidal volume (Chapter I) is in the range [0.4, 0.58] L.

5.3.5 Model Stability and Robustness Assessment

In this part of the work, we assess the stability and the robustness of the proposed model. To prove numerical stability, we have simulated the model for more than 4000 breaths (300+ simulation hours) on a 2.9GHz 8GB machine. The model outputs PaO_2 and alveolar volume are plotted on a phase plane as shown in Figure 5.9. Both PaO_2 and alveolar volume are well-known indicators of blood oxygenation and ventilation in the lung gas exchange system and lung mechanics module respectively. Hence, we plot those two important states against each other (PaO_2 vs alveolar volume) for healthy (blue), low severity (red) and high severity (yellow) levels (following Figure 5.5). The system output loops (PaO_2 vs alveolar volume) are closed, indicating a well-behaved system under both healthy (unperturbed) and diseased (perturbed) cases. Through these analyses, system stability is maintained when multiplicative factors perturbing the parameters (representing lung diseases) are bound by the following limits: $R_{ml} > 0, R_{lt} > 0, R_{tb} > 0, R_{bA} > 0, C_l > 0, C_{tr} > 0, C_b > 0, C_{pl} > 0, C_{abd} > 0, V_{col} > 0, \Gamma \geq 0, c_1 > 0,$ and $0 < c_2 \leq 1$. Note that

physiological systems typically have positive-only parameters, since negative parameter values do not have physical meaning.

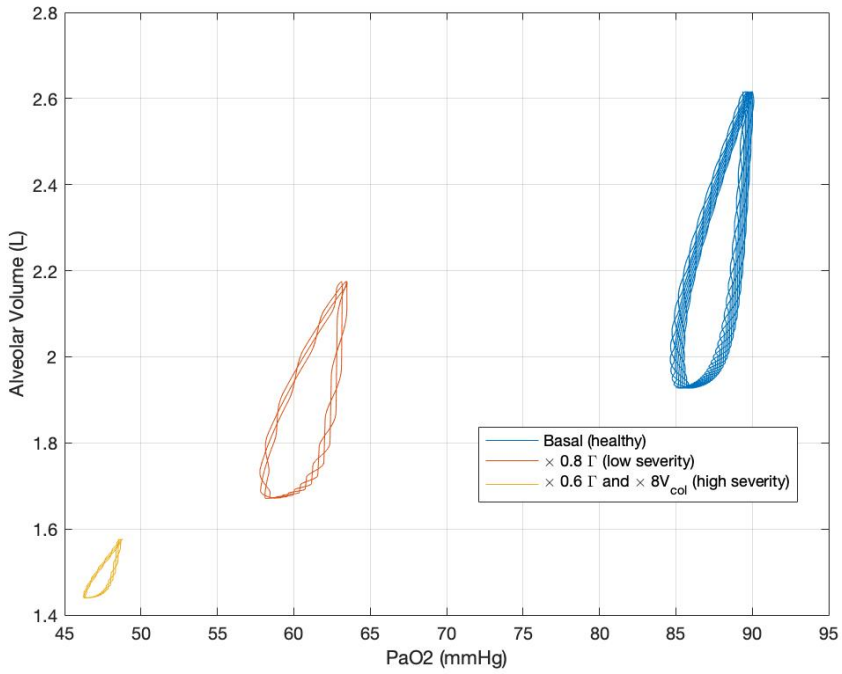

Figure 5. 9: Model output loops (PaO_2 vs Alveolar volume) for long-time breathing simulation in healthy (blue), low severity (red) and high severity (yellow) sickness levels. Low severity: 20% reduction in surfactant concentration. High severity: 40% reduction in surfactant concentration and 8 times increase in basal collagen volume.

5.4 Conclusion

In this chapter, we have completed an integrative lung model that includes six pulmonary modules: lung mechanics, alveolus elasticity, respiratory muscles and rib cage mechanics, microvascular exchange, pulmonary circulation, and pulmonary gas exchange. This lung model simulates the pulmonary variables, across three transport mechanism: hydraulic, diffusive, and

advective, including lung pressures and volumes, rib cage kinematics, blood gas contents, lung fluid balance, and pulmonary vascular pressures.

A dynamic model of the pulmonary system for predicting diseases is still uncommon in current medicine. However, its benefits are numerous, including parameters that have real physical meaning and changes in which can be related to diseases and/or interventions. The proposed integrative pulmonary system elevates the understanding of the lung normo- and patho-physiology via its integrative physiological knowledge and their mathematical functions. This model provides users the freedom to change the parameters that relate to a disease, and outputs the corresponding variables that reflect the patient's health. The proposed model can also forecast the state of breathing mechanisms under healthy and diseased conditions by performing long time simulation. In addition, different therapeutic scenarios can be tested on the proposed dynamic respiratory model so that the optimal therapy can be found for a specific patient. In addition, system identification techniques can be applied to this, or part of this, model to achieve personalized medicine for better disease diagnosis and treatment.

In future work, we will replace the simplistic pulmonary system in the cardio-pulmonary model developed by Albanese [1] with the proposed integrative pulmonary model to create a more rigorous cardio-pulmonary model. Then, more model validation against real human data should be performed. In addition, parameter estimation techniques can be applied to this, or part of this, model in order to personalize for the individual.

Chapter VI: Summary and Future Work

6.1 Summary

In this thesis we have taken another step toward personalized medicine via a physiology-based model and optimization algorithms, which improves patient health assessment, diagnosis, and therapy. This work proposed a dynamic pulmonary system that includes: 1) a lung mechanics module (Chapter I) that quantitatively describe the change of lung pressures and volumes, 2) an alveolus elasticity module (Chapter I) that determines the alveolar compliance as a function of surfactant concentration and lung fiber elasticity, 3) a respiratory muscles and rib cage mechanics module (Chapter II) that computes the rib cage movement and the variation of the pleural cavity pressure as the respiratory muscles (diaphragm and intercostal muscles) contract and relax during respiration, 4) a microvascular exchange system (Chapter IV) that describes the fluid (water) and mass (protein) transport between the alveoli and the pulmonary capillaries, 5) a lung gas exchange system (Chapter V) that quantitatively describes the oxygen and carbon dioxide transport between the air in the lungs and the blood in the pulmonary microvessels, and 6) a pulmonary blood circulation module (Chapter V) that describes the blood flows from the heart to the pulmonary system. Each module was developed based on the latest knowledge of lung physiology and was validated using patient data when available or published and validated physiology-based models when data is unavailable. This dynamic respiratory system can be used to describe human breathing under healthy and diseased conditions. It provides users the freedom to change the parameters that relate to a disease, and outputs the variables that reflect the patient health. Different therapeutic scenarios can be tested on the proposed dynamic respiratory model so that an optimal therapy can be found for a patient. In addition, system identification techniques can be applied to

this model, or part of it, to achieve personalized medicine for better disease diagnosis and treatment.

To assess the pulmonary health state of a *specific* patient, we have also developed a simplistic lung mechanics model. Utilizing this simplistic model, the parameters that represent the state of lung health and pulmonary functionality, *i.e.*, the lung mechanical properties (resistance and compliance) and the patient breathing effort, can be estimated via system identification techniques. Pulmonary syndromes or diseases, such as ARDS and COPD (Chronic Obstructive Pulmonary Disease) evoke alterations in lung resistance and compliance. Tracking these two parameters thus can lead to better disease diagnosis and easier monitoring of the respiratory disease progression. In Chapter III, a model-based nonlinear constrained optimization algorithm is developed to estimate, breath-by-breath, the lung resistance, the lung compliance, as well as the patient breathing effort due to the respiratory muscle activity, using readily available non-invasive measurements (airway opening pressure and airflow). Data collected from a lung emulator built at Quadrus Medical Technologies is used to test the algorithms. Utilizing the developed optimization algorithms along with the data collected from the lung emulator, we manage to estimate the lung mechanics parameters (resistance and compliance) and the respiratory muscle effort within an average percent error of only 5%.

6.2 Future work

The proposed pulmonary system and the developed optimization algorithms are a successful first step that accomplish one application of personalized medicine. This work can be further expanded in terms of modeling and parameter estimation so that the proposed work can achieve

personalized medicine under more conditions. In the following, we articulate some proposed future work per chapter.

Chapter I: Utilizing the proposed dynamic model, the development of ARDS and IPF in time becomes possible to simulate. To validate such a model, ARDS and IPF human studies that measure the pleural cavity pressure and lung volume in time would be needed. Another piece of work would involve the real-time estimation of the lung fiber elasticity and the alveolar surfactant concentration so to achieve personalized medicine.

Chapter II: The proposed model simulates human quiet breathing involving intercostal and diaphragm muscles activity only. For future research, the contraction of the accessary respiratory muscles (scalene muscles) ought to be included in order to simulate breathing during exercise (forced respiration). To validate forced respiration, human studies that measure the lower and upper rib angular displacement, sternum movement, abdominal and pleural cavity pressures would be needed.

Chapter III: Testing of the proposed optimization algorithms on human or animal should be the next step to extend this chapter's work. The human/animal airway opening pressure and airflow measurements would be required for optimization, and the alveolar and pleural pressure measurements are needed to compute the true lung mechanics parameters for algorithm validation.

Chapter IV: In future work, this model can be expanded by including: 1) sodium-potassium pumping transport mechanism, and 2) additional blood ions (sodium, potassium, *etc*.) transport to simulate a more realistic blood condition. To further validate the lung water accumulation for heart failure patients, human studies that measure the change of extravascular lung water volume in time and pulmonary peripheral pressure are needed.

Chapter V: One of the future research possibilities is the simulation of corona virus disease (COVID) utilizing the proposed integrative lung model. Human studies are needed to further validate COVID simulation using the proposed model. COVID patients are known to be lung mechanics compromised or gas exchange compromised. To simulate and validate the lung mechanics compromised COVID patient, the measurement of pressure-volume curve is needed to estimate lung mechanics parameters. For the gas exchange compromised type, measurements of heart rate, arterial and venous blood gas concentration would be needed to estimate the parameters of the gas exchange system (the gas dissociation curve). The simulation of COVID patients with the estimated lung parameters can provide clinicians with specific what-if scenarios.

In addition, the pulmonary system in the cardio-pulmonary (CP) model developed by Albanese [1] should be enhanced with the proposed integrative pulmonary model. With the full CP model, more model-based applications can be researched, for example, fluid management, drug infusion, cardio-pulmonary interaction and monitoring, *etc*.

Bibliography

[1] A. Albanese, L. Cheng, M. Ursino, and N. W. Chbat, "An integrated mathematical model of the human cardiopulmonary system: model development," Am. J. Physiol.-Heart Circ. Physiol., vol. 310, no. 7, pp. H899–H921, Dec. 2015, doi: 10.1152/ajpheart.00230.2014.

[2] N. Karamolegkos, "Modeling and Estimation of Cardiorespiratory Function, with Application to Mechanical Ventilation," 2018, doi: 10.7916/D8H14JC3.

[3] B. J. Czerwin, J. Yuan, C. M. Chiofolo, and N. W. Chbat, "Modeling Transport Mechanisms in the Kidney Proximal Tubule: Rodent Renal Validation."

[4] E. R. Weibel, "Morphometry of the Human Lung." https://www.springer.com/gp/book/9783642875557 (accessed Nov. 25, 2019).

[5] S. A. Khonsary, "Guyton and Hall: Textbook of Medical Physiology," Surg. Neurol. Int., vol. 8, Nov. 2017, doi: 10.4103/sni.sni_327_17.

[6] A. C. Guyton, T. G. Coleman, and H. J. Granger, "Circulation: overall regulation," Annu. Rev. Physiol., vol. 34, pp. 13–46, 1972, doi: 10.1146/annurev.ph.34.030172.000305.

[7] J. B. West, Respiratory Physiology: The Essentials, Ninth edition. Philadelphia: LWW, 2011.

[8] J. Yuan, C. M. Chiofolo, B. J. Czerwin, and N. W. Chbat, "Modeling of Transport Mechanisms in the Respiratory System: Validation via Congestive Heart Failure Patients," in 2019 41st Annual International Conference of the IEEE Engineering in Medicine and Biology Society (EMBC), Jul. 2019, pp. 2361–2364, doi: 10.1109/EMBC.2019.8856569.

[9] D. Rowell and D. N. Wormley, System Dynamics: An Introduction, 1 edition. Upper Saddle River, NJ: Pearson, 1996.

[10] B. Suki, D. Stamenovic, and R. Hubmayr, "Lung Parenchymal Mechanics," Compr. Physiol., vol. 1, no. 3, pp. 1317–1351, Jul. 2011, doi: 10.1002/cphy.c100033.

[11] M. Griese, "Pulmonary surfactant in health and human lung diseases: state of the art," Eur. Respir. J., vol. 13, no. 6, pp. 1455–1476, Jun. 1999, doi: 10.1183/09031936.99.13614779.

[12] J. F. Lewis and A. H. Jobe, "Surfactant and the adult respiratory distress syndrome," Am. Rev. Respir. Dis., vol. 147, no. 1, pp. 218–233, Jan. 1993, doi: 10.1164/ajrccm/147.1.218.

[13] L. Armstrong et al., "Changes in collagen turnover in early acute respiratory distress syndrome," Am. J. Respir. Crit. Care Med., vol. 160, no. 6, pp. 1910–1915, Dec. 1999, doi: 10.1164/ajrccm.160.6.9811084.

[14] J. A. Last, A. D. Siefkin, and K. M. Reiser, "Type I collagen content is increased in lungs of patients with adult respiratory distress syndrome," Thorax, vol. 38, no. 5, pp. 364–368, May 1983, doi: 10.1136/thx.38.5.364.

[15] M. Selman, M. Montaño, C. Ramos, and R. Chapela, “Concentration, biosynthesis and degradation of collagen in idiopathic pulmonary fibrosis,” Thorax, vol. 41, no. 5, pp. 355–359, May 1986, doi: 10.1136/thx.41.5.355.

[16] J. D. Fulmer et al., “Collagen concentration and rates of synthesis in idiopathic pulmonary fibrosis,” Am. Rev. Respir. Dis., vol. 122, no. 2, pp. 289–301, Aug. 1980, doi: 10.1164/arrd.1980.122.2.289.

[17] J. M. Seyer, E. T. Hutcheson, and A. H. Kang, “Collagen polymorphism in idiopathic chronic pulmonary fibrosis.,” J. Clin. Invest., vol. 57, no. 6, pp. 1498–1507, Jun. 1976.

[18] R. S. Harris, “Pressure-Volume Curves of the Respiratory System,” Respir. Care, vol. 50, no. 1, pp. 78–99, Jan. 2005.

[19] L. Gattinoni, D. Chiumello, and S. Rossi, “COVID-19 pneumonia: ARDS or not?,” Crit. Care, vol. 24, no. 1, p. 154, Apr. 2020, doi: 10.1186/s13054-020-02880-z.

[20] D. F. Proctor, “The upper airways. I. Nasal physiology and defense of the lungs,” Am. Rev. Respir. Dis., vol. 115, no. 1, pp. 97–129, Jan. 1977, doi: 10.1164/arrd.1977.115.1.97.

[21] G. Servillo et al., “Pressure-volume curves in acute respiratory failure: automated low flow inflation versus occlusion.,” Am. J. Respir. Crit. Care Med., vol. 155, no. 5, pp. 1629–1636, May 1997, doi: 10.1164/ajrccm.155.5.9154868.

[22] S. Orfao, N. Hochhausen, R. Kuhlen, and D. Henzler, “Analysis of Sigmoidal Equations To Describe the Pulmonary Pressure- Volume Curve in Acute Respiratory Distress Syndrome,” Open Crit. Care Med. J., vol. 1, no. 1, Dec. 2008, Accessed: Jun. 03, 2020. [Online]. Available: https://benthamopen.com/ABSTRACT/TOCCMJ-1-54.

[23] C. Pereira et al., “Sigmoidal equation for lung and chest wall volume-pressure curves in acute respiratory failure,” J. Appl. Physiol. Bethesda Md 1985, vol. 95, no. 5, pp. 2064–2071, Nov. 2003, doi: 10.1152/japplphysiol.00385.2003.

[24] J. C. Ferreira et al., “A sigmoidal fit for pressure-volume curves of idiopathic pulmonary fibrosis patients on mechanical ventilation: clinical implications,” Clin. Sao Paulo Braz., vol. 66, no. 7, pp. 1157–1163, 2011, doi: 10.1590/s1807-59322011000700006.

[25] J. H. T. Bates, “Lung Mechanics.” https://www-cambridge-org.ezproxy.cul.columbia.edu/core/books/lung-mechanics/D95220907DAF0A264FA80925AE5E1127 (accessed Nov. 25, 2019).

[26] M. H. Victor Júnior et al., “Parameter estimation of an artificial respiratory system under mechanical ventilation following a noisy regime,” Res. Biomed. Eng., vol. 31, no. 4, pp. 343–351, Dec. 2015, doi: 10.1590/2446-4740.0581.

[27] F. Vicario, A. Albanese, D. Wang, N. Karamolegkos, and N. W. Chbat, “Simultaneous Parameter and Input Estimation of a Respiratory Mechanics Model,” in Modeling, Simulation

and Optimization of Complex Processes HPSC 2015, Cham, 2017, pp. 235–247, doi: 10.1007/978-3-319-67168-0_19.

[28] V. C. Rideout, Mathematical and Computer Modeling of Physiological Systems. Upper Saddle River, NJ, USA: Prentice-Hall, Inc., 1991.

[29] G. Galster, "Source code for a model of pulmonary mechanics," 1995.

[30] J. G. Venegas, R. S. Harris, and B. A. Simon, "A comprehensive equation for the pulmonary pressure-volume curve," J. Appl. Physiol. Bethesda Md 1985, vol. 84, no. 1, pp. 389–395, Jan. 1998, doi: 10.1152/jappl.1998.84.1.389.

[31] E. Denny and R. C. Schroter, "The mechanical behavior of a mammalian lung alveolar duct model," J. Biomech. Eng., vol. 117, no. 3, pp. 254–261, Aug. 1995, doi: 10.1115/1.2794178.

[32] E. Denny and R. C. Schroter, "Relationships between alveolar size and fibre distribution in a mammalian lung alveolar duct model," J. Biomech. Eng., vol. 119, no. 3, pp. 289–297, Aug. 1997, doi: 10.1115/1.2796093.

[33] E. Denny and R. C. Schroter, "Viscoelastic behavior of a lung alveolar duct model," J. Biomech. Eng., vol. 122, no. 2, pp. 143–151, Apr. 2000, doi: 10.1115/1.429644.

[34] E. Denny and R. C. Schroter, "A model of non-uniform lung parenchyma distortion," J. Biomech., vol. 39, no. 4, pp. 652–663, 2006, doi: 10.1016/j.jbiomech.2005.01.010.

[35] J. A. Clements, E. S. Brown, and R. P. Johnson, "Pulmonary Surface Tension and the Mucus Lining of the Lungs: Some Theoretical Considerations," J. Appl. Physiol., vol. 12, no. 2, pp. 262–268, Mar. 1958, doi: 10.1152/jappl.1958.12.2.262.

[36] E. M. Scarpelli, B. C. Clutario, and F. A. Taylor, "Preliminary identification of the lung surfactant system," J. Appl. Physiol., vol. 23, no. 6, pp. 880–886, Dec. 1967, doi: 10.1152/jappl.1967.23.6.880.

[37] H. Fujioka, D. Halpern, and D. P. Gaver, "A model of surfactant-induced surface tension effects on the parenchymal tethering of pulmonary airways," J. Biomech., vol. 46, no. 2, pp. 319–328, Jan. 2013, doi: 10.1016/j.jbiomech.2012.11.031.

[38] D. Rowell and D. N. Wormley, System Dynamics: An Introduction, 1 edition. Upper Saddle River, NJ: Pearson, 1996.

[39] E. H. Oldmixon and F. G. Hoppin, "Distribution of elastin and collagen in canine lung alveolar parenchyma," J. Appl. Physiol. Bethesda Md 1985, vol. 67, no. 5, pp. 1941–1949, Nov. 1989, doi: 10.1152/jappl.1989.67.5.1941.

[40] Y. C. Fung, "A model of the lung structure and its validation," J. Appl. Physiol. Bethesda Md 1985, vol. 64, no. 5, pp. 2132–2141, May 1988, doi: 10.1152/jappl.1988.64.5.2132.

[41] R. R. Mercer and J. D. Crapo, “Spatial distribution of collagen and elastin fibers in the lungs,” J. Appl. Physiol., Aug. 1990, doi: 10.1152/jappl.1990.69.2.756.

[42] S. Schurch, H. Bachofen, J. Goerke, and F. Possmayer, “A captive bubble method reproduces the in situ behavior of lung surfactant monolayers,” J. Appl. Physiol., vol. 67, no. 6, pp. 2389–2396, Dec. 1989, doi: 10.1152/jappl.1989.67.6.2389.

[43] B. M. Carlson, “Chapter 11 - The Respiratory System,” in The Human Body, B. M. Carlson, Ed. Academic Press, 2019, pp. 303–319.

[44] L. Cheng, A. Albanese, M. Ursino, and N. W. Chbat, “An integrated mathematical model of the human cardiopulmonary system: model validation under hypercapnia and hypoxia,” Am. J. Physiol.-Heart Circ. Physiol., vol. 310, no. 7, pp. H922–H937, Apr. 2016, doi: 10.1152/ajpheart.00923.2014.

[45] “Acute Respiratory Distress Syndrome: The Berlin Definition,” JAMA, vol. 307, no. 23, pp. 2526–2533, Jun. 2012, doi: 10.1001/jama.2012.5669.

[46] J. Guttmann, L. Eberhard, G. Wolff, W. Bertschmann, J. Zeravik, and M. Adolph, “Maneuver-free determination of compliance and resistance in ventilated ARDS patients,” Chest, vol. 102, no. 4, pp. 1235–1242, Oct. 1992, doi: 10.1378/chest.102.4.1235.

[47] P. H. N. Saldiva, V. C. Delmonte, C. R. R. de Carvalho, R. A. Kairalla, and J. O. Costa Auler, “Histochemical Evaluation of Lung Collagen Content in Acute and Chronic Interstitial Diseases,” Chest, vol. 95, no. 5, pp. 953–957, May 1989, doi: 10.1378/chest.95.5.953.

[48] R. H. Kallet, “Should PEEP Titration Be Based on Chest Mechanics in Patients With ARDS?,” Respir. Care, vol. 61, no. 6, pp. 876–890, Jun. 2016, doi: 10.4187/respcare.04657.

[49] T. E. King, A. Pardo, and M. Selman, “Idiopathic pulmonary fibrosis,” The Lancet, vol. 378, no. 9807, pp. 1949–1961, Dec. 2011, doi: 10.1016/S0140-6736(11)60052-4.

[50] A. De Troyer and M. Estenne, “Coordination between rib cage muscles and diaphragm during quiet breathing in humans,” J. Appl. Physiol., vol. 57, no. 3, pp. 899–906, Sep. 1984, doi: 10.1152/jappl.1984.57.3.899.

[51] E. R. Donley, M. R. Holme, and J. W. Loyd, “Anatomy, Thorax, Wall Movements,” in StatPearls, Treasure Island (FL): StatPearls Publishing, 2020.

[52] J. Mead and S. H. Loring, “Analysis of volume displacement and length changes of the diaphragm during breathing,” J. Appl. Physiol., vol. 53, no. 3, pp. 750–755, Sep. 1982, doi: 10.1152/jappl.1982.53.3.750.

[53] Z. Shahid and B. Burns, “Anatomy, Abdomen and Pelvis, Diaphragm,” in StatPearls, Treasure Island (FL): StatPearls Publishing, 2020.

[54] J. Ayoub et al., “Non-invasive quantification of diaphragm kinetics using m-mode sonography,” Can. J. Anaesth. J. Can. Anesth., vol. 44, no. 7, pp. 739–744, Jul. 1997, doi: 10.1007/BF03013389.

[55] J. Mills, “Intra-abdominal pressures during quiet breathing.” https://www.ncbi.nlm.nih.gov/pmc/articles/PMC1393069/ (accessed Nov. 25, 2019).

[56] J. Danon, W. S. Druz, N. B. Goldberg, and J. T. Sharp, “Function of the isolated paced diaphragm and the cervical accessory muscles in C1 quadriplegics,” Am. Rev. Respir. Dis., vol. 119, no. 6, pp. 909–919, Jun. 1979, doi: 10.1164/arrd.1979.119.6.909.

[57] J. S. Mecklenburgh, T. A. al-Obaidi, and W. W. Mapleson, “A model lung with direct representation of respiratory muscle activity,” Br. J. Anaesth., vol. 68, no. 6, pp. 603–612, Jun. 1992, doi: 10.1093/bja/68.6.603.

[58] P. T. Macklem, “A mathematical and graphical analysis of inspiratory muscle action,” Respir. Physiol., vol. 38, no. 2, pp. 153–171, Oct. 1979, doi: 10.1016/0034-5687(79)90034-3.

[59] D. C. Grinnan and J. D. Truwit, “Clinical review: Respiratory mechanics in spontaneous and assisted ventilation,” Crit. Care, vol. 9, no. 5, pp. 472–484, 2005, doi: 10.1186/cc3516.

[60] M. E. Ward, J. W. Ward, and P. T. Macklem, “Analysis of human chest wall motion using a two-compartment rib cage model,” J. Appl. Physiol. Bethesda Md 1985, vol. 72, no. 4, pp. 1338–1347, Apr. 1992, doi: 10.1152/jappl.1992.72.4.1338.

[61] C. M. Kenyon et al., “Rib cage mechanics during quiet breathing and exercise in humans,” J. Appl. Physiol. Bethesda Md 1985, vol. 83, no. 4, pp. 1242–1255, Oct. 1997, doi: 10.1152/jappl.1997.83.4.1242.

[62] T. A. Wilson, “Compartmental models of the chest wall and the origin of Hoover’s sign,” Respir. Physiol. Neurobiol., vol. 210, pp. 23–29, May 2015, doi: 10.1016/j.resp.2015.01.010.

[63] A. De Troyer, “The action of the canine diaphragm on the lower ribs depends on activation,” J. Appl. Physiol. Bethesda Md 1985, vol. 111, no. 5, pp. 1266–1271, Nov. 2011, doi: 10.1152/japplphysiol.00402.2011.

[64] A. De Troyer, “Respiratory effect of the lower rib displacement produced by the diaphragm,” J. Appl. Physiol., vol. 112, no. 4, pp. 529–534, Feb. 2012, doi: 10.1152/japplphysiol.01067.2011.

[65] W. W. Glenn, J. F. Hogan, J. S. Loke, T. E. Ciesielski, M. L. Phelps, and R. Rowedder, “Ventilatory support by pacing of the conditioned diaphragm in quadriplegia,” N. Engl. J. Med., vol. 310, no. 18, pp. 1150–1155, May 1984, doi: 10.1056/NEJM198405033101804.

[66] W. W. Glenn, W. G. Holcomb, R. K. Shaw, J. F. Hogan, and K. R. Holschuh, “Long-term ventilatory support by diaphragm pacing in quadriplegia.,” Ann. Surg., vol. 183, no. 5, pp. 566–577, May 1976.

[67] N. S. Arora and D. F. Rochester, “Effect of body weight and muscularity on human diaphragm muscle mass, thickness, and area,” J. Appl. Physiol., vol. 52, no. 1, pp. 64–70, Jan. 1982, doi: 10.1152/jappl.1982.52.1.64.

[68] M. Cassart, N. Pettiaux, P. A. Gevenois, M. Paiva, and M. Estenne, “Effect of chronic hyperinflation on diaphragm length and surface area,” Am. J. Respir. Crit. Care Med., vol. 156, no. 2 Pt 1, pp. 504–508, Aug. 1997, doi: 10.1164/ajrccm.156.2.9612089.

[69] A. D. Troyer and T. A. Wilson, “Action of the diaphragm on the rib cage,” J. Appl. Physiol. Bethesda Md 1985, vol. 121, no. 2, pp. 391–400, 01 2016, doi: 10.1152/japplphysiol.00268.2016.

[70] N. Pettiaux, M. Cassart, M. Paiva, and M. Estenne, “Three-dimensional reconstruction of human diaphragm with the use of spiral computed tomography,” J. Appl. Physiol., vol. 82, no. 3, pp. 998–1002, Mar. 1997, doi: 10.1152/jappl.1997.82.3.998.

[71] J. Dansereau and I. A. F. Stokes, “Measurements of the three-dimensional shape of the rib cage,” J. Biomech., vol. 21, no. 11, pp. 893–901, Jan. 1988, doi: 10.1016/0021-9290(88)90127-3.

[72] M. G. Urbanchek, E. B. Picken, L. K. Kalliainen, and W. M. Kuzon, “Specific force deficit in skeletal muscles of old rats is partially explained by the existence of denervated muscle fibers,” J. Gerontol. A. Biol. Sci. Med. Sci., vol. 56, no. 5, pp. B191-197, May 2001, doi: 10.1093/gerona/56.5.b191.

[73] M. L. N. G. Malbrain, Y. Peeters, and R. Wise, “The neglected role of abdominal compliance in organ-organ interactions,” Crit. Care Lond. Engl., vol. 20, p. 67, Mar. 2016, doi: 10.1186/s13054-016-1220-x.

[74] J. Heidecker, J. T. Huggins, S. A. Sahn, and P. Doelken, “Pathophysiology of Pneumothorax Following Ultrasound-Guided Thoracentesis,” Chest, vol. 130, no. 4, pp. 1173–1184, Oct. 2006, doi: 10.1016/S0012-3692(15)51155-0.

[75] R.-S. Lan, “Elastance of the Pleural Space: A Predictor for the Outcome of Pleurodesis in Patients with Malignant Pleural Effusion,” Ann. Intern. Med., vol. 126, no. 10, p. 768, May 1997, doi: 10.7326/0003-4819-126-10-199705150-00003.

[76] M. Galal, A. El Halafawy, H. H. Assal, and Y. El-kabany, “Pleural manometry in pleural effusion,” Egypt. J. Chest Dis. Tuberc., vol. 65, no. 2, pp. 415–419, Apr. 2016, doi: 10.1016/j.ejcdt.2016.02.006.

[77] E. Abrams, M. Mohr, C. Engel, and M. Bottlang, “CROSS-SECTIONAL GEOMETRY OF HUMAN RIBS,” p. 2.

[78] T. A. Wilson, K. Rehder, S. Krayer, E. A. Hoffman, C. G. Whitney, and J. R. Rodarte, “Geometry and respiratory displacement of human ribs,” J. Appl. Physiol. Bethesda Md 1985, vol. 62, no. 5, pp. 1872–1877, May 1987, doi: 10.1152/jappl.1987.62.5.1872.

[79] M. Goldman, “Mechanical Interaction between Diaphragm and Rib Cage,” p. 4.

[80] A. J. Merrell and G. Kardon, “Development of the diaphragm -- a skeletal muscle essential for mammalian respiration,” FEBS J., vol. 280, no. 17, pp. 4026–4035, Sep. 2013, doi: 10.1111/febs.12274.

[81] J. Kocjan, M. Adamek, B. Gzik-Zroska, D. Czyżewski, and M. Rydel, “Network of breathing. Multifunctional role of the diaphragm: a review,” Adv. Respir. Med., vol. 85, no. 4, pp. 224–232, 2017, doi: 10.5603/ARM.2017.0037.

[82] A. T. Johnson, Biomechanics and Exercise Physiology: Quantitative Modeling. CRC Press, 2007.

[83] P. D. Willem van Meurs, Modeling and Simulation in Biomedical Engineering: Applications in Cardiorespiratory Physiology. McGraw-Hill Education, 2011.

[84] D. Papandrinopoulou, V. Tzouda, and G. Tsoukalas, “Lung Compliance and Chronic Obstructive Pulmonary Disease,” Pulm. Med., vol. 2012, 2012, doi: 10.1155/2012/542769.

[85] P. E. Wright and G. R. Bernard, “The role of airflow resistance in patients with the adult respiratory distress syndrome,” Am. Rev. Respir. Dis., vol. 139, no. 5, pp. 1169–1174, May 1989, doi: 10.1164/ajrccm/139.5.1169.

[86] G. B. Nair and E. Castillo, “Longitudinal Lung Compliance Imaging in Idiopathic Pulmonary Fibrosis,” Radiology, vol. 293, no. 2, pp. 272–272, Sep. 2019, doi: 10.1148/radiol.2019191115.

[87] G. Nucci and C. Cobelli, “Mathematical Models of Respiratory Mechanics,” 2001, doi: 10.1016/B978-012160245-1/50011-8.

[88] F. Vicario, A. Albanese, N. Karamolegkos, D. Wang, A. Seiver, and N. W. Chbat, “Noninvasive Estimation of Respiratory Mechanics in Spontaneously Breathing Ventilated Patients: A Constrained Optimization Approach,” IEEE Trans. Biomed. Eng., vol. 63, no. 4, pp. 775–787, Apr. 2016, doi: 10.1109/TBME.2015.2470641.

[89] R. Penrose, “On best approximate solutions of linear matrix equations,” Math. Proc. Camb. Philos. Soc., vol. 52, no. 1, pp. 17–19, Jan. 1956, doi: 10.1017/S0305004100030929.

[90] “Convex Optimization | Guide books.” https://dl.acm.org/doi/book/10.5555/993483 (accessed Dec. 03, 2020).

[91] M. Grover, R. A. Slutsky, C. B. Higgins, and R. Shabetai, “Extravascular lung water in patients with congestive heart failure. Difference between patients with acute and chronic myocardial disease.,” Radiology, vol. 147, no. 3, pp. 659–662, Jun. 1983, doi: 10.1148/radiology.147.3.6342031.

[92] R. M. Dongaonkar, Integration of microvascular, interstitial, and lymphatic function to determine the effect of their interaction on interstitial fluid volume. 2009.

[93] F. Heijmans, J. L. Bert, and K. L. Pinder, “Digital simulation of pulmonary microvascular exchange,” Comput. Biol. Med., vol. 16, no. 2, pp. 69–90, Jan. 1986, doi: 10.1016/0010-4825(86)90033-8.

[94] J. L. Bert and K. L. Pinder, “Pulmonary microvascular exchange: An analog computer simulation,” Microvasc. Res., vol. 27, no. 1, pp. 51–70, Jan. 1984, doi: 10.1016/0026-2862(84)90041-4.

[95] F. Heijmans, J. Bert, and K. Pinder, “Alveolar flooding: a computer simulation,” Comput. Methods Programs Biomed., vol. 23, no. 2, pp. 93–101, Oct. 1986, doi: 10.1016/0169-2607(86)90104-5.

[96] R. E. Drake, G. A. Laine, S. J. Allen, J. Katz, and J. C. Gabel, “A model of the lung interstitial-lymphatic system,” Microvasc. Res., vol. 34, no. 1, pp. 96–107, Jul. 1987, doi: 10.1016/0026-2862(87)90082-3.

[97] C. C. Michel, “Starling: the formulation of his hypothesis of microvascular fluid exchange and its significance after 100 years,” Exp. Physiol., vol. 82, no. 1, pp. 1–30, Jan. 1997.

[98] S. Weinbaum, “1997 Whitaker Distinguished Lecture: Models to solve mysteries in biomechanics at the cellular level; a new view of fiber matrix layers,” Ann. Biomed. Eng., vol. 26, no. 4, pp. 627–643, Aug. 1998.

[99] R. H. Adamson, J. F. Lenz, X. Zhang, G. N. Adamson, S. Weinbaum, and F. E. Curry, “Oncotic pressures opposing filtration across non-fenestrated rat microvessels: Oncotic pressures opposing filtration,” J. Physiol., vol. 557, no. 3, pp. 889–907, Jun. 2004, doi: 10.1113/jphysiol.2003.058255.

[100] J. R. Levick and C. C. Michel, “Microvascular fluid exchange and the revised Starling principle,” Cardiovasc. Res., vol. 87, no. 2, pp. 198–210, Jul. 2010, doi: 10.1093/cvr/cvq062.

[101] M. Hlastala and A. Berger, Physiology of Respiration, Second Edition. Oxford, New York: Oxford University Press, 2001.

[102] S. Weinbaum, J. M. Tarbell, and E. R. Damiano, “The Structure and Function of the Endothelial Glycocalyx Layer,” Annu. Rev. Biomed. Eng., vol. 9, no. 1, pp. 121–167, Jul. 2007, doi: 10.1146/annurev.bioeng.9.060906.151959.

[103] R. O. Dull et al., “Lung heparan sulfates modulate Kfc during increased vascular pressure: evidence for glycocalyx-mediated mechanotransduction,” Am. J. Physiol.-Lung Cell. Mol. Physiol., vol. 302, no. 9, pp. L816–L828, Dec. 2011, doi: 10.1152/ajplung.00080.2011.

[104] N. C. Staub, “Pulmonary edema,” Physiol. Rev., vol. 54, no. 3, pp. 678–811, Jul. 1974, doi: 10.1152/physrev.1974.54.3.678.

[105] S. Modi, A. W. B. Stanton, W. E. Svensson, A. M. Peters, P. S. Mortimer, and J. R. Levick, “Human lymphatic pumping measured in healthy and lymphoedematous arms by lymphatic

congestion lymphoscintigraphy," J. Physiol., vol. 583, no. 1, pp. 271–285, Aug. 2007, doi: 10.1113/jphysiol.2007.130401.

[106] J. M. Yoffey and F. C. Courtice, Lymphatics, lymph and the lymphomyeloid complex. Academic Press, 1970.

[107] P. D. Snashall, K. Nakahara, and N. C. Staub, "Estimation of perimicrovascular fluid pressure in isolated perfused dog lung lobes," J. Appl. Physiol., vol. 46, no. 5, pp. 1003–1010, May 1979, doi: 10.1152/jappl.1979.46.5.1003.

[108] J. R. Casley-Smith, "Lymph and lymphatics," Microcirculation, vol. 1, pp. 423–502, 1977.

[109] Miff Linnette D., "Extra-Alveolar Vessels and Edema Development in Excised Dog Lungs," Circ. Res., vol. 28, no. 5, pp. 524–532, May 1971, doi: 10.1161/01.RES.28.5.524.

[110] J. S. Prichard, Edema of the Lung. Charles C Thomas Pub Limited, 1982.

[111] S. F. Rimoldi, M. Yuzefpolskaya, Y. Allemann, and F. Messerli, "Flash pulmonary edema," Prog. Cardiovasc. Dis., vol. 52, no. 3, pp. 249–259, Dec. 2009, doi: 10.1016/j.pcad.2009.10.002.

[112] M. Ursino and E. Magosso, "Acute cardiovascular response to isocapnic hypoxia. I. A mathematical model," Am. J. Physiol. Heart Circ. Physiol., vol. 279, no. 1, pp. H149-165, Jul. 2000, doi: 10.1152/ajpheart.2000.279.1.H149.

[113] E. Magosso and M. Ursino, "A mathematical model of CO2 effect on cardiovascular regulation," Am. J. Physiol. Heart Circ. Physiol., vol. 281, no. 5, pp. H2036-2052, Nov. 2001, doi: 10.1152/ajpheart.2001.281.5.H2036.

[114] D. Castro and M. Keenaghan, "Arterial Blood Gas," in StatPearls, Treasure Island (FL): StatPearls Publishing, 2020.

[115] "Guyton and Hall Textbook of Medical Physiology - 13th Edition." https://www.elsevier.com/books/guyton-and-hall-textbook-of-medical-physiology/hall/978-1-4557-7005-2 (accessed Dec. 29, 2020).

[116] J. L. Spencer, E. Firouztale, and R. B. Mellins, "Computational expressions for blood oxygen and carbon dioxide concentrations," Ann. Biomed. Eng., vol. 7, no. 1, pp. 59–66, Jan. 1979, doi: 10.1007/BF02364439.

[117] J. B. West and A. M. Luks, "West's Respiratory Physiology: The Essentials, 11e," Jan. 2021, Accessed: Dec. 29, 2020. [Online]. Available: https://meded.lwwhealthlibrary.com/book.aspx?bookid=2994.

Appendix A

The dynamic equations of the six pulmonary subsystems are summarized in this section.

A1. Lung Mechanics module

$$C_l \frac{dP_l}{dt} = \frac{P_{ao} - P_l}{R_{ml}} - \frac{P_l - P_{tr}}{R_{lt}} \quad (A-1)$$

$$C_{tr} \frac{d(P_{tr} - P_{pl})}{dt} = \frac{P_l - P_{tr}}{R_{lt}} - \frac{P_{tr} - P_b}{R_{tb}} \quad (A-2)$$

$$C_b \frac{d(P_b - P_{pl})}{dt} = \frac{P_{tr} - P_b}{R_{tb}} - \frac{P_b - P_A}{R_{bA}} \quad (A-3)$$

$$C_A \frac{d(P_A - P_{pl})}{dt} = \frac{P_b - P_A}{R_{bA}} \quad (A-4)$$

$$\dot{V} = \frac{P_{ao} - P_l}{R_{ml}} \quad (A-5)$$

$$V_l = C_l P_l + V_{u,l} \quad (A-6)$$

$$V_{tr} = C_{tr}(P_{tr} - P_{pl}) + V_{u,tr} \quad (A-7)$$

$$V_b = C_b(P_b - P_{pl}) + V_{u,b} \quad (A-8)$$

$$V_A = C_A(P_A - P_{pl}) + V_{u,A} \quad (A-9)$$

$$V_D = V_l + V_{tr} + V_b \quad (A-10)$$

A2. Alveolus Elasticity Module

$$\sigma_C = c_1 \log\left[1 - \frac{\exp(\epsilon_f) - 1}{c_2}\right] + c_3 \epsilon_f \quad (A-11)$$

$$\sigma_e = E \epsilon_f \quad (A-12)$$

$$\sigma_{fib} = \sigma_e + \sigma_c \quad (A-13)$$

$$F_{fib} = \sigma_{fib} A_{fib} \quad (A-14)$$

$$\gamma = \begin{cases} \gamma_0 - E\Gamma & \Gamma < \Gamma_\infty \\ \Gamma_\infty \exp\left[\frac{E}{\Gamma_\infty}(\Gamma_\infty - \Gamma)\right] & \Gamma \geq \Gamma_\infty \end{cases} \quad (A-15)$$

$$\mathrm{F_{surf}} = \frac{2\gamma}{\mathrm{R_{alv}}}\mathrm{A_{alv}} \quad (\mathrm{A}-16)$$

$$C_{alv} = \frac{V_A}{\rho RT} + \frac{\Delta V_A}{\Delta P_A} \quad (\mathrm{A}-17)$$

A3. Respiratory Muscles and Rib Cage Mechanics

RMRM Differential Equations with Transducer Equations:

$$m_{ct}\dot{v}_{ct} = F_{dia} - A_{do}P_{abd} + A_{do}P_{pl} - b_{dia}v_{ct} \quad (A-18)$$

$$C_{abd}\dot{P}_{abd} = A_{do}v_{ct} - l_{rb}^{l}A_{lrc}^{zoa}\sin\left(\theta_{l,o} - \theta_l\right)\omega_{lrc} \quad (A-19)$$

$$C_{pl}\dot{P}_{pl} = Q_{l-tr} - A_{do}v_{ct} - A_{urc}l_{rb}^{u}\sin\left(\theta_{u,o} - \theta_u\right)\omega_{urc} - A_{lrc}^{pl}l_{rb}^{l}\sin\left(\theta_{l,o} - \theta_l\right)\omega_{lrc} \quad (A-20)$$

$$I_{lrc}\dot{\omega}_{lrc} = A_{lrc}^{pl}l_{rb}^{l}\sin\left(\theta_{l,o} - \theta_l\right)P_{pl} + A_{lrc}^{zoa}l_{rb}^{l}\sin\left(\theta_{l,o} - \theta_l\right)P_{abd} - \tau' + l_{rb}^{l}\cos\left(\theta_{l,o} - \theta_l\right)F_{dia} - b_{lrc}\omega_{lrc} - k_{lrc}\theta_{lrc} \quad (A-21)$$

$$I_{urc}\dot{\omega}_{urc} = l_{rb}^{u}\cos\left(\theta_{u,o} - \theta_u\right)F_{int} + A_{urc}l_{rb}^{u}\sin\left(\theta_{u,o} - \theta_u\right)P_{pl} + \tau' - b_{urc}\omega_{urc} - k_{urc}\theta_{urc} \quad (A-22)$$

$$\dot{\tau}' = k\left(\omega_{lrc} - \omega_{urc} - \frac{1}{b}\tau'\right) \quad (A-23)$$

RMRM Transducer Equations

$$\begin{bmatrix} v_{ct} \\ F_{ct}^{pl} \end{bmatrix} = \begin{bmatrix} 0 & \frac{1}{A_{do}} \\ -A_{do} & 0 \end{bmatrix}\begin{bmatrix} P_{pl} \\ Q_{pl}^{ct} \end{bmatrix} \quad (A-24)$$

$$\begin{bmatrix} v_{ct} \\ F_{ct}^{abd} \end{bmatrix} = \begin{bmatrix} 0 & -\frac{1}{A_{do}} \\ A_{do} & 0 \end{bmatrix}\begin{bmatrix} P_{abd} \\ Q_{ab\,d}^{ct} \end{bmatrix} \quad (A-25)$$

$$\begin{bmatrix} P_{abd} \\ Q_{abd}^{lrc} \end{bmatrix} = \begin{bmatrix} 0 & \dfrac{-1}{l_{rb}^{l} A_{lrc}^{zoa} \sin(\theta_{l,o} - \theta_l)} \\ l_{rb}^{l} A_{lrc}^{zoa} \sin(\theta_{l,o} - \theta_l) & 0 \end{bmatrix} \begin{bmatrix} \omega_{lrc} \\ \tau_{lrc}^{abd} \end{bmatrix} \quad (A-26)$$

$$\begin{bmatrix} P_{pl} \\ Q_{pl}^{urc} \end{bmatrix} = \begin{bmatrix} 0 & \dfrac{-1}{l_{rb}^{u} A_{urc} \sin(\theta_{u,o} - \theta_u)} \\ l_{rb}^{u} A_{urc} \sin(\theta_{u,o} - \theta_u) & 0 \end{bmatrix} \begin{bmatrix} \omega_{urc} \\ \tau_{urc}^{pl} \end{bmatrix} \quad (A-27)$$

$$\begin{bmatrix} P_{pl} \\ Q_{pl}^{lrc} \end{bmatrix} = \begin{bmatrix} 0 & \dfrac{-1}{l_{rb}^{l} A_{lrc}^{\mathrm{pl}} \sin(\theta_{l,o} - \theta_l)} \\ l_{rb}^{l} A_{lrc}^{\mathrm{pl}} \sin(\theta_{l,o} - \theta_l) & 0 \end{bmatrix} \begin{bmatrix} \omega_{lrc} \\ \tau_{lrc}^{pl} \end{bmatrix} \quad (A-28)$$

$$\begin{bmatrix} F_{dia} \\ v_{dia} \end{bmatrix} = \begin{bmatrix} \dfrac{-1}{l_{rb}^{l} \cos(\theta_{l,o} - \theta_l)} & 0 \\ 0 & l_{rb}^{l} \cos(\theta_{l,o} - \theta_l) \end{bmatrix} \begin{bmatrix} \tau_{dia} \\ \omega_{lrc} \end{bmatrix} \quad (A-29)$$

$$\begin{bmatrix} F_{int} \\ v_{int} \end{bmatrix} = \begin{bmatrix} \dfrac{1}{l_{rb}^{u} \cos(\theta_{u,o} - \theta_u)} & 0 \\ 0 & -l_{rb}^{u} \cos(\theta_{u,o} - \theta_u) \end{bmatrix} \begin{bmatrix} \tau_{int} \\ \omega_{urc} \end{bmatrix} \quad (A-30)$$

RMRM Differential Equations

$$m_{ct} \dot{v_{ct}} = F_{dia} - F_{ct}^{abd} - F_{ct}^{pl} \quad (A-31)$$

$$C_{pl} \dot{P}_{pl} = Q_{l-tr} - Q_{pl}^{ct} - Q_{Pl}^{lrc} - Q_{pl}^{urc} \quad (A-32)$$

$$C_{abd} \dot{P}_{abd} = -Q_{abd}^{ct} - Q_{abd}^{lrc} \quad (A-33)$$

$$I_{lrc} \dot{\omega}_{lrc} = -\tau_{lrc}^{pl} - \tau_{lrc}^{abd} - \tau' - \tau_{dia} \quad (A-34)$$

$$I_{urc} \dot{\omega}_{urc} = -\tau_{int} - \tau_{urc}^{pl} + \tau' \quad (A-35)$$

$$\dot{\tau}' = k \left(\omega_{lrc} - \omega_{urc} - \frac{1}{b} \tau' \right) \quad (A-36)$$

A4. Microvascular Exchange System

$$\frac{dP_{int}}{dt} = \frac{1}{C_{int}} \cdot (Q_{mv-int} - Q_{int-tv} - Q_{int-as}) \quad (A-37)$$

$$Q_{mv-int}^{h} = \frac{1}{R_{endo}^{h}} \cdot (P_{mv} - P_{int}) \quad (A-38)$$

$$Q^{o}_{mv-sg} = Q^{o}_{sg-int} = -\frac{1}{R^{h}_{endo}} \cdot \sigma_{glx} \cdot (\pi_{mv} - \pi_{sg}) \quad (A-39)$$

$$Q_{mv-int} = Q^{h}_{mv-int} + Q^{o}_{sg-int} = \frac{1}{R^{h}_{endo}} \cdot [(P_{mv} - P_{int}) - \sigma_{glx} \cdot (\pi_{mv} - \pi_{sg}) \quad (A-40)$$

$$Q_{int-as} = \frac{1}{R^{h}_{epi}} \cdot [(P_{int} - P_{as}) - \sigma_{epi} \cdot (\pi_{int} - \pi_{as}) \quad (A-41)$$

$$\frac{dP_{as}}{dt} = \frac{1}{C_{as}} \cdot (Q_{int-as}) \quad (A-42)$$

$$V_{int} = \int Q_{mv-int} - Q_{int-tv} - Q_{int-as}\ dt \quad (A-43)$$

$$V_{as} = \int Q_{int-as}\ dt \quad (A-44)$$

A5. Pulmonary Blood Circulation

$$C_{pa} \frac{d(P_{pa} - P_{pl})}{dt} = Q_{rv,o} - Q_{pa} \quad (A-45)$$

$$L_{pa} \frac{dQ_{pa}}{dt} = P_{pa} - P_{pp} - R_{pa} Q_{pa} \quad (A-46)$$

$$V_{pa} = C_{pa} \cdot (P_{pa} - P_{pl}) + V_{u,pa} \quad (A-47)$$

$$(C_{ps} + C_{pp}) \frac{d(P_{pp} - P_{pl})}{dt} = Q_{pa} - Q_{ps} - Q_{pp} \quad (A-48)$$

$$Q_{pp} = \frac{P_{pp} - P_{pv}}{R_{pp}} \quad (A-49)$$

$$Q_{ps} = \frac{P_{ps} - P_{pv}}{R_{ps}} \quad (A-50)$$

$$P_{ps} = P_{pp} \quad (A-51)$$

$$V_{pp} = C_{pp} \cdot (P_{pp} - P_{pl}) + V_{u,pp} \quad (A-52)$$

$$V_{ps} = C_{ps} \cdot (P_{ps} - P_{pl}) + V_{u,ps} \quad (A-53)$$

$$(C_{pv}) \frac{d(P_{pv} - P_{pl})}{dt} = Q_{pp} + Q_{ps} - Q_{pv} \quad (A-54)$$

$$Q_{pv} = \frac{P_{pv} - P_{la}}{R_{pv}} \qquad (A-55)$$

$$V_{pv} = C_{pv} \cdot \left(P_{pv} - P_{pl}\right) + V_{u,pv} \qquad (A-56)$$

A6. Lung Gas Exchange System

$$V_D dF_{D,gas} = u(\dot{V})\dot{V}\left(F_{gas} - F_{D,gas}\right) + u(-\dot{V})\dot{V}_A\left(F_{D,gas} - F_{A,gas}\right) \qquad (A-57)$$

$$V_A dF_{A,gas} = u(\dot{V})\dot{V}_A\left(F_{D,gas} - F_{A,gas}\right) - K\left(Q_{pa}(1-sh)\left(C_{pp,gas} - \tilde{C}_{v,gas}\right) + V_{pp}\frac{dC_{pp,gas}}{dt}\right) \qquad (A-58)$$

$$C_{pp,O_2} = C_{pp,O_2}\frac{\left(X_{pp,O_2}\right)^{\frac{1}{h1}}}{1 + \left(X_{pp,O_2}\right)^{\frac{1}{h1}}} \qquad (A-59)$$

$$X_{pp,O_2} = P_{A,O_2}\frac{1+\beta_1 P_{A,CO2}}{K_1(1+\alpha_1 P_{A,CO2})} \qquad (A-60)$$

$$C_{pp,CO_2} = C_{pp,CO_2}\frac{\left(X_{pp,CO_2}\right)^{\frac{1}{h2}}}{1 + \left(X_{pp,CO_2}\right)^{\frac{1}{h2}}} \qquad (A-61)$$

$$X_{pp,CO_2} = P_{A,CO_2}\frac{1+\beta_2 P_{A,O2}}{K_2(1+\alpha_2 P_{A,O2})} \qquad (A-62)$$

$$P_{A,gas} = F_{A,gas}(P_{atm} - P_{ws}) \qquad (A-63)$$

$$C_{a,gas} = \frac{Q_{pp}C_{pp,gas} + Q_{ps}\tilde{C}_{v,gas}}{Q_{pp} + Q_{ps}} \qquad (A-64)$$

$$S_{a,gas}\% = \frac{C_{a,O_2} - P_{a,O_2}\cdot\frac{0.003}{100}}{Hgb \cdot 1.34}\cdot 100 \qquad (A-65)$$